Synthesis and Self-assembly of Monodisperse Nanoparticles

for Magnetic and Catalytic Applications

By

Liheng Wu

B.Sc., University of Science and Technology of China, 2009

M.A., Brown University, 2012

A Dissertation Submitted in Partial Fulfillment of the

Requirements for the Degree of Doctor of Philosophy

in the Department of Chemistry at Brown University

Providence, Rhode Island

May 2016

This dissertation by Liheng Wu is accepted in its present form

by the Department of Chemistry as satisfying the

dissertation requirement for the degree of Doctor of Philosophy.

Date _____   _____

                                                        Shouheng Sun, Advisor

Recommended to the Graduate Council by

Date _____   _____

                                                        Matthew Zimmt, Reader

Date _____   _____

                                                        Eunsuk Kim, Reader

Approved by the Graduate Council

Date _____   _____

                                                        Peter Weber, Dean of the Graduate School

CURRICULUM VITAE

Liheng Wu was born on November 7th, 1989 in Hefei, Anhui Province of China. He attended the University of Science and Technology of China from 2005 to 2009, graduating with his B. Sc. in Materials Science and Engineering. After that, he spent one year as a research assistant at Hefei National Laboratory for Physical Sciences at the Microscale, working with Prof. Shu-Hong Yu on microwave-assisted synthesis of functional nanostructures. In 2010, he was accepted in the graduate program of Chemistry Department at Brown University. He joined Prof. Shouheng Sun's group and started his doctoral research in 2011. In 2012, he received his M. A. in Chemistry and continued his Ph. D. research on the synthesis and self-assembly of monodisperse nanoparticles for magnetic recording and catalytic applications. He has 14 papers published in peer-reviewed journals, 1 approved patent and 2 papers in preparation.

PUBLICATIONS

16) **Wu, Liheng**; Mendoza-Garcia, Adriana; Sun, Shouheng. "Synthesis, Properties and Applications of Magnetic Nanoparticles", *Chemical Reviews*, **2016**, invited

15) **Wu, Liheng**; Li, Qing; Wu, Cheng-Hao.; Zhu, Huiyuan; Mendoza-Garcia, Adriana; Shen, Bo; Guo, Jinghua; Sun, Shouheng. "Stable Cobalt Nanoparticles and Their Monolayer Array as an Efficient Electrocatalyst for Oxygen Evolution Reaction", *Journal of the American Chemical Society*, **2015**, 137, 7071−7074

14) **Wu, Liheng**; Shen, Bo; Sun, Shouheng. "Synthesis and Assembly of Barium-doped Iron Oxide Nanoparticles and Nanomagnets", **2015**, submitted

13) Li, Qing;[†] **Wu, Liheng**;[†] Wu, Gang; Su, Dong; Lv, Haifeng; Zhang, Sen; Zhu, Wenlei; Casirmir, Anix; Zhu, Huiyuan; Mendoza-Garcia, Adriana; Sun, Shouheng. "New Approach to Fully-Ordered fct-FePt Nanoparticles for Much Enhanced Electrocatalysis in Acid", *Nano Letters*, **2015**, 15, 2468−2473 ([†]Equal contribution)

12) Du, Xuewen; Zhou, Jie; **Wu, Liheng**; Sun, Shouheng; Xu, Bing. "Enzymatic Transformation of Phosphate Decorated Magnetic Nanoparticles for Selectively Sorting and Inhibiting Cancer Cells", *Bioconjugate Chemistry*, **2014**, 25, 2129–2133.

11) **Wu, Liheng**; Jubert, Pierre-Olivier; Berman, David; Imaino, Wayne; Nelson, Alshakim; Zhu, Huiyuan; Zhang, Sen; Sun, Shouheng. "Monolayer Assembly of Ferrimagnetic $Co_xFe_{3-x}O_4$ Nanocubes for Magnetic Recording", *Nano Letters*, **2014**, 14, 3395–3399.

10) Zhang, Sen; Jiang, Guangming; Filsinger, Gabriel T.; **Wu, Liheng**; Zhu, Huiyuan;

Lee, Jonghun; Wu, Zhongbiao; Sun, Shouheng. "Halide Ion-mediated Growth of Single Crystalline Fe Nanoparticles", *Nanoscale*, **2014**, 6, 4852–4856.

9) Klara, Kristina; Hou, Ning; Lawman, Allison; **Wu, Liheng**; Morrill, Drew; Tente, Alfred; Wang, Li-Qiong. "Developing and Implementing a Simple, Affordable Hydrogen Fuel Cell Laboratory in Introductory Chemistry", *Journal of Chemical Education*, **2014**, 91, 1924–1928.

8) Zhu, Huiyuan; Zhang, Sen; Huang, Yuixi; **Wu, Liheng**; Sun, Shouheng. "Monodisperse $M_xFe_{3-x}O_4$ (M = Fe, Cu, Co, Mn) Nanoparticles and Their Electrocatalysis for Oxygen Reduction Reaction", *Nano Letters*, **2013**, 13, 2947–2951.

7) Guo, Shaojun; Zhang, Sen; **Wu, Liheng**; Sun, Shouheng. "Co/CoO Nanoparticles Assembled on Graphene for Electro-chemical Reduction of Oxygen", *Angewandte Chemie International Edition*, **2012**, 51, 11770–11773.

6) **Wu, Liheng**; Yao, Hong-Bin; Hu, Bo; Yu, Shu-Hong. "Unique Lamellar Sodium/Potassium Iron Oxide Nanosheets: Facile Microwave-Assisted Synthesis and Magnetic and Electrochemical Properties", *Chemistry of Materials*, **2011**, 23, 3946–3952.

5) Yao, Hong-Bin; **Wu, Liheng**; Cui, Chunhua; Fang, Haiyu; Yu, Shu-Hong. "Direct Fabrication of Photoconductive Patterns on LBL Assembled Graphene Oxide/PDDA/Titania Hybrid Films by Photothermal and Photocatalytic Reduction", *Journal of Materials Chemistry*, **2010**, 20, 5190–5195.

4) Yao, Hong-Bin; Fang, Hai-Yu; Tan, Zhi-Hua; **Wu, Liheng**; Yu, Shu-Hong. "Biologically Inspired, Strong, Transparent, and Functional Layered Organic-

Inorganic Hybrid Films", *Angewandte Chemie International Edition*, **2010**, 49, 2140–2145.

3) Hu, Bo; **Wu, Liheng**; Zhao, Zhi; Zhang, Meng; Chen, Shao-Feng.; Liu, Shu-Juan; Shi, Hong-Yan; Ding, Ze-Jun; Yu, Shu-Hong. "Hierarchical Silver Indium Tungsten Oxide Mesocrystals with Morphology-, Pressure-, and Temperature-dependent Luminescence Properties", *Nano Research*, **2010**, 3, 395–403.

2) Hu, Bo;[†] **Wu, Liheng**;[†] Liu, Shu-Juan; Yao, Hong-Bin; Shi, Hong-Yan; Li, Gong-Pu; Yu, Shu-Hong. "Microwave-assisted Synthesis of Silver Indium Tungsten Oxide Mesocrystals and Their Selective Photocatalytic Properties", *Chemical Communications*, **2010**, 46, 2277–2279. ([†]Equal contribution)

1) Hu, Bo; Wang, Kan; **Wu, Liheng**; Yu, Shu-Hong; Antonietti, Markus.; Titirici, Maria-Magdalena. "Engineering Carbon Materials from the Hydrothermal Carbonization Process of Biomass", *Advanced Materials*, **2010**, 22, 813–828.

ACKNOWLEDGEMENTS

Looking back upon my graduate life, I would like to thank many wonderful people whose great support in the past five years has made my Ph.D. study meaningful and successful. First of all, my sincerest thanks go to my advisor, Prof. Shouheng Sun. Thank him for giving me much freedom during my graduate research, although it was not going smoothly during the first two years. His passion towards science, his inspiring ideas, and his mentoring on critical thinking and logical presentations have motivated me a lot. I cannot imagine what it would be without his great support and encouragement. I am so grateful for what I have learnt from him, which I believe will be a great treasure for my future career.

I would like to thank many great professors at Brown. Prof. Wesley Bernskoetter and Prof. Eunsuk Kim served as my committee member and gave lots of valuable advice during my graduate study, especially on my RPD and ORP defense. I still remember what Prof. Wesley Bernskoetter criticized during my first ORP, which made me better as a researcher for presenting a proposal defense. I greatly appreciate Prof. Eunsuk Kim for her advice and constant encouragement during my graduate study. I also would like to thank them for their excellent lecturing during my first semester at Brown. There are some other professors who lectured me. I thank Prof. Paul Williard for his interesting lecturing on Crystallography and Prof. Dwight Sweigart for his enlightening teaching on Electrochemistry. I would like to specially thank Prof. Matthew Zimmt for joining my thesis defense as a committee member after Prof. Bernskoetter left Brown University.

It is very wonderful to have worked with many brilliant and hardworking lab members. I would like to thank Dr. Sen Zhang for teaching me nanoparticle synthesis at the early stage when I joined the group. And "thank" him for burning down my old hood so that I could get a new one, even though waiting for about 1 year was too long for the replacement. I would like to thank Dr. Qing Li for helping with the electrochemical studies. Thank Dr. Shaojun Guo for helpful discussion on electrocatalysis. Thank Dr. Yongsheng Yu for the discussion on magnetic properties of nanoparticles. I thank Dr. Aruna Sigdel for the help on dialysis and ligand exchange of nanoparticles. Thank Dr. Sally Ho for bringing so much fun to our lab. I would like to thank Dr. Huiyuan Zhu, Bo Ning, Adriana Mendoza-Garcia and Wenlei Zhu. We had really good time as a team in the lab. Thank Dr. Yi Liu, Dr. Vismadeb Mazumder, Dr. Xiaolian Sun, Dr. Jonghun Lee, Dr. Dongguo Li, Dr. Guangming Jiang, Dr. Haifeng Lv, Hongyi Zhang, Gabriel Filsinger, Zheng Xi, Bo Shen, Caoyuan Ma, Yuyang Li, Junrui Li and Sibo Wang for helpful discussions. I wish you all the best in your future endeavor.

I would not finish my thesis without the help from many collaborators and professional personnel. I sincerely appreciate Dr. Pierre-Olivier Jubert, Dr. David Berman, Dr. Wayne Imaino and Dr. Alshakim Nelson from IBM Almaden Research Center for their help on the magnetic recording demonstration. It was a great experience to participate in the INSIC project. Thank Dr. Dong Su from Brookhaven National Laboratory for his great work on the characterization of my intermetallic nanoparticles. Thank Dr. Qiang Hao and Wenzhe Chen from the Department of Physics at Brown University for their assistance on magnetic measurements. Thank Cheng Hao Wu and Dr. Jinghua Guo from Lawrence Berkeley National Laboratory for the surface analysis of my

Dedicated to My Family

Abstract of "*Synthesis and Self-assembly of Monodisperse Nanoparticles for Magnetic and Catalytic Applications*" by Liheng Wu, Ph. D., Brown University, May 2016.

With unique properties different from their bulk materials, magnetic nanoparticles (NPs) have been extensively studied not only for scientific interests but also for technological developments. Organic solution-phase synthesis provides a versatile and robust method for synthesizing monodisperse NPs with controlled size, shape and composition. Those monodisperse NPs can be self-assembled into functional devices through the "bottom-up" approach. This thesis focuses on the synthesis and self-assembly of several magnetic NPs, as well as their applications in magnetic recording and catalysis.

Synthesis and self-assembly of monodisperse magnetic NPs are very important for magnetic recording. In this thesis, I will discuss the controlled synthesis of cobalt ferrite NPs with tunable size and magnetic properties. Large-area monolayer arrays of those ferrimagnetic NPs were fabricated through the water-air interfacial self-assembly. The monolayer arrays were studied as the magnetic recording media, demonstrating their great potentials in data storage application. This solution-phase synthesis and self-assembly approach were extended to ferromagnetic barium ferrite NPs, which can be potentially used for magnetic recording and permanent magnets.

The investigations of magnetic NPs for catalytic applications will also be discussed. Specifically, I will discuss the efficient catalytic activity of cobalt (Co) NPs for oxygen evolution reaction (OER) in water splitting. Highly stable Co NPs were synthesized through thermal decomposition of $Co_2(CO)_8$ followed by a post reductive annealing treatment. The developed NPs are more active and stable than state-of-the-art iridium

catalyst. Moreover, well-defined monolayer catalyst of the Co NPs was developed to evaluate their intrinsic OER activity, showing 15 times higher turnover frequency and mass activity than the NPs deposited on conventional carbon support.

Strong ferromagnetic face-centered tetragonal (fct) FePt NPs are a superior catalyst towards oxygen reduction reaction (ORR). However, it is very challenging to make fully order intermetallic fct-FePt NPs. In the thesis, I will discuss a new approach to fully ordered fct-FePt NPs through dumbbell-like FePt-Fe_3O_4 NPs. The fct-FePt NPs exhibit the highest catalytic activity and durability for ORR among all intermetallic Pt-based catalysts.

Table of Contents

List of Figures

List of Tables

Chapter 1. Introduction to Nanomaterials, Nanomagnetism and Nanoparticle Catalysts

1.1. General Introduction to Nanomaterials

In 1959 physicist Richard Feynman gave a talk entitled "There's Plenty of Room at the Bottom" at the California Institute of Technology, describing a process of manipulating and controlling individual atoms and molecules.[1] This is where the concept of nanotechnology began. However, modern nanotechnology started from 1981 when Gerd Binnig and Heinrich Rohrer at IBM-Zürich invented the scanning tunneling microscopy, making the manipulation of individual atoms achievable. Since then, nanotechnology has attracted more and more attention not only for fundamental scientific research but also for technological applications.[2-8] One nanometer (nm) is one billionth (10^{-9}) of a meter, which is a really small length scale. For example, a single gold atom is about one third of nanometer in diameter; a strand of human DNA is about 0.5~2 nm in diameter. The illustration in **Figure 1-1** shows how small the nanoworld is compared to some natural things. Typically nanoparticles (NPs) are on the length scale of 1 − 100 nm.
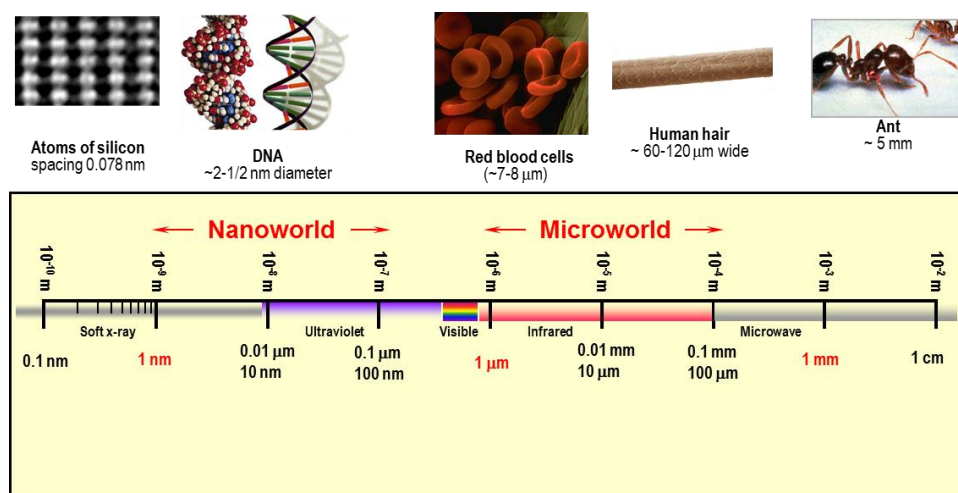
Figure 1-1. The scale chart to illustrate how small the nanoworld is (Courtesy of the Office of Basic Energy Sciences for the U.S. Department of Energy).

When the size of a material decreases to the nanoscale, its physical and chemical properties differentiate significantly from its bulk counterpart. This is called size-dependent effects. One direct consequence of the size-dependent effects is the surface area change. Much larger surface areas can be obtained for NPs. A simple demonstration can show why nanomaterials have extraordinary high surface areas. Imagining a solid cubic material with the length of 1 cm, the surface area is 6 cm^2. However, by splitting this cube into 1 mm small cube, one can get 1000 small cubes with the total surface area of 60 cm^2; further splitting the 1 cm cube into 1 nm nanocube, the total surface area increases dramatically to 60,000,000 cm^2. This size effect also leads to an increase of the surface atoms by decreasing the size of a NP. For example, in cluster NPs shown in **Figure 1-2**,[9] if the total number of atoms decreases from 561 to 13, the surface atoms percentage can increase significantly from 45% to 92%.

Full-Shell "Magic Number" Clusters					
Number of shells	1	2	3	4	5
Number of atoms in cluster	M_{13}	M_{55}	M_{147}	M_{309}	M_{561}
Percentage surface atoms	92%	76%	63%	52%	45%

Figure 1-2. The relationship between the number of atoms in cluster nanoparticles and the percentage of surface atoms.[9]

There are significant differences between the surface atoms and the inner ones. In a NP, the inner atoms are highly coordinated forming bonds similarly to the atoms in the bulk material. However, the surface atoms are less saturated, especially those corner and edge atoms on the surface. They are much less stable than the inner atoms. This lower

stabilization of the surface atoms causes lower melting points of NPs compared to the bulk ones. Taking the well-studied Au nanoparticles into consideration, the melting point of ~2 nm Au nanoparticles was reported to be about 800 K, much lower to its bulk value of 1336 K.[10] Another important consequence of the unstable surface atoms is their high chemical activity. The unsaturated surface atoms are extremely active to react with other molecules or intermediates to form new bonds, which are of great importance for developing efficient catalysts for specific reactions.

The other important size-dependent effect is quantum effect, which is well known in semiconductor materials. For instance, quantum dots (e.g. CdSe) are typical semiconducting nanocrystals. The most phenomenal properties of quantum dots are their size-dependent optical properties. In bulk semicondutors, when excited, electrons in the valence band jump to the conduction band, leaving holes in the valence band. The electrons-holes pairs are called excitons. The normal size of an exciton (also called exciton Bohr radius) is in nanometer region. As the size of a semiconductor material reaches a certain limit in nanoscale, the geometric confinement of excitons results in quantum confinement, making the energy spectrum discrete and the band gap size-dependent, as illustrated **Figure 1-3A**.[11] The smaller the nanocrystals, the bigger the band gap. Thus, more energy is needed to excite the electrons in the valence band of the dots and consequently, and more energy will be released when the excited electrons and holes recombine. This effect results in a blue-shift in emission as the size of quantum dots decreases. **Figure 1-3B** is a photo demonstrating size-tunable fluorescence properties of CdSe quantum dots with different sizes.[12] **Figure 1-3C** shows the absorption and emission spectra of the corresponding quantum dots, further confirming the quantum size

effects on the optical properties of quantum dots.[12] As a result of the quantum effect, the fluorescence of the quantum dots can be easily tuned by simply adjusting their sizes. With wide optical tunability and long term stability, quantum dots have attracted lots of attention as fluorophores in biological labelling.[12-14] Moreover, their unique band-gap engineering offers great potential in photovoltaics, solid-state lighting and displays.[15-18] Quantum dot displays, as a revolutionary display technology, is coming to our daily life with much brighter color and more power efficiency.
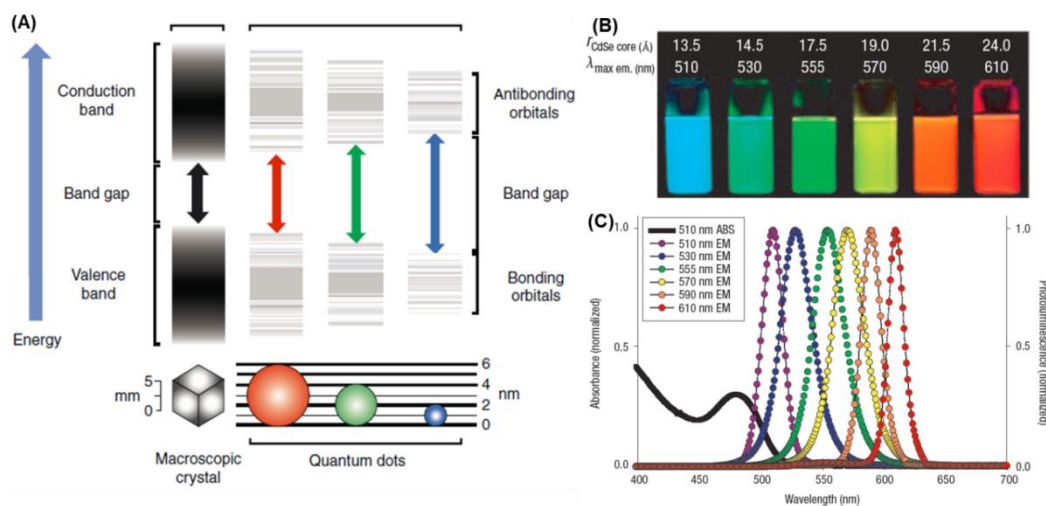
Figure 1-3. (A) Size-dependent electronic energy states of a semiconductor in the transition from bulk crystals to nanocrystals.[11] (B) A photograph demonstrating size-tunable fluorescence properties of CdSe quantum dots with different sizes. (C) The absorption and emission spectra of the corresponding quantum dots.[12]

Properties of NPs are not only size-dependent, but also shape-dependent. Taking quantum dots into consideration again, their bandgap is strongly dependent on the dimensionality.[19] Due to the shape effect on quantum confinement, much effort has been made to synthesize NPs with precisely controlled shape and dimension.[20] The shape effect is also obvious in metal nanostructures (e.g. Au) for their surface plasmon

resonance (SPR), which results from the oscillation between the surface conduction electrons and the electromagnetic radiation. By tuning the shape of the metallic NPs, the SPR can be easily tuned.[21-23] **Figure 1-4A** shows a typical TEM image of Au nanorods with the aspect ratio of 5.9.[21] Their longitudinal SPR peak locates at 979 nm. Enhancing the aspect ratio to 8.5 makes the LSPR shift significantly to NIR region at 1246 nm (**Figure 1-4B**). The broadly tunable SPR in metallic nanostructures is of great potential in sensing,[24] bioimaging and therapeutic applications.[25-27]
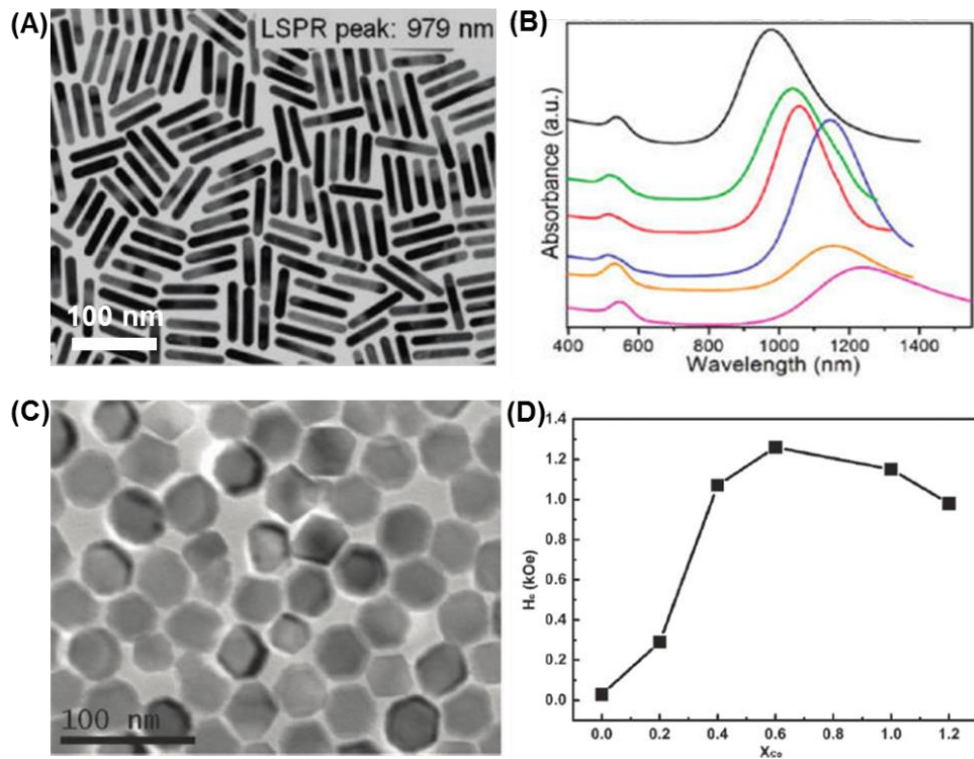
Figure 1-4. (A) TEM image of Au nanorods with the aspect ratio of 5.9. (B) UV-vis-NIR spectra of Au nanorods with increased aspect ratio from 5.9 to 8.5.[21] (C) TEM image of 35 nm $Co_xFe_{3-x}O_4$ nanoparticles. (D) Composition dependence of the coercivity (H_c) of 35 nm $Co_xFe_{3-x}O_4$ nanoparticles.[28]

The composition of NPs also strongly affects their chemical and physical properties. As a result, many research efforts have been made to synthesize NPs with precise

composition control. An example of ferrimagnetic cobalt ferrite system ($Co_xFe_{3-x}O_4$) is presented here. The magnetic coercivity (H_c) of cobalt ferrite is strongly dependent on the composition of Co.[29] Due to the competing effect of spin-orbit coupling and crystal field energy, the H_c increases as Co composition x increases and reaches the highest at around x = ~0.6-0.7, which is confirmed in the 35 nm $Co_xFe_{3-x}O_4$ nanoparticles (**Figure 1-4C and D**).[28] Thus it is important to control the chemical composition of NPs for tunable and optimum properties.

1.2. Introduction to Nanomagnetism

1.2.1. Classes of Magnetism

Magnets have been widely used since a long time ago, especially in ancient China. By the 12th century the Chinese were well known for using the loadstone compass for navigation. However, the basics of magnetism have started to be understood since Hans Christian Ørsted, a professor at the University of Copenhagen, discovered the relationship between electricity and magnetism in 1819. Electromagnetism has been continuing to develop ever since. This famous Ørsted's experiment is illustrated in **Figure 1-5A,** which shows how a magnetic field H can be generated by a current loop. In atomic physics, the magnetism is mainly from the electron magnetic moment, which is caused by the orbital and spin magnetization of an electron (**Figure 1-5B**). Based on the interaction of atomic magnetic moments, materials can be divided into five major groups: diamagnetism, paramagnetism, ferromagnetism, ferrimagnetism, and antiferromagnetism.
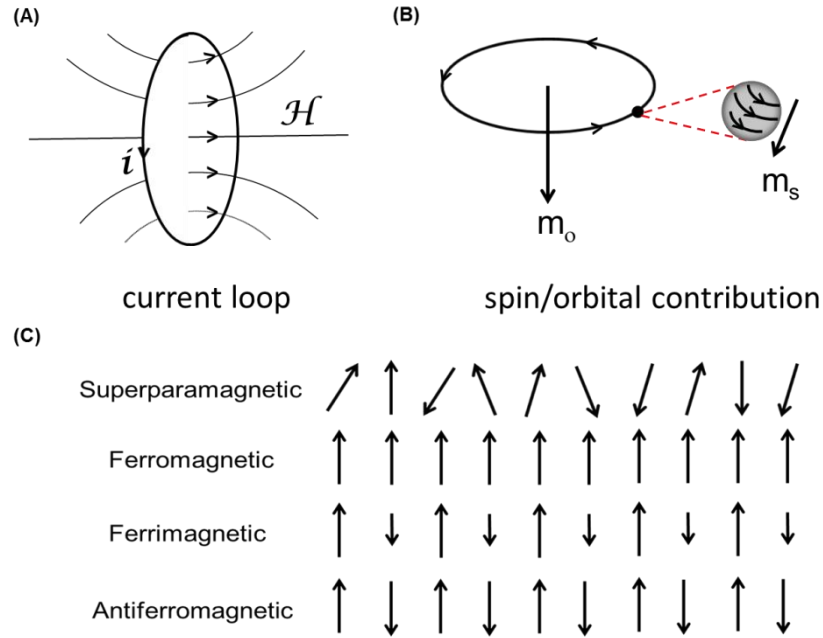
Figure 1-5. (A) Magnetic field generated by a current loop. (B) Magnetics from an electron by spin and orbital contribution. (C) Illustration of atomic moment interactions in different classes of magnetic materials

Diamagnetism is a fundamental property of all materials, which are composed of atoms with no net magnetic moments (no unpaired electrons). Due to the very weak property, diamagnetic effect is overwhelmed in the strong magnetic materials like paramagnetic and ferromagnetic materials. In paramagnetic materials, there are some unpaired electrons in partially filled orbitals. In the absence of external field, the spins are randomly oriented due to thermal fluctuation and the net magnetization is zero (**Figure 1-5C**). But in the presence of an external applied magnetic field, those atomic magnetic moments will align in the directions of the field, resulting in a net positive magnetization. Removing the external field causes a spontaneous randomization of those atomic magnetic moments and zeros the net magnetization again. Different from paramagnetism, in ferromagnetic materials, the atomic moments are strongly interacted by electronic

exchange forces. The strong interaction causes a parallel alignment of the atomic moments, which shows a large net magnetization even in the absence of external field.

In ferrimagnetic materials, there are two magnetic sublattices interacted by superexchange coupling. This interaction results in antiparallel alignment of the two sublattices. However, their magnetic moments are not equal with a existing net magnetic moment. Ferrimagnetism shows similar magnetic behavior to ferromagnetism. Antiferromagnetism also exhibits strong superexchange interaction, but differently, the two sublattices have the same magnetic moments and cancel each other in the antiparallel alignment, resulting in zero net magnetization.

1.2.2. Properties of Ferromagnetic Nanoparticles

Due to strong interactions of atomic moments, ferromagnetic/ferrimagnetic materials show characteristic magnetic behavior: once magnetized, they can retain a memory of the applied field. This behavior is called hysteresis and the curve of the magnetization change with the external field is called a hysteresis loop. A typical hysteresis loop of ferromagnetic materials is shown in **Figure 1-6A**. In the presence of external field, the domains (the region where individual magnetic moments of atoms align in the same direction) in a ferromagnetic material tend to align in the direction of the field. When the field is strong enough, all the domains are aligned in the field direction. In this case, the material is saturated and the corresponding magnetic moment is called saturation moment (M_s). After magnetization, if one removes the external field, due to the strong magnetic interaction between the domains, the material still exhibits a significant amount of moment, which is call remnant moment (M_r). The remnant moment is the basis for

magnetic recording. In order to totally demagnetize it, a reverse magnetic field has to be applied. The field that needs to drive the magnetization to zero again is called coercivity (H_c). This hysteresis behavior is very different from the magnetization curve of superparamagnetic materials. In a superparamagnetic material, owning to the thermal fluctuation, the magnetic domains undergo randomization as long as the external field is removed, leaving no remnant magnetic moment (**Figure 1-6B**).
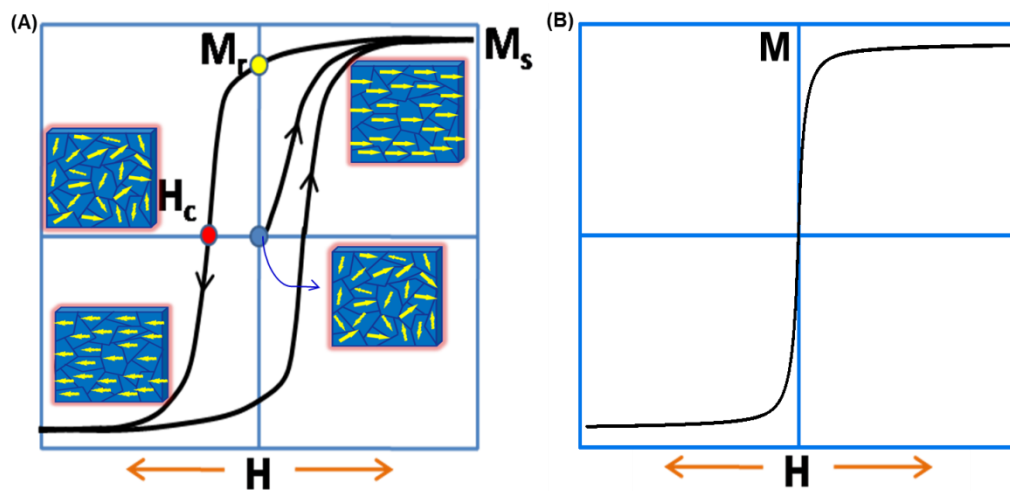
Figure 1-6. Schematic illustration of (A) the hysteresis loops of ferromagnetic/ferrimagnetic and (B) the magnetization curve of superparamagnetic materials.

The magnetic properties of a ferromagnetic material are strongly size-dependent. The size below which all the magnetic spins in a ferromagnetic grain align in the same direction is called the critical size (D_c). Below the D_c, the grain becomes a single domain (SD). For most ferromagnetic materials, the critical size is in the range of $5 - 100$ nm. If the grain size is bigger than D_c, multi-domains (MD) exist inside. Due to the domain-domain interaction, the magnetic coercivity decreases with increasing the size. A relatively low field is needed to change the magnetization of a MD grain through an energetically easy domain wall translation process. However, in the SD size range, the

only way to change the magnetization is through the rotation of the magnetization, which is an energetically difficult process. Thus the coercivity for SD NPs is relatively high. In the SD size range, as the size continues to decrease, another critical threshold is reached, at which the ferromagnetic becomes superparamagnetic. This critical limit is call superparamagnetic limit. The size-dependent coercivity of ferromagnetic NPs is shown in **Figure 1-7A**.[30-31] The reason for the transition of ferromagnetism to superparamagnetism in the SD size range is explained in **Figure 1-7B**, which shows the energy barrier between the "up" and "down" magnetization of a SD NP. The energy required for reversing the magnetization of a SD NP is KV, where K is magneto-anisotropic constant and V is the volume of the nanoparticle. If V is small enough, thermal energy $k_B T$ (k_B is Boltzmann constant, T is temperature) will be sufficient to overcome the energy barrier, causing a spontaneous reversal of magnetization. The superparamagnetic limit of small ferromagnetic NPs has proven to be a challenge in the design of recording media for magnetic data storage applications. However, the properties of those superparamagnetic NPs, namely their high M_s in the small external field and no M_r, render them great potentials in biomedical applications, especially in drug delivery, magnetic resonance imaging, and hyperthermia therapy.[32-43]

11
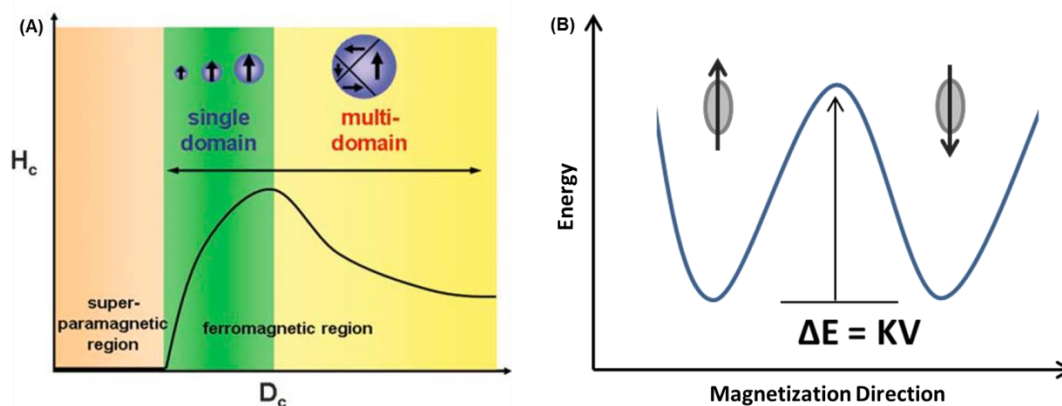
Figure 1-7. (A) A plot of magnetic coercivity (H_c) vs. the size of ferromagnetic nanoparticles.[30] (B) Sketch of double well potential showing the energy plotted against the orientation of the magnetization of magnetic nanoparticles in the absence of field.

The magnetic properties of ferromagnetic NPs are not only size-dependent, but also temperature-dependent. For ferromagnetic NPs with a certain size, at a particular temperature, thermal energy $k_B T$ will be high enough and eventually overcome the reversal barrier, causing a randomization effect. This temperature is called Curie temperature (T_c). Above T_c, ferromagnetism transits into superparamagnetism. Curie temperature is also an intrinsic property which is important in determining the application of ferromagnetic NPs.

1.2.3. Applications of Ferromagnetic Nanoparticles

One important application of ferromagnetic NPs is as building blocks of permanent magnets for magnetic energy storage applications. Permanent magnets with high energy storage have various applications in our daily life, such as in the fabrication of direct-current motors and wind turbines. As an intrinsic property, ferromagnetic materials maintain remnant magnetic moment (M_r) after magnetization. Due to this property, permanent magnets could be used to generate a large magnetic field. However, for long-time stability, they must possess a large coercivity (H_c). A figure-of-merit for evaluating the performance of a permanent magnet is referred to as the maximum energy product $(BH)_{max}$, which corresponds to the area of the largest rectangle that can fit inside the second quadrant of the B-H hysteresis loop by converting M into magnetic induction $B = H + 4\pi M$. The increase of the magnetic energy in a specific volume of a permanent magnet would result in the enhancement of the energy conversion efficiency and also the

decrease of the device size. However, regular hard ferromagnetic materials, such as SmCo$_5$[44] and fct-FePt[45-47], have very high H$_c$ (> 10000 Oe) but relatively low M$_s$, while soft magnetic materials (e.g. bcc-Fe[48] and FeCo[49]) have very high M$_s$ but very small H$_c$ (< 1000 Oe). In order to enhance the energy storage of a permanent magnet, both high coercivity and saturation moment would be needed. Exchange coupling provides an alternative way for this purpose. The illustration of a modulated hard-soft exchange-coupled system is shown in **Figure 1-8**. The requirements for effective exchange coupling between the two phases are very strict.[50-51] First of all, the hard magnet and soft magnet much be in close contact with each other. Secondly and the most importantly, the size of the soft phase must be appropriate. If the size of the soft phase is too large, the composite would be non-exchange-coupled (**Figure 1-8A**). Just the interface between the hard and soft magnets is effective coupled, the majority of the soft would be easily magnetized and demagnetized, and therefore there would be a kink in the demagnetization curve showing two phase behavior. Only with appropriate size of the soft phase (~10 nm) will the composite be effectively exchange couples with enhanced energy storage (**Figure 1-8B**).

A successful exchange-coupled nanocomposite has been achieved in self-assembled FePt and Fe$_3$O$_4$ NPs.[52] Annealing the composite under reducing atmosphere resulted in the fct-FePt/Fe$_3$Pt composite with enhanced energy product of 20.1MGOe, which is 50 % more than theoretical limit of 13 MGOe for non-exchange-coupled isotropic FePt. Another example is recently developed exchange-coupled fct-FePt/Co core/shell nanoparticles, within which the magnetic properties can be rationally tuned by the shell thickness of the soft phase.[53]
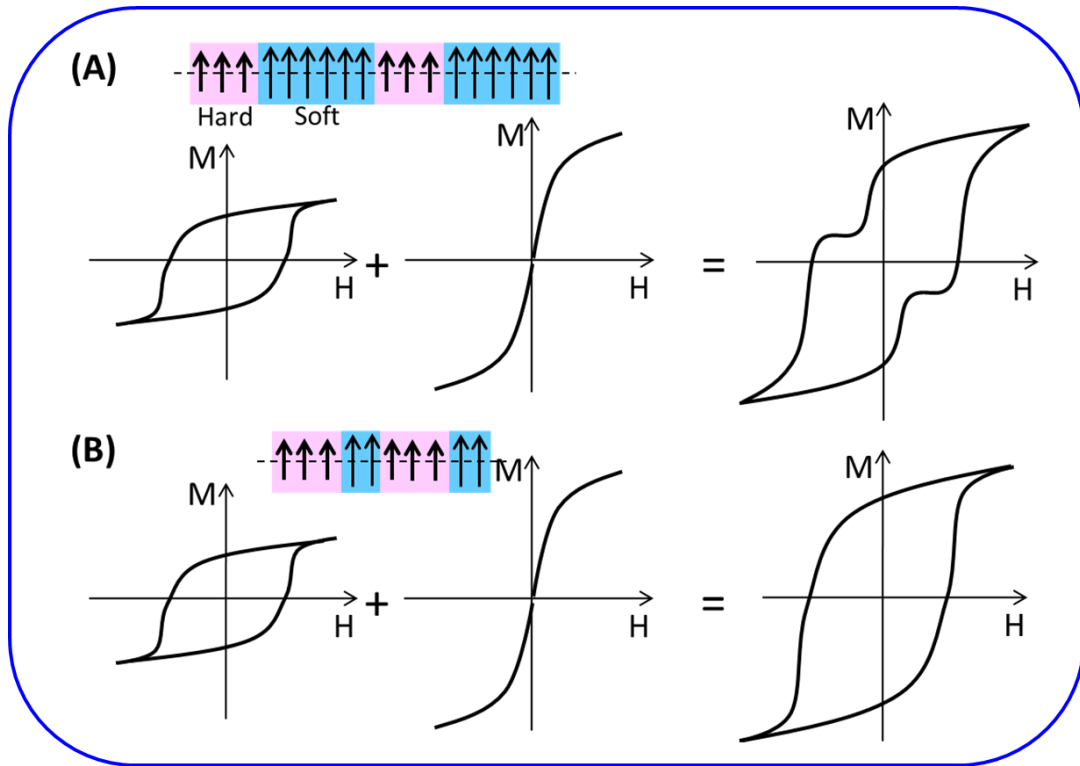
Figure 1-8. Illustration of (A) non-exchange-coupled system and (B) exchange-coupled system in magnetic soft and hard composites.

Another very important application of ferromagnetic NPs is as recording media in magnetic data storage. Magnetic recording also takes advantage of the remnant magnetization (M_r) of ferromagnetic NPs, which converts magnetic signals of those ferromagnetic NPs into voltage signals by giant magnetoresistance (GMR) sensors. **Figure 1-9A** shows a typical longitudinal recording system in hard disk drive (HDD).[54] Basically, it composes of three parts: magnetic recording medium of ferromagnetic NPs, write head and read head. During writing process, the write head is driven by a flux current carrying the information to be stored, generating a flux external field. The flux field changes the magnetization of the recording medium under the write head. To read back the stored information on the recording medium, the read head is used. The read head, namely GMR sensors, translates the recorded magnetic signal into a voltage signal

14
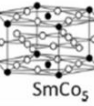
(**Figure 1-9B**). Due to the significant advancements in materials science and recording technology, there is a dramatic enhancement of the recording areal density, as shown in **Figure 1-9C**.[55] **Figure 1-9D** shows a typical TEM image of the media material of CoCrPtX NPs with the size of ~8.5 nm in the commercial HDD.[56] This recording media guarantee a recording density of ~750 Gb/in^2. To further increase the areal density, the size of the media NPs needs to be further reduced.
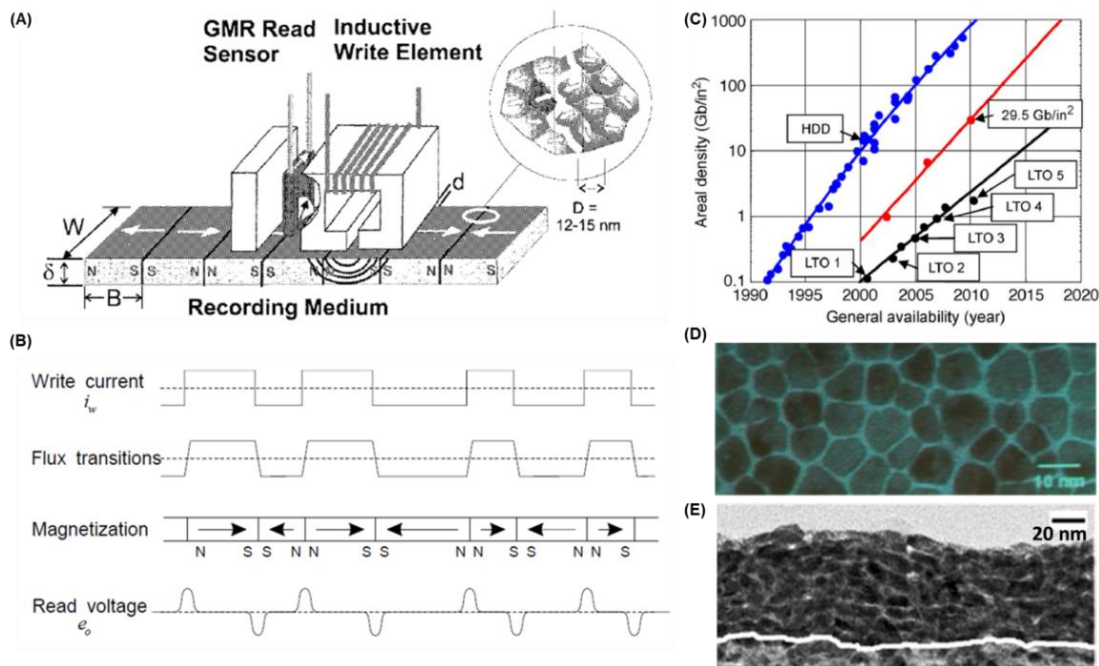
Figure 1-9. (A) Schematic of a longitudinal recording system in HDD.[54] (B) Illustration of the write and read process in the longitudinal recording system. (C) Recent recording areal density enhancement of HDD and magnetic tape recording (LTO is commercial tape product and the red line represents research demonstration of the tape recording).[55] (D) TEM image of the CoCrPtX nanoparticular recording media in HDD.[56] (E) Cross-section TEM image of Ba-ferrite NPs in magnetic tape recording.[55]

Smaller ferromagnetic NPs with high thermal stability are required for future ultrahigh areal density recording in HDD. **Table 1-1** lists possible magnetic recording media materials.[56] The thermally stable grain size D_p is calculated by assuming KV/k_BT

15

= 60 and T = 350 K. Today's HDD recording media is mainly based on CoCrPtX NPs, which can support thermally stable grain size of 7-9 nm and ~750 Gb/in^2 density. However, to further increase the density, smaller recording media is required. $SmCo_5$ and $Fe_{14}Nd_2B$ have smaller D_p, but they have very complicated structures and are not chemically stable. Thus they are mainly used for permanent magnets, not of interest in HDD. $L1_0$-structured FePt (or fct-FePt) is alternative media material for this purpose. Due to very small D_p (~4nm) and not very high T_c (~750 K), it is the key media candidate for the future HDD in heat-assisted magnetic recording. By decreasing the grain size to 3-5 nm, we are expecting to increase the areal density to ~1.5 Tb/in^2.

alloy system	material	K_u (10^7 erg/cm^3)	M_S (emu/cm^3)	H_K (kOe)	T_C (K)	D_p (a) (nm)	D_p (b) (nm)	D_p (c) (nm)	D_p (d) (nm)
Co-alloys	$CoCr_8Pt_{22}$	0.7	500	28.0	1000[a]	7.3	7.5	8.7	6.4
	Co_3Pt	2	1100	36.4	1200	4.3	5.3	6.1	4.5
	$CoPt_3$	0.5	300	33.3	600	8.6	8.3	9.7	7.2
CoX/Pt(Pd) multilayers	Co_3/Pt_{10}	1.2	450	53.3	~700[b]	5.5	6.2	7.2	5.4
	Co_3/Pd_{10}	0.6	360	33.3	~700[b]	7.8	7.8	9.1	6.8
ordered $L1_0/L1_1$ phases	FePd	1.8	1100	32.7	760	4.5	5.4	6.3	4.7
	FePt	7	1140	122.8	750	2.3	3.5	4.0	3.0
	CoPt	4.9	800	122.5	840	2.7	3.9	4.5	3.4
	MnAl	1.7	560	60.7	650	4.7	5.5	6.4	4.8
rare-earth transition metals	$Fe_{14}Nd_2B$	4.6	1270	72.4	585	2.8	4.0	4.6	3.4
	$SmCo_5$	20	910	439.6	1000	1.4	2.4	2.8	2.1

Table 1-1. Possible magnetic media material for extremely high areal density recording in HDD. D_p is the average thermally stable grain diameter assuming $KV/k_BT = 60$ and T = 350 K. [56]

Apart from the HDD recording, there is another important recording media, called magnetic tape recording. The basic concept of the magnetic recording is the same, but

differently the media materials used in magnetic tape are ferrimagnetic materials, like FeCo alloy nanorods and ferrite NPs. Recent development in the areal density of the magnetic tape recording is also shown in **Figure 1-9C**. Even though a big gap between the tape recording and HDD exists, there are several advantages for the tape recording. First of all, the media materials are much cheaper than the Pt-based media in HDD. Secondly, even though the areal density of magnetic tape is much smaller than HDD, its available surface area is much larger than that of HDD, bringing about similar capacity to that of HDD. For example, in the commercial LTO 5 magnetic tape, ~40 nm needle-shape FeCo NPs are used as the recording media. The data cartridge has the dimension of $102 \times 105 \times 21.5$ mm (Length $\times$ Width $\times$ Hight), but contains the tape of ~846 m. The capacity of this tape cartridge is 1.5 TB. The demand for even higher recording density requires the media to be smaller and smaller, and shape anisotropy cannot support such a dimension reduction. Very recently barium-ferrite (BaFe) NPs have attracted lots of attention in tape recording due to their high magnetic anisotropy and chemical stability. A successful demonstration of utilizing oriented BaFe NPs (**Figure 1-9E**) in magnetic tape drives has been achieved, leading to an areal density of 29.5 Gb/in^2.[55] However, BaFe is normally synthesized through conventional solid state chemistry method at very high temperature.[57-59] It is very difficult to control the size and shape of BaFe NPs. In my thesis, I will discuss the chemical methods I developed for synthesizing ferrite NPs (cobalt-ferrite NPs in **Chapter 3** and BaFe NPs in **Chapter 4**) with controlled size and magnetic properties and their potential applications as recording media in magnetic data storage.

17

1.3. Introduction to Nanoparticle Catalysts

As discussed earlier, NPs have very large surface area. The surface unsaturated atoms are highly active to react with other molecules or intermediates, which are of great importance for developing efficient catalysts for specific reactions. Recent advancements in chemical synthesis of NPs with rational size, shape, composition and structure control have led to significant developments of various new and better catalysts. During my Ph. D. study, I also focused on the design and synthesis of metal and metal alloy NPs for catalytic applications, specifically fct-FePt NPs for oxygen reduction reaction (ORR) in proton exchange membrane (PEM) fuel cells and metallic cobalt (Co) NPs for oxygen evolution reaction (OER) in electrochemical water splitting.

1.3.1. Nanoparticle Catalysts for Oxygen Reduction Reaction

In the past few decades, lots of research efforts have been made on renewable and sustainable energy technologies. Among them, PEM fuel cells are a promising technology which converts diverse fuels directly into electrical energy without combustion. **Figure 1-10A** is a typical PEM fuel cell with H_2 as fuel. In the anode, H_2 is oxidized to protons. The generated protons are further migrated in the electrolyte to the cathode through PEM. In the cathode, O_2 is reduced and neutralized by the protons. The electrons go through the external circuit, generating a flow of electricity. The two half reactions in cathode and anode and overall reaction in H_2 PEM fuel cell are listed in **Figure 1-10B**.
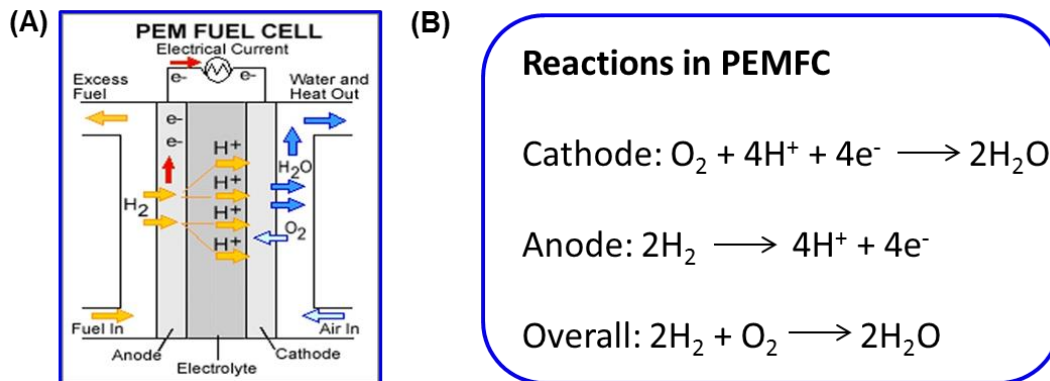
Figure 1-10. (A) A typical PEM fuel cell with H_2 as fuel (Courtesy of the Office of Energy Efficiency and Renewable Energy for the U.S. Department of Energy). (B) Half reactions and overall reaction in a H_2 PEM fuel cell.

However, oxygen reduction reaction (ORR) in a PEM fuel cell is kinetically sluggish and requires a catalyst to lower its electrochemical overpotential and increase the voltage output.[60] Although the exact mechanism of ORR process on a catalyst surface is not well known, density functional theory (DFT) calculations have been utilized to gain some insights into the ORR. For example, possible reaction mechanism on a Pt (111) surface was proposed by DFT calculation of adsorption energies for the surface intermediates.[61] There are two possible mechanisms: one is dissociation mechanism in which the O-O bond is cleaved into adsorbed O, followed by the transfer of proton and electron to it forming OH. The adsorbed OH further reacts with proton and electron to form H_2O and then desorbs from the catalytic surface.

(A) Dissociation Mechanism

$$\frac{1}{2}O_2 + * \rightarrow O*$$

$$O* + H^+ + e^- \rightarrow HO*$$

$$HO* + H^+ + e^- \rightarrow H_2O + *$$

(B) Association Mechanism

$$O_2 + * \rightarrow O_2*$$

$$O_2* + (H^+ + e^-) \rightarrow HO_2*$$

$$HO_2* + (H^+ + e^-) \rightarrow H_2O + O*$$

$$O* + (H^+ + e^-) \rightarrow HO*$$

$$HO* + (H^+ + e^-) \rightarrow H_2O + *$$
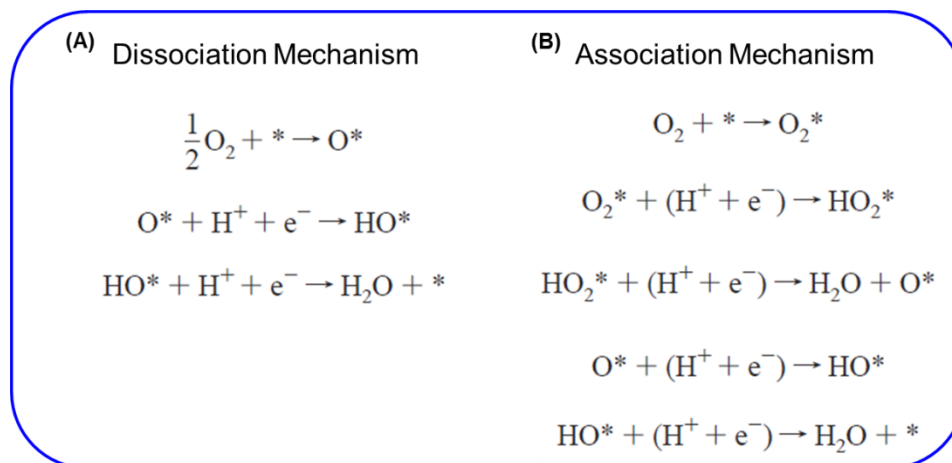
Figure 1-11. Possible reaction mechanism of ORR on a Pt (111) surface. Here * denotes a catalytic site on the Pt (111) surface.[61]

The other mechanism is called association mechanism, in which the adsorbed O_2 does not undergo bond cleavage of O-O, but directly react with proton and electron forming OOH species. Proton and electron are transferred to the adsorbed OOH species, resulting in the formation of adsorbed O and H_2O. Then the adsorbed O undergoes similar reactions as discussed in dissociation mechanism. At lower O_2 coverage, the dissociation has lower energy barrier and dominates the ORR process. However, at high O_2 coverage, the association mechanism has lower energy barrier.

So far, Pt NPs are the state-of-the-art catalyst for ORR, but there is still considerable overpotential for ORR over Pt catalyst. Moreover, Pt itself is not stable enough for long-time fuel cell durability due to dissolution and aggregation.[62] The high price and scarcity of the noble metal Pt also limit the large-scale commercialization of Pt catalyst for ORR. Thus, a rational design of ORR catalysts should not only reduce amount of Pt but also enhance catalytic activity and durability.

Recent advancements in chemical synthesis of Pt-based NPs with precise size, shape, composition and structure control have provided successful approaches to meet those requirements. For example, by designing a Pt thin shell on non-Pt core NPs, the Pt loading in the catalyst can be effectively reduced.[63-65] To further improve catalytic activity, theoretical calculation and experimental results have indicated that by alloy with transition metal M (M = Fe, Co, Ni), the electronic structure of surface Pt atoms can be modified.[66] The formed Pt_3M alloy catalysts exhibit 'volcano-type' catalytic activity, which is determined by a balance between adsorption energies of reactive intermediates and surface coverage by spectator (blocking) species. For bare Pt (111) electrode, the bonding between Pt and adsorbed O is so strong that it is very hard to remove the oxygen species. After alloying with M, the alloy catalysts show lower binding energy with O and thereby accelerate the reaction. As a result, alloying with other M metals into Pt NPs can not only reduce the Pt loading but also enhance the ORR activity.[67-69] Apart from alloy effect of catalyst performance, shape-induced enhancement of both activity and durability for ORR has also been demonstrated in one-dimensional Pt-based nanowires.[70-71] Very recently, structure-induced activity and durability improvements for ORR have been realized in intermetallic CoPt and FePt NPs.[72-73] These improvements are mainly caused by the Pt-Pt bond compress in the intermetallic structure, resulting in a better balance of adsorption/desorption of oxygenated species during ORR. However, high temperature annealing is normally needed to obtain intermetallic structure of those NPs, which will cause NP sintering/aggregation if not treated properly. What's more, even after proper annealing, it is still very difficult to obtain fully ordered intermetallic structure. In **Chapter 6** of my thesis, I will discuss the method I developed for synthesizing fully

ordered fct-FePt NPs with much enhanced activity and durability for ORR in acid solution.

1.3.2. Nanoparticle Catalysts for Oxygen Evolution Reaction

The increasing consumption of fossil fuels and the limited amount of natural resources have motivated us to search for renewable and sustainable energy. Harvesting energy directly from sunlight provides a very promising and viable solution for clean energy. One way is to convert solar energy directly into electricity using photovoltaic cells, which has shown significant advances recently.[18, 74] Alternatively, solar energy can be converted and stored into high-energy chemical bonds through artificial photosynthesis. Among the artificial photosynthesis, photoelectrolysis of water is one of the most promising method to store solar energy in chemical fuel H_2. **Figure 1-12** illustrates the renewable H_2 cycle based on the photoelectrochemical water splitting.[75] Sunlight is utilized and converted into H_2 fuel through electrolysis of H_2O in a water splitting cell. The generated H_2 is then stored, which can be used as a fuel, e.g. to power the PEM fuel cell, generating electricity and releasing H_2O in the atmosphere. However, efficiently photoelectrochemical splitting water into usable H_2 is still challenging. There are basically two requirements for achieving this success: one is efficient utilization of solar energy; the other is enhanced catalytic conversion kinetics of water splitting into hydrogen and oxygen.[76]
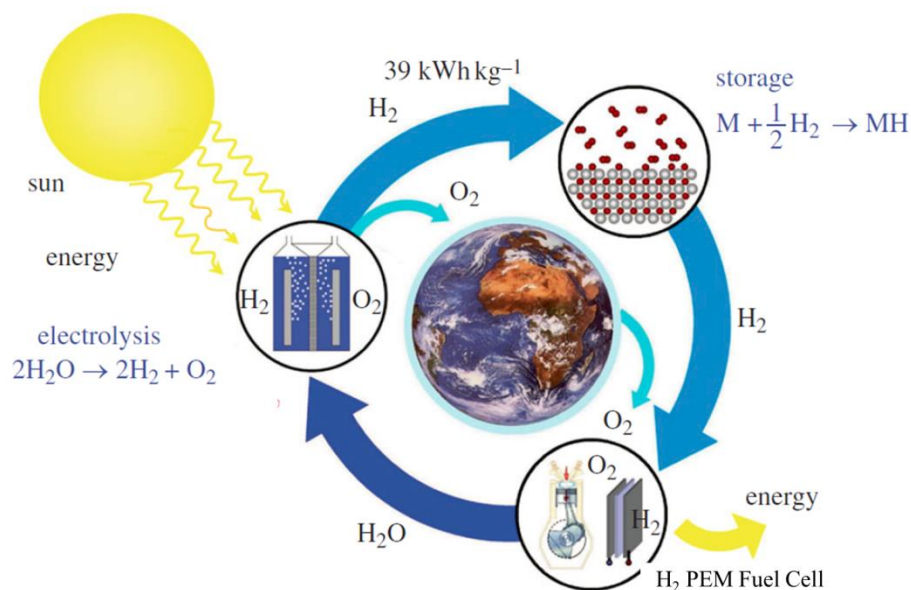
Figure 1-12. The hydrogen cycle: H_2 fuel is generated through photoelectrolysis of water in the splitting cell; the generated H_2 is stored and utilized as a clean fuel to power the PEM fuel cell, generating electricity and heat and releasing water in the atmosphere.[75]

The reactions of water splitting in acidic and alkaline solutions are shown in **Figure 1-13**. Oxygen evolution reaction (OER) takes place at anode while hydrogen evolution reaction (HER) happens at cathode. Ideally, the thermodynamic potential needed to drive the electrolysis of H_2O under standard conditions is $\Delta E = 1.23$ V. The first demonstration of photoelectrolysis of water was done by Honda and Fujishima in 1972, using wide band-gap semiconducting TiO_2 as the light absorber.[77] However, TiO_2 only absorbs UV region of the sunlight, resulting in low solar conversion efficiency.[76]
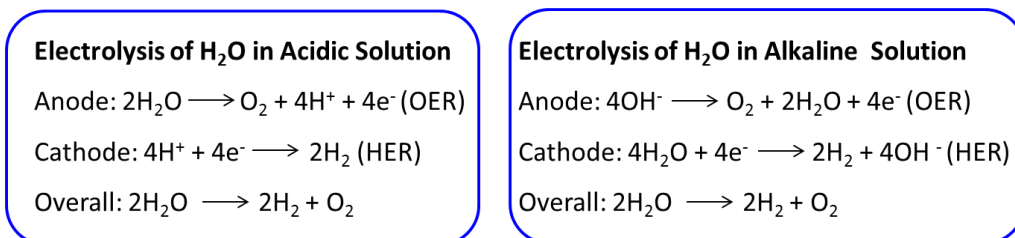
Figure 1-13. OER and HER of water splitting under acidic and alkaline solutions.

23

In order to efficiently harvest a large portion of the solar spectrum, multijunction configurations of semiconductors with different band gaps are needed.[78] Recently there are some promising developments in the designs of semiconducting materials for photoelectrochemical water splitting.[78-81] An efficient solar water splitting cell is proposed in **Figure 1-14**.[82] It contains a membrane-supported assembly of two types of semiconductors with different band gaps: one is p-type semiconductor with narrower band gap as photocathode electrode for HER; the other is n-type semiconductor with wider band gap as photoanode electrode for OER. The membrane is used to physically separate the HER and ORR but at the same time allows protons transfer during reactions.

The dual band gap cell configuration allows more efficient sunlight capture and creates sufficient chemical potential to drive the water-splitting reactions. However, the kinetics of water splitting on the bare semiconductor surface normally limits its efficiency.[78] An overpotential is needed as the driving force to overcome the kinetic barriers for a high reaction rate. Thus addition of a catalyst onto the surface of the semiconductor is needed to further improve the efficiency of water splitting. A catalyst to facilitate reduction of protons to H_2 at the cathode and a catalyst to facilitate oxidation of water to O_2 at the anode are needed, as depicted in **Figure 1-14**.
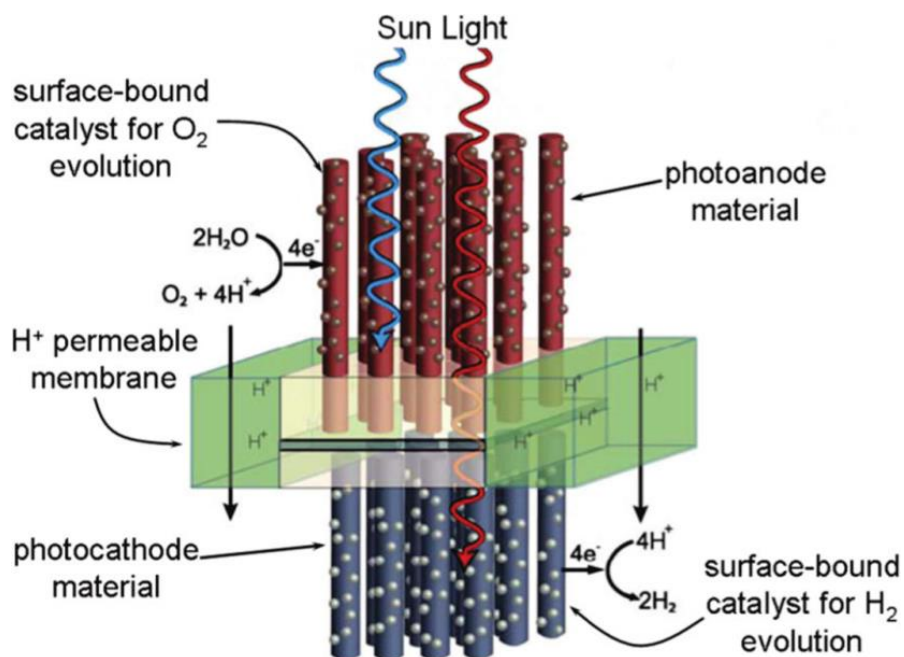
Figure 1-14. A typical solar water-splitting cell in acidic condition with a membrane-supported assembly of two types of semiconductors and electrocatalysts on the surface of semiconductors to promote water splitting.[82]

During my graduate study, I also devoted to develop new efficient catalyst for OER in water splitting. As discussed, OER is a kinetically sluggish reaction, which requires an overpotential to drive its completion. A catalyst is required to lower the overpotential to promote the 4-electron oxidation process. So far, iridium (Ir) and ruthenium (Ru) oxide have been chosen as the state-of-the-art OER catalyst.[83-85] However, just like the Pt catalyst for ORR in PEM fuel cells, the high price and limited sources of the precious metals limit their large-scale commercialization. Moreover, those precious metal oxides are not stable in basic solutions. For example, RuO_2 is subject to dissolution in base to unstable RuO_4.[84] Thus, searching for non-precious catalyst with high electrocatalytic activity and long-term stability is needed for efficient water splitting. Recently, lots of earth-abundant transition metal oxide/hydroxide nanostructures have been developed as

25

promising alternative catalysts for OER, including oxide thin films,[86-88] NPs,[89-94] and layered double hydroxide nanosheets.[95-99] However, these oxides/hydroxide catalysts generally have low electron conductivities, limiting their performance in electrocatalysis enhancement. One strategy to improve the OER catalytic activity of these oxides is to couple them with a conductive support, such as graphene,[95] carbon nanotubes,[97, 100] or metallic Au support.[88, 101-102]   However, these conductive supports can only offer a partial solution to the desired enhancement in catalysis, as the electron transfer required for the OER on the catalytically active surface may only be possible at the catalyst-support interface, not entirely on the catalyst surface. In **Chapter 5**, I will present the stable metallic Co NP catalyst I developed as an efficient OER catalyst. The stable Co NPs were synthesized and stabilized against oxidation via a post reductive annealing. During OER process, the surface metal atoms are oxidized, forming a thin layer of CoO_x. The metallic core acts as a conductive support to enhance its OER activity. Moreover, a monolayer array of metallic Co NP array was fabricated, which exhibits much enhanced activity than the NPs deposited on conventional carbon support. These stable Co NPs are a promising new class of noble-metal-free catalyst for water-splitting.

REFERENCES

[1]   R. P. Feynman, *Eng. Sci.* **1959**, *23*, 22.

[2]   B. D. Gates, Q. B. Xu, M. Stewart, D. Ryan, C. G. Willson, G. M. Whitesides, *Chem. Rev.* **2005**, *105*, 1171-1196.

[3]   N. L. Rosi, C. A. Mirkin, *Chem. Rev.* **2005**, *105*, 1547-1562.

[4]   E. Boisselier, D. Astruc, *Chem. Soc. Rev.* **2009**, *38*, 1759-1782.

[5]   B. L. Cushing, V. L. Kolesnichenko, C. J. O'Connor, *Chem. Rev.* **2004**, *104*, 3893-3946.

[6]   M. Haase, H. Schafer, *Angew. Chem. Int. Ed.* **2011**, *50*, 5808-5829.

[7]   A. H. Lu, E. L. Salabas, F. Schuth, *Angew. Chem. Int. Ed.* **2007**, *46*, 1222-1244.

[8]   D. V. Talapin, J.-S. Lee, M. V. Kovalenko, E. V. Shevchenko, *Chem. Rev.* **2010**, *110*, 389-458.

[9]   J. P. Wilcoxon, B. L. Abrams, *Chem. Soc. Rev.* **2006**, *35*, 1162-1194.

[10]   J. P. Borel, *Surf. Sci.* **1981**, *106*, 1-9.

[11]   D. Ioannou, D. K. Griffin, *Nano Rev.* **2010**, *1*, 5117

[12]   I. L. Medintz, H. T. Uyeda, E. R. Goldman, H. Mattoussi, *Nat. Mater.* **2005**, *4*, 435-446.

[13]   A. M. Smith, S. M. Nie, *Acc. Chem. Res.* **2010**, *43*, 190-200.

[14]   O. Chen, J. Zhao, V. P. Chauhan, J. Cui, C. Wong, D. K. Harris, H. Wei, H. S. Han, D. Fukumura, R. K. Jain, M. G. Bawendi, *Nat. Mater.* **2013**, *12*, 445-451.

[15]   H. S. Jang, H. Yang, S. W. Kim, J. Y. Han, S. G. Lee, D. Y. Jeon, *Adv. Mater.* **2008**, *20*, 2696-2702.

[16]   J. Lim, S. Jun, E. Jang, H. Baik, H. Kim, J. Cho, *Adv. Mater.* **2007**, *19*, 1927-1932.

[17]   V. L. Colvin, M. C. Schlamp, A. P. Alivisatos, *Nature* **1994**, *370*, 354-357.

[18]   C. H. M. Chuang, P. R. Brown, V. Bulovic, M. G. Bawendi, *Nat. Mater.* **2014**, *13*, 796-801.

[19]   W. E. Buhro, V. L. Colvin, *Nat. Mater.* **2003**, *2*, 138-139.

[20]   Y. W. Jun, J. S. Choi, J. Cheon, *Angew. Chem. Int. Ed.* **2006**, *45*, 3414-3439.

[21]   X. C. Ye, L. H. Jin, H. Caglayan, J. Chen, G. Z. Xing, C. Zheng, V. Doan-Nguyen, Y. J. Kang, N. Engheta, C. R. Kagan, C. B. Murray, *ACS Nano* **2012**, *6*, 2804-2817.

[22]   C. J. Murphy, N. R. Jana, *Adv. Mater.* **2002**, *14*, 80-82.

[23]   L. M. Liz-Marzan, *Mater. Today* **2004**, *7*, 26-31.

[24]   L. B. Wang, Y. Y. Zhu, L. G. Xu, W. Chen, H. Kuang, L. Q. Liu, A. Agarwal, C. L. Xu, N. A. Kotov, *Angew. Chem. Int. Ed.* **2010**, *49*, 5472-5475.

[25]   X. Huang, I. H. El-Sayed, W. Qian, M. A. El-Sayed, *J. Am. Chem. Soc.* **2006**, *128*, 2115-2120.

[26]   P. K. Jain, I. H. El-Sayed, M. A. El-Sayed, *Nano Today* **2007**, *2*, 18-29.

[27]   X. J. Xue, F. Wang, X. G. Liu, *J. Mater. Chem.* **2011**, *21*, 13107-13127.

[28]   Y. S. Yu, A. Mendoza-Garcia, B. Ning, S. H. Sun, *Adv. Mater.* **2013**, *25*, 3090-3094.

[29]   I. C. Nlebedim, J. E. Snyder, A. J. Moses, D. C. Jiles, *IEEE Trans. Magn.* **2012**, *48*, 3084-3087.

[30]   Y. W. Jun, J. S. Choi, J. Cheon, *Chem. Commun.* **2007**, 1203-1214.

[31]   B. M. Moskowitz, *Hitchhiker's guide to magnetism* **1991**.

[32] J. H. Lee, Y. M. Huh, Y. Jun, J. Seo, J. Jang, H. T. Song, S. Kim, E. J. Cho, H. G. Yoon, J. S. Suh, J. Cheon, *Nat. Med.* **2007**, *13*, 95-99.

[33] H. B. Na, J. H. Lee, K. J. An, Y. I. Park, M. Park, I. S. Lee, D. H. Nam, S. T. Kim, S. H. Kim, S. W. Kim, K. H. Lim, K. S. Kim, S. O. Kim, T. Hyeon, *Angew. Chem. Int. Ed.* **2007**, *46*, 5397-5401.

[34] J. H. Gao, G. L. Liang, J. S. Cheung, Y. Pan, Y. Kuang, F. Zhao, B. Zhang, X. X. Zhang, E. X. Wu, B. Xu, *J. Am. Chem. Soc.* **2008**, *130*, 11828-11833.

[35] K. Cheng, S. Peng, C. J. Xu, S. H. Sun, *J. Am. Chem. Soc.* **2009**, *131*, 10637-10644.

[36] J. T. Jang, H. Nah, J. H. Lee, S. H. Moon, M. G. Kim, J. Cheon, *Angew. Chem. Int. Ed.* **2009**, *48*, 1234-1238.

[37] T. Hyeon, J. E. Lee, N. Lee, H. Kim, J. Kim, S. H. Choi, J. H. Kim, T. Kim, I. C. Song, S. P. Park, W. K. Moon, *J. Am. Chem. Soc.* **2010**, *132*, 552-557.

[38] D. Ho, X. Sun, S. Sun, *Acc. Chem. Res.* **2011**, *44*, 875-882.

[39] S. Peng, S. H. Sun, *Angew. Chem. Int. Ed.* **2007**, *46*, 4155-4158.

[40] S. Peng, C. Wang, J. Xie, S. H. Sun, *J. Am. Chem. Soc.* **2006**, *128*, 10676-10677.

[41] C. J. Xu, B. D. Wang, S. H. Sun, *J. Am. Chem. Soc.* **2009**, *131*, 4216-4217.

[42] S. H. Sun, L. L. Lacroix, L. M., N. F. Huls, D. Ho, X. L. Sun, K. Cheng, *Nano Lett.* **2011**, *11*, 1641-1645.

[43] C. Wang, Y. J. Wei, H. Y. Jiang, S. H. Sun, *Nano Lett.* **2009**, *9*, 4544-4547.

[44] Y. L. Hou, Z. C. Xu, S. Peng, C. B. Rong, J. P. Liu, S. H. Sun, *Adv. Mater.* **2007**, *19*, 3349-3352.

[45] S. H. Sun, C. B. Murray, D. Weller, L. Folks, A. Moser, *Science* **2000**, *287*, 1989-1992.

[46] J. M. Kim, C. B. Rong, J. P. Liu, S. H. Sun, *Adv. Mater.* **2009**, *21*, 906-909.

[47] J. Kim, C. Rong, Y. Lee, J. P. Liu, S. Sun, *Chem. Mater.* **2008**, 7242–7245.

[48] L. M. Lacroix, N. F. Huls, D. Ho, X. L. Sun, K. Cheng, S. H. Sun, *Nano Lett.* **2011**, *11*, 1641-1645.

[49] C. Wang, S. Peng, L. M. Lacroix, S. H. Sun, *Nano Res.* **2009**, *2*, 380-385.

[50] E. F. Kneller, R. Hawig, *IEEE Trans. Magn.* **1991**, *27*, 3588-3600.

[51] R. Skomski, J. M. D. Coey, *Phys. Rev. B* **1993**, *48*, 15812-15816.

[52] H. Zeng, J. Li, J. P. Liu, Z. L. Wang, S. H. Sun, *Nature* **2002**, *420*, 395-398.

[53] F. Liu, J. H. Zhu, W. L. Yang, Y. H. Dong, Y. L. Hou, C. Z. Zhang, H. Yin, S. H. Sun, *Angew. Chem. Int. Ed.* **2014**, *53*, 2176-2180.

[54] D. Weller, A. Moser, *IEEE Trans. Magn.* **1999**, *35*, 4423-4439.

[55] G. Cherubini, R. D. Cideciyan, L. Dellmann, E. Eleftheriou, W. Haeberle, J. Jelitto, V. Kartik, M. A. Lantz, S. Olcer, A. Pantazi, H. E. Rothuizen, D. Berman, W. Imaino, P. O. Jubert, G. McClelland, P. V. Koeppe, K. Tsuruta, T. Harasawa, Y. Murata, A. Musha, H. Noguchi, H. Ohtsu, O. Shimizu, R. Suzuki, *IEEE Trans. Magn.* **2011**, *47*, 137-147.

[56] D. Weller, O. Mosendz, G. Parker, S. Pisana, T. S. Santos, *Phys. Status Solidi A* **2013**, *210*, 1245-1260.

[57] J. Jalli, Y. K. Hong, S. Bae, G. S. Abo, J. J. Lee, J. C. Sur, S. H. Gee, S. G. Kim, S. C. Erwin, A. Moitra, *IEEE Trans. Magn.* **2009**, *45*, 3590-3593.

[58] D. Lisjak, S. Ovtar, *J. Phys. Chem. B* **2013**, *117*, 1644-1650.

[59]   A. Yourdkhani, D. Caruntu, A. K. Perez, G. Caruntu, *J. Phys. Chem. C* **2014**, *118*, 1774-1782.

[60]   Y. H. Bing, H. S. Liu, L. Zhang, D. Ghosh, J. J. Zhang, *Chem. Soc. Rev.* **2010**, *39*, 2184-2202.

[61]   J. K. Norskov, J. Rossmeisl, A. Logadottir, L. Lindqvist, J. R. Kitchin, T. Bligaard, H. Jonsson, *J. Phys. Chem. B* **2004**, *108*, 17886-17892.

[62]   Y. J. Wang, D. P. Wilkinson, J. J. Zhang, *Chem. Rev.* **2011**, *111*, 7625-7651.

[63]   S. Zhang, Y. Z. Hao, D. Su, V. V. T. Doan-Nguyen, Y. T. Wu, J. Li, S. H. Sun, C. B. Murray, *J. Am. Chem. Soc.* **2014**, *136*, 15921-15924.

[64]   Y. J. Kang, J. Snyder, M. F. Chi, D. G. Li, K. L. More, N. M. Markovic, V. R. Stamenkovic, *Nano Lett.* **2014**, *14*, 6361-6367.

[65]   C. Wang, D. van der Vliet, K. L. More, N. J. Zaluzec, S. Peng, S. H. Sun, H. Daimon, G. F. Wang, J. Greeley, J. Pearson, A. P. Paulikas, G. Karapetrov, D. Strmcnik, N. M. Markovic, V. R. Stamenkovic, *Nano Lett.* **2011**, *11*, 919-926.

[66]   V. R. Stamenkovic, B. S. Mun, M. Arenz, K. J. J. Mayrhofer, C. A. Lucas, G. F. Wang, P. N. Ross, N. M. Markovic, *Nat. Mater.* **2007**, *6*, 241-247.

[67]   S. I. Choi, S. F. Xie, M. H. Shao, J. H. Odell, N. Lu, H. C. Peng, L. Protsailo, S. Guerrero, J. H. Park, X. H. Xia, J. G. Wang, M. J. Kim, Y. N. Xia, *Nano Lett.* **2013**, *13*, 3420-3425.

[68]   C. Wang, M. F. Chi, D. G. Li, D. van der Vliet, G. F. Wang, Q. Y. Lin, J. F. Mitchell, K. L. More, N. M. Markovic, V. R. Stamenkovic, *ACS Catal.* **2011**, *1*, 1355-1359.

[69]   C. Wang, G. F. Wang, D. van der Vliet, K. C. Chang, N. M. Markovic, V. R. Stamenkovic, *Phys. Chem. Chem. Phys.* **2010**, *12*, 6933-6939.

[70]   S. J. Guo, D. G. Li, H. Y. Zhu, S. Zhang, N. M. Markovic, V. R. Stamenkovic, S. H. Sun, *Angew. Chem. Int. Ed.* **2013**, *52*, 3465-3468.

[71]   H. Zhu, S. Zhang, D. Su, G. Jiang, S. Sun, *Small* **2015**.

[72]   D. L. Wang, H. L. L. Xin, R. Hovden, H. S. Wang, Y. C. Yu, D. A. Muller, F. J. DiSalvo, H. D. Abruna, *Nat. Mater.* **2013**, *12*, 81-87.

[73]   S. Zhang, X. Zhang, G. Jiang, H. Zhu, S. Guo, D. Su, G. Lu, S. Sun, *J. Am. Chem. Soc.* **2014**, *136*, 7734-7739.

[74]   N. J. Jeon, J. H. Noh, W. S. Yang, Y. C. Kim, S. Ryu, J. Seo, S. I. Seok, *Nature* **2015**, *517*, 476-480.

[75]   A. Zuttel, A. Remhof, A. Borgschulte, O. Friedrichs, *Phil. Trans. R Soc. A* **2010**, *368*, 3329-3342.

[76]   D. Kim, K. K. Sakimoto, D. Hong, P. Yang, *Angew. Chem. Int. Ed.* **2015**, *54*, 3259-3266.

[77]   A. Fujishima, K. Honda, *Nature* **1972**, *238*, 37-38.

[78]   M. G. Walter, E. L. Warren, J. R. McKone, S. W. Boettcher, Q. X. Mi, E. A. Santori, N. S. Lewis, *Chem. Rev.* **2010**, *110*, 6446-6473.

[79]   H. M. Chen, C. K. Chen, R. S. Liu, L. Zhang, J. J. Zhang, D. P. Wilkinson, *Chem. Soc. Rev.* **2012**, *41*, 5654-5671.

[80]   T. Hisatomi, J. Kubota, K. Domen, *Chem. Soc. Rev.* **2014**, *43*, 7520-7535.

[81]   A. Kudo, Y. Miseki, *Chem. Soc. Rev.* **2009**, *38*, 253-278.

[82]   I. Yahyaie, K. McEleney, M. Walter, D. R. Oliver, D. J. Thomson, M. S. Freund, N. S. Lewis, *J. Phys. Chem. Lett.* **2011**, *2*, 675-680.

[83]   M. Yagi, E. Tomita, T. Kuwabara, *J. Electroanal. Chem.* **2005**, *579*, 83-88.

[84]   M. Yagi, E. Tomita, S. Sakita, T. Kuwabara, K. Nagai, *J. Phys. Chem. B* **2005**, *109*, 21489-21491.

[85]   Y. Lee, J. Suntivich, K. J. May, E. E. Perry, Y. Shao-Horn, *J. Phys. Chem. Lett.* **2012**, *3*, 399-404.

[86]   Y. Gorlin, T. F. Jaramillo, *J. Am. Chem. Soc.* **2010**, *132*, 13612-13614.

[87]   L. Trotochaud, S. L. Young, J. K. Ranney, S. W. Boettcher, *J. Am. Chem. Soc.* **2014**, *136*, 6744-6753.

[88]   B. S. Yeo, A. T. Bell, *J. Am. Chem. Soc.* **2011**, *133*, 5587-5593.

[89]   F. Jiao, H. Frei, *Angew. Chem. Int. Ed.* **2009**, *48*, 1841-1844.

[90]   J. Masa, W. Xia, I. Sinev, A. Q. Zhao, Z. Y. Sun, S. Grutzke, P. Weide, M. Muhler, W. Schuhmann, *Angew. Chem. Int. Ed.* **2014**, *53*, 8508-8512.

[91]   A. J. Esswein, M. J. McMurdo, P. N. Ross, A. T. Bell, T. D. Tilley, *J. Phys. Chem. C* **2009**, *113*, 15068-15072.

[92]   M. R. Gao, Y. F. Xu, J. Jiang, Y. R. Zheng, S. H. Yu, *J. Am. Chem. Soc.* **2012**, *134*, 2930-2933.

[93]   T. Y. Ma, S. Dai, M. Jaroniec, S. Z. Qiao, *J. Am. Chem. Soc.* **2014**, *136*, 13925-13931.

[94]   L. B. Liao, Q. H. Zhang, Z. H. Su, Z. Z. Zhao, Y. N. Wang, Y. Li, X. X. Lu, D. G. Wei, G. Y. Feng, Q. K. Yu, X. J. Cai, J. M. Zhao, Z. F. Ren, H. Fang, F. Robles-Hernandez, S. Baldelli, J. M. Bao, *Nat. Nanotechnol.* **2014**, *9*, 69-73.

[95] X. Long, J. K. Li, S. Xiao, K. Y. Yan, Z. L. Wang, H. N. Chen, S. H. Yang, *Angew. Chem. Int. Ed.* **2014**, *53*, 7584-7588.

[96] D. Friebel, M. W. Louie, M. Bajdich, K. E. Sanwald, Y. Cai, A. M. Wise, M. J. Cheng, D. Sokaras, T. C. Weng, R. Alonso-Mori, R. C. Davis, J. R. Bargar, J. K. Norskov, A. Nilsson, A. T. Bell, *J. Am. Chem. Soc.* **2015**, *137*, 1305-1313.

[97] M. Gong, Y. Li, H. Wang, Y. Liang, J. Z. Wu, J. Zhou, J. Wang, T. Regier, F. Wei, H. Dai, *J. Am. Chem. Soc.* **2013**, *135*, 8452-8455.

[98] F. Song, X. L. Hu, *J. Am. Chem. Soc.* **2014**, *136*, 16481-16484.

[99] Y. Zhang, B. Cui, C. S. Zhao, H. Lin, J. B. Li, *Phys. Chem. Chem. Phys.* **2013**, *15*, 7363-7369.

[100] A. Q. Zhao, J. Masa, W. Xia, A. Maljusch, M. G. Willinger, G. Clavel, K. P. Xie, R. Schlogl, W. Schuhmann, M. Muhlert, *J. Am. Chem. Soc.* **2014**, *136*, 7551-7554.

[101] Z. B. Zhuang, W. C. Sheng, Y. S. Yan, *Adv. Mater.* **2014**, *26*, 3950-3955.

[102] Y. Gorlin, C. J. Chung, J. D. Benck, D. Nordlund, L. Seitz, T. C. Weng, D. Sokaras, B. M. Clemens, T. F. Jaramillo, *J. Am. Chem. Soc.* **2014**, *136*, 4920-4926.

Chapter 2. Chemical Synthesis and Self-Assembly of

Monodisperse Nanoparticles

2.1. Chemical Synthesis of Monodisperse Nanoparticles

As the chemical and physical properties of nanoparticles (NPs) are strongly dependent on their size, shape and composition, in the past few decades, lots of research efforts have been made on designing efficient synthetic methods to well-defined NPs with precise size, shape and composition control. Liquid-phase colloidal method provides a powerful tool to achieve this. In the early stage of colloidal synthesis, NPs were mainly synthesized in hydrolytic (e.g. aqueous) solutions. Lots of metal and metal oxide NPs were obtained through sol-gel process, microemulsion process and hydrothermal methods, which were well summarized in the review article.[1] However, NPs synthesized by this method generally suffer from low crystallinity or large size distribution. An alternative way is using high-boiling point organic solvent instead of hydrolytic solvent. NPs synthesized through this organic-phase colloidal method have much better crystallinity and monodispersity. They can be well controlled in size, shape, and composition by changing the reaction parameters, such as precursor concentrations, the reaction temperatures, and the surfactants used. Moreover, NPs with different architectures such as core/shell type, dumbbell type or even more complex morphologies can be achieved. There are several excellent review articles on the synthesis of inorganic NPs using the organic-phase colloidal method.[2-5] During my graduate study, I focused on this organic solution synthesis of monodisperse metal and metal oxide NPs with controlled shape, size and composition.

2.1.1. Formation Mechanism of Monodisperse Nanoparticles

The widely accepted formation mechanism of monodisperse NPs is based on the concept of "burst nucleation" proposed by LaMer.[6] The LaMer model describing the nucleation and growth process of monodisperse NPs synthesis is shown in **Figure 2-1**.[7] "Burst nucleation" is an important concept in guiding the synthesis. The concentration of "monomers" or "precursors" continues to increase as the reaction time increases. The nucleation threshold is the supersaturation of those monomers. If the concentration of monomers is rapidly increased above the nucleation threshold, then "burst nucleation" takes place, resulting in the formation of nuclei and at the same time the rapid decrease of the monomer concentration. When the concentration level drops below the nucleation threshold, no new nuclei form. The reaction comes to the growth stage, in which the monomers attached to the formed nuclei to facilitate the NP growth. The growth process will keep going as long as the monomer concentration is above the saturation level. In order to synthesize monodisperse NPs, it is required to separate the nucleation process from the subsequent growth process.
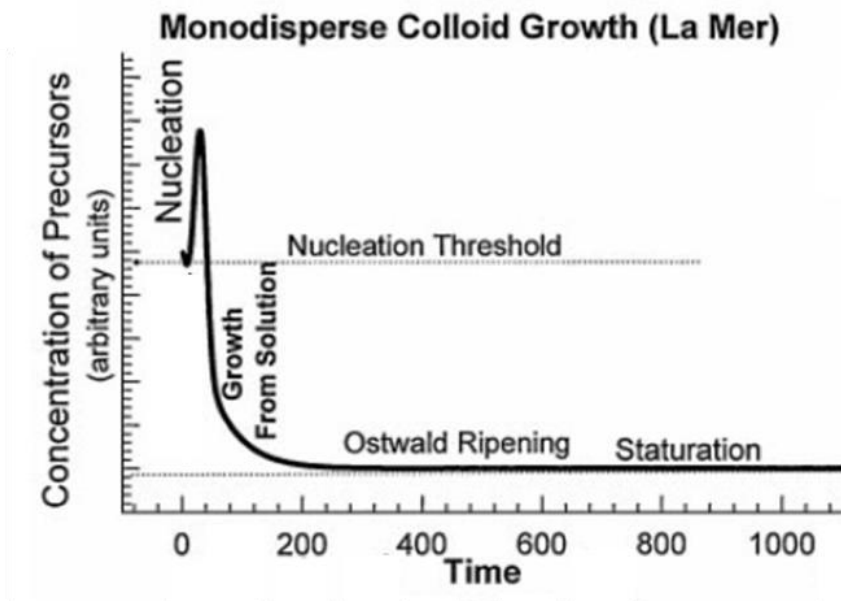
Figure 2-1. LaMer model of the nucleation and growth process of synthesizing monodisperse nanoparticles.[7]

Basically there are two techniques for achieving efficient "burst nucleation" for monodisperse NP synthesis. One is "hot-injection" method. This method was introduced by Bawendi and his coworkers on the synthesis of monodisperse CdE (E = S, Se and Te) semiconductor NPs about two decades ago.[8] During the synthesis, the rapid injection of precursors in surfactant solvent at high temperature generated high degree supersaturation, causing burst nucleation and the formation of monodisperse NPs. The cartoon depicting the "hot-injection" synthesis of monodisperse NPs is shown in **Figure 2-2**.[4] This "hot-injection" method has been well extended to some other semiconductor and metal NPs synthesis.[7]
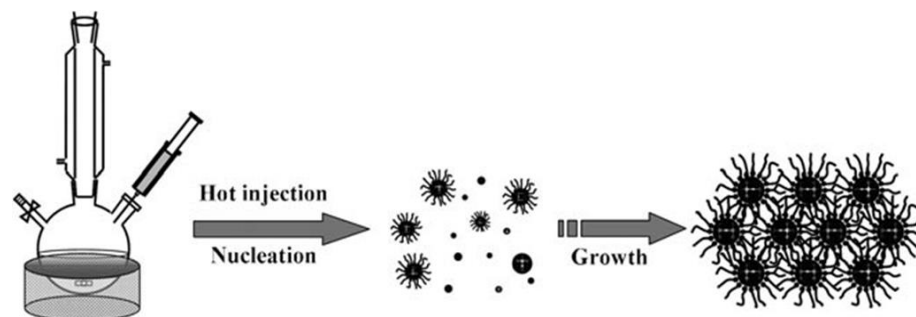
Figure 2-2. "Hot-injection" synthesis of monodisperse nanoparticles.[4]

The other method is call "heating-up" method, in which the precursors, surfactants and solvent are mixed together at low temperature and subsequently heated up to a certain temperature to initiate the nucleation and growth process. This process can also generate very uniform NPs. Moreover, it is very convenient for a large-scale synthesis. The "heating-up" method is especially powerful for metal oxide NP synthesis.[9-11]

Typically the organic-phase colloidal synthesis utilizes high boiling organic solvents (180 ~ 350 ^{o}C) including 1-octadecene, benzylether, 1,2-dichlorobenzene and 1,2,3,4-tetrahydronaphthalene. It also needs appropriate surfactants to stabilize the formed NPs. Typical surfactants include long-chain carboxylic acids (e.g. oleic acid), alkylamines (e.g. oleylamine), alkyl phosphines and alkylphosphine oxides (e.g. trioctylphosphine and trioctylphosphine oxide).

2.1.2. Chemical Synthetic Routes for Monodisperse Nanoparticles

As discussed above, organic-phase colloidal synthesis provides a powerful method for synthesizing monodisperse NPs based on the LaMer model. In the past few decades, significant progress has been made on the controlled synthesis of monodisperse NPs through this colloidal method. As my Ph. D. work is mainly focused on the synthesis and

self-assembly of monodisperse metal and metal oxide NPs, I will briefly summarize the synthetic routes in colloidal synthesis of those NPs we have achieved in our lab.

There are mainly two approaches to monodisperse metal NPs: reduction of metal salts and thermal decomposition of metal compounds. A representative example of reducing metal salt precursors to uniform metallic NPs is Au NP synthesis. Using $HAuCl_4$ as the precursor, monodisperse Au NPs have been successfully synthesized with tert-butylamine-borane complex as the reducing agent.[12] **Figure 2-3A** shows a TEM image of self-assembled 6 nm Au superlattice. By tuning the reaction temperature, the kinetics of the nucleation and growth process can be controlled to synthesize monodisperse Au NPs with the size range of $2 - 10$ nm. Thermal decomposition of metal organic compounds has also been widely used to synthesize monodisperse metal NPs. For instance, monodisperse Fe NPs have been synthesized by thermal decomposition of $Fe(CO)_5$ with oleylamine as the surfactant, as shown in **Figure 2-3B**. Due to the oxidation of Fe upon air oxidation, a layer of Fe_3O_4 shell was formed on the metallic Fe NPs. The size of the final Fe NPs can be easily adjusted by changing the amount of the precursors and the surfactants. Similarly, monodisperse Co NPs can be produced through the thermal decomposition of $Co_2(CO)_8$.[13]
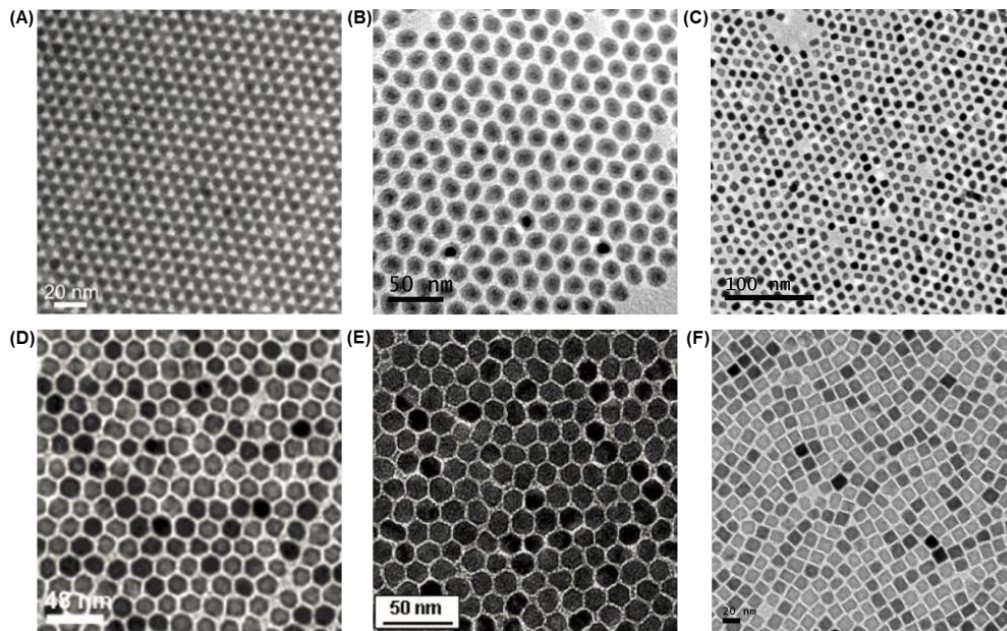
Figure 2-3. TEM images of some representative monodisperse NPs synthesized in our group. (A) 6 nm Au NPs.[12] (B) 13 nm Fe NPs with an oxide layer upon air exposure. (C) 9 nm FePt NPs. (D) 16 nm Fe_3O_4 NPs.[9] (E) 14 nm $CoFe_2O_4$ NPs.[11] (F) 15 nm $Co_{0.6}Fe_{2.4}O_3$ NPs.[31]

Compared to the single element metal NPs, bimetallic NPs are somehow more difficult to synthesize with precise size and composition control. One way is to synthesize single element metal NPs first and then dope the other element into the metal NPs to form uniform alloy (e.g. FeCo,[14] AuAg[15] and MnAu[16] alloy NPs). Another way is to directly form monodisperse alloy NPs, as shown in the FePt case.[17] The FePt synthesis combines the reduction of metal salt and thermal decomposition of metal compound together. It uses $Fe(CO)_5$ as Fe precursor. Thermal decomposition of $Fe(CO)_5$ generate CO, which can be used as the reducing agent to reduce $Pt(acac)_2$ to $Pt(0)$. The composition can be readily tuned by changing the initial precursor ratio. More importantly, the reaction kinetics can be controlled by changing the amount and ratio of the surfactants (oleic acid and oleylamine), leading to precise size and shape control.[18-19] **Figure 2-3C** shows a typical TEM image of 9 nm cubic FePt NPs. More examples about

41

using the surfactant molecules to direct the kinetics of nucleation and growth process in NP synthesis can be found in this review article.[3]

Metal oxides NPs, especially magnetic ferrite NPs, are a main research project in our group due to their great potential applications in magnetic recording and biological applications. In our group, we utilize organic-phase colloidal synthesis to make monodisperse metal oxide NPs. For example, monodisperse iron oxide NPs were synthesized in high boiling solvent (e.g. benzyl ether) using the "heating-up" method through the thermal decomposition of $Fe(acac)_3$ with oleic acid and oleylamine as the surfactants.[9] Figure **2-3D** shows a TEM image of 16 nm monodisperse Fe_3O_4 NPs. By substituting part of $Fe(acac)_3$ with $Co(acac)_2$ or $Mn(acac)_2$, monodisperse Co ferrite or Mn ferrite NPs were synthesized (**Figure 2-3E**).[11] Very recently, we found that using sodium oleate instead of oleylamine, preferential growth of Co ferrite NPs along the <111> direction can be achieved and cubic Co ferrite NPs can be synthesized (**Figure 2-3F**).[31] These ferrimagnetic NPs are of great potential applications in magnetic recording, which I will discuss in details in **Chapter 3**.

2.2. Self-Assembly of Monodisperse Nanoparticles

Self-Assembly of NPs is of great importance for bottom-up fabrication of functional devices. Recent advances in the synthesis of monodisperse NPs with precise control over the size and shape allow us to assemble them into well-defined patterns, such as 2D monolayers[20-22] and 3D superlattices.[23-27] There are several techniques for self-assembling NPs on solid substrates, including drop-casting,[22, 28] and spin-coating.[29-30] However, it is hard to control the thickness and size of the assembly through drop-casting

method. Spin-coating is a convenient way to fabricate well-assembled film with the thickness of several hundred nanometers, but it is difficult to make ultrathin assemblies, especially dense-packed monolayers.
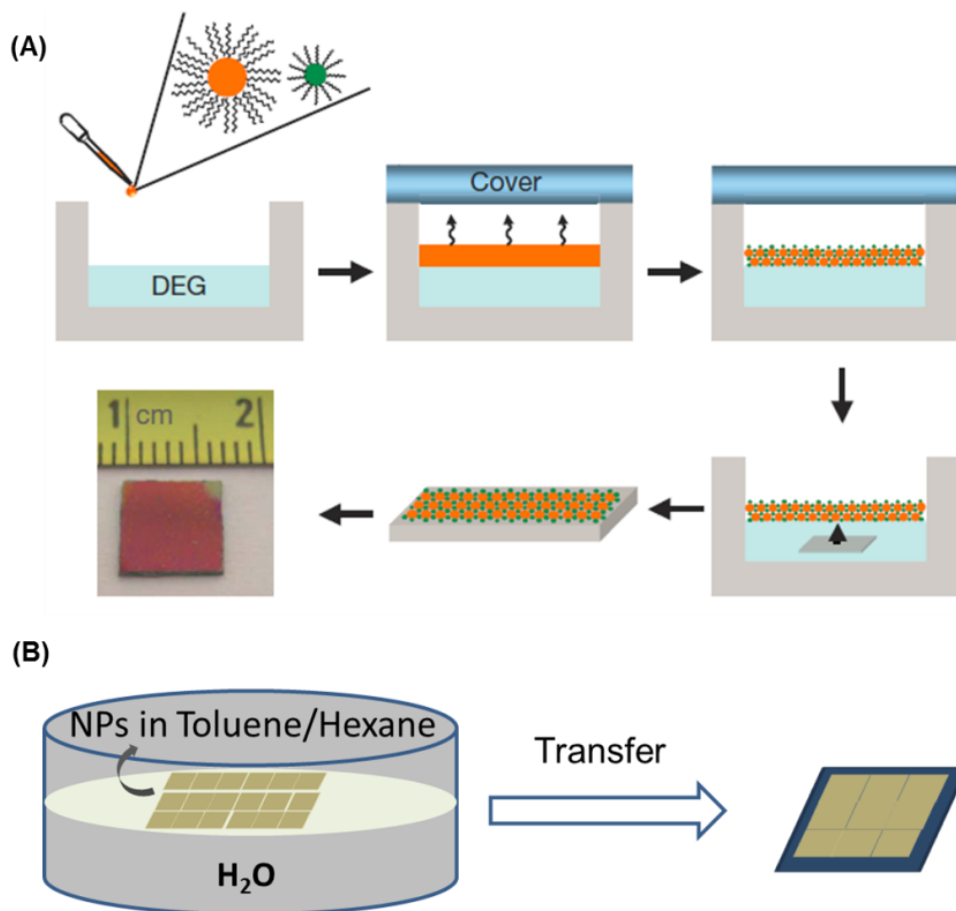
Figure 2-4. (A) Schematic illustration of the liquid-air interfacial assembly of binary superlattices.[25] (B) Schematic illustration of the water-air interfacial assembly of monolayer nanoparticles.

Very recently, Murray group developed a liquid-air interfacial assembly method of preparing centimeter-scale binary superlattices.[25] The concept is shown in **Figure 2-4A**. The binary NPs dispersion in hexane with desired amount was drop-cast on the surface of diethylene glycol (DEG) in a Teflon well. The well was covered with a glass slide to

allow the hexane to evaporate slowly in about 10 min. Upon the complete evaporation of the organic solvent, the assembled film formed on the surface of DEG could be readily transferred to solid substrates for further characterization. There are two major benefits of this liquid-air interfacial assembly: one is the formation of large-area assembly with control architecture; the other is the ease of transferring the assembly on any arbitrary substrates to fabricate devices.

Inspired by this liquid-air assembly method, large-area monolayer assembly of NPs can be fabricate through similar method.[21] The water-air interfacial assembly I developed is shown in **Figure 2-4B**. Here, water was used instead of DEG, which makes the drying of the assembled film much easier. The NPs were dispersed in the mixture of toluene and hexane (volume ratio = 1 : 1), in which the toluene can slow down the evaporation rate of the organic solvent and as a result favor the assembly process. After the complete evaporation of the solvent, densely packed assemblies of the monodisperse NPs were formed on the water surface, which could be easily transferred onto a Cu TEM grid, Si wafer or glassy carbon support for further characterizations. The thickness of the assembly can be tuned by the initial amount of the NP dispersion, which can form monolayer, bilayer or even thicker assemblies. I will discuss more about the monolayer assembly of the $Co_{0.4}Fe_{2.4}O_4$ NPs for magnetic recording in **Chapter 3**. Moreover, this assembly process can be extended to the assembly of Ba-doped iron oxide NPs for permant magnet and magnetic recording applications, which will be included in **Chapter 4**. A detailed study of well-defined monolayer catalyst of Co NPs for oxygen evolution reaction will be discussed in **Chapter 5**.

2.3. Organic-Phase Colloidal Synthesis: Experimental Section

2.3.1. Experimental Setup

A typical experimental set-up to synthesized monodisperse NPs in our lab is shown in **Figure 2-5.** We use the Schlenk line to provide inert gas to protect the synthesis from oxygen and moisture. A four-neck flask is used as the reaction vessel for the NP synthesis. During synthesis, the organic solvent in the flask is stirred by a stirring bar and a stirring plate. The reaction vessel is heated using a hemisphere heating mantle. One neck of the flask is connected to the thermal couple of the temperature controller to control the reaction temperature. One is connected to a gas (e.g. Ar or N_2) inlet of the Schlenk line and another is connected to the gas outlet trap. The extra neck is usually covered with a rubber septum for adding any chemicals inside the reaction system if needed.
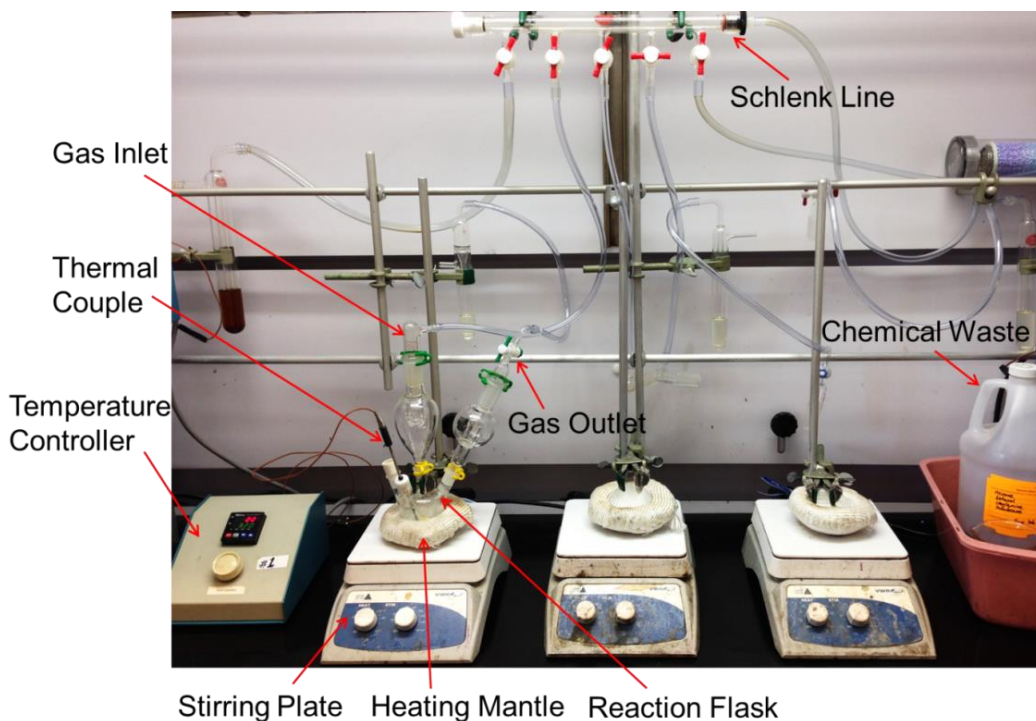
Figure 2-5. A typical experimental setup for colloidal synthesis of monodisperse NPs.

The chemicals used for the organic-phase colloidal synthesis include the solvent, metal precursors, surfactants, and reducing agents (if necessary). Most of the chemicals we used were purchased from Strem Chemicals (e.g. metal acetylacetonate, metal stearate and cobalt carbonyl) or Sigma Aldrich (e.g. surfactants: oleic acid and oleylamine; solvents: 1-octadecent, benzyl ether and 1,2-dichlorobenzene) without further purification. The reaction temperature and heating rate are well controlled by the controller to obtain desired conditions for monodisperse NP formation.

Figure 2-6. Photograph of 10 nm CoFe$_2$O$_4$ NPs dispersion in hexane.

2.3.2. Nanoparticle Collection and Purification

After the reaction, the formed NPs are precipitated out from the solution by adding a non-solvent, such as ethanol, isopropanol or acetone. The precipitation of NPs is then collected by centrifugation using a Beckman Coulter Allegra® 64R Centrifuge (8500 rpm, 5 ~ 10 min). The NPs are then re-dispersed in non-polar solvent (e.g. hexane, toluene or

chloroform) and separated again using non-solvent followed by centrifugation. This washing step is usually repeated two or three times to clean the NPs. During each step, few droplets of surfactants are sometimes added to better cover the surface of NPs. The final product is re-dispersed in non-polar solvent and stored for further characterization and use. **Figure 2-6** shows a photograph of 10 nm $CoFe_2O_4$ NPs synthesized two years ago. They are very stable in hexane. Some metal NPs (e.g. bcc-Fe and fcc-Co NPs) are not stable in air which can be gradually oxidized. These air-sensitive NPs should be stored in inert atmosphere in glove box for long-term use.

2.4. Material Characterization

There are various characterization techniques available to investigate the properties of the synthesized NPs. The typical characterization methods I used during my Ph. D. study are listed below.

2.4.1. Transmission Electron Microscopy

Transmission electron microscopy (TEM) is the most common equipment used to characterize the size and morphology of the NPs. The TEM images were collected on a Philips CM20 microscopy with an operating voltage of 200 kV at Brown University. To prepare the sample for TEM analysis, typically a droplet of dilute NP dispersion in hexane was deposited on an amorphous carbon coated Cu TEM grid (Ted Pella). For the monolayer assembly, it can be easily transferred onto a TEM grid for morphology analysis. High-resolution TEM is even powerful which can analyze the lattice distance of the crystalline NPs. HR-TEM images were recorded using a JEOL 2010 with an

accelerating voltage of 200 kV. The sample preparation is the same as regular TEM sample.

2.4.2. X-ray Diffraction

X-ray diffraction (XRD) is an important technique used to determine the crystalline structure of the synthesized NPs. XRD patterns of the NPs were collected on a Bruker AXS D8-Advanced diffractometer with Cu Kα radiation (λ = 1.5418 Å). In order to prepare sample for XRD, NPs need to be dried into powder or form a thick film on a glass or Si substrate by drop-casting concentrated NP dispersion. Based on the standard patterns, the crystalline structure of the NPs can be analyzed. Moreover, using Scherrer equation, the size of the NPs can be roughly determined, which can be coupled with the size analysis from TEM study.

2.4.3. Scanning Electron Microscopy

Scanning electron microscopy (SEM) is another EM technique for studying the size and morphology of NPs, although the resolution is not as high as TEM. SEM images were acquired on a LEO 1530 microscope at an accelerating voltage of 10 kV. To prepare samples for SEM, conductive substrates such as Si substrates are needed. Typically, NPs dispersion was deposited on a Si substrate. For characterizing the morphology of monolayer pattern of the assembly, the assembly was transferred on a Si substrate and let dry under ambient condition. SEM can not only analyze the morphology, but also can perform elemental analysis. Equipped with an energy-dispersive X-ray (EDX)

spectroscopy, this equipment can analyze the characteristic X-ray emission spectrum of the elements inside the NPs and thus can measure elemental composition of the specimen.

2.4.4. Scanning Transmission Electron Microscopy

The recent advances in EM technology allow us to study the atomic structure in a single NP that tradition TEM or SEM cannot achieve. Taking the intermetallic face-centered tetragonal (fct) FePt NPs as an example, regular TEM cannot show the intermetallic structure. However, scanning transmission electron microscopy (STEM) can provide detailed elemental distribution and atomic structures of a NP. STEM analysis were carried out on a Hitachi HD2700C (200 kV) with a probe aberration corrector, at the Center for Functional Nanomaterials, Brookhaven National Lab. The electron energy loss spectroscopy (EELS) in STEM measurement makes elemental identification possible, which is capable of determining the intermetallic structure. The EELS line-scan was obtained by a high-resolution Gatan-Enfina ER with a probe size of 1.3 Å. Sample preparation is similar to that of TEM sample.

2.4.5. Inductively Coupled Plasma Atomic Emission Spectroscopy

EDX can provide some accurate elemental information of NPs, but a more accurate elemental analysis can be done by the inductively coupled plasma-atomic emission spectroscopy (ICP-AES) measurements, which were carried on a JY2000 Ultrace ICP atomic emission spectrometer equipped with a JY AS 421 autosampler and 2400g/mm holographic grating. To prepare the sample, a few droplets of NP dispersion were dried in a 20 mL glass vial. Then 1 mL of aqua regia solution was added to dissolve the NPs.

Subsequently, ~5 mL of 2% HNO_3 solution was added. This solution was ready for the ICP-AES analysis.

2.4.6. Magnetic Measurements

Magnetic properties of NPs were evaluated by a vibrating sample magnetometry (VSM, LakeShore 7404) in our group. Several mg of NP dry powder was transferred into a gelatin capsule (0.3 mL, Electron Microscopy Science) and placed inside a uniform magnetic field to measure its hysteresis loop. Alternatively, the NPs can be deposited onto small Si substrates for this measurement. The VSM can only provide a magnetic field of 1.5 T. For very strong ferromagnetic NPs such as fct-FePt NPs, this field is not strong enough to fully magnetize them. Thus a stronger field is necessary. In this case, a Quantum Design Superconducting Quantum Interface Device (SQUID) with a field up to 7 T from Prof. Xiao's group at Physics Department was used.

2.4.7. Electrochemical Measurements

The catalytic properties of NPs studied in this thesis were evaluated using an Autolab 302 Potentiostat station, which uses glassy carbon rotating disk (5 mm in diameter) as a working electrode, Ag/AgCl (4 M KCl) as a reference electrode, and platinum wire as a counter electrode. Typically, NPs were first deposited on Ketjen carbon (C) support at the desired mass ratio. Then the C-NPs was dispersed in the mixture of water, isopropanol and Nafion (v/v/v 4:1:0.05) through sonication to form a homogeneous catalyst ink. The catalyst ink was cast on the rotating disk and dried under ambient condition for the further catalytic study. Different from the NPs deposited on C, the monolayer catalyst of

Co NPs in **Chapter 5** was directed loaded onto a homemade glassy carbon plate electrode for the catalytic measurement.

REFERENCES

[1]   B. L. Cushing, V. L. Kolesnichenko, C. J. O'Connor, *Chem. Rev.* **2004**, *104*, 3893-3946.

[2]   S. G. Kwon, T. Hyeon, *Acc. Chem. Res.* **2008**, *41*, 1696-1709.

[3]   Y. W. Jun, J. S. Choi, J. Cheon, *Angew. Chem. Int. Ed.* **2006**, *45*, 3414-3439.

[4]   J. Park, J. Joo, S. G. Kwon, Y. Jang, T. Hyeon, *Angew. Chem. Int. Ed.* **2007**, *46*, 4630-4660.

[5]   D. V. Talapin, J.-S. Lee, M. V. Kovalenko, E. V. Shevchenko, *Chem. Rev.* **2010**, *110*, 389-458.

[6]   V. K. Lamer, R. H. Dinegar, *J. Am. Chem. Soc.* **1950**, *72*, 4847-4854.

[7]   C. B. Murray, C. R. Kagan, M. G. Bawendi, *Annu. Rev. Mater. Sci.* **2000**, *30*, 545-610.

[8]   C. B. Murray, D. J. Norris, M. G. Bawendi, *J. Am. Chem. Soc.* **1993**, *115*, 8706-8715.

[9]   S. H. Sun, H. Zeng, *J. Am. Chem. Soc.* **2002**, *124*, 8204-8205.

[10]   J. Park, K. J. An, Y. S. Hwang, J. G. Park, H. J. Noh, J. Y. Kim, J. H. Park, N. M. Hwang, T. Hyeon, *Nat. Mater.* **2004**, *3*, 891-895.

[11]   S. H. Sun, H. Zeng, D. B. Robinson, S. Raoux, P. M. Rice, S. X. Wang, G. X. Li, *J. Am. Chem. Soc.* **2004**, *126*, 273-279.

[12]   S. Peng, Y. M. Lee, C. Wang, H. F. Yin, S. Dai, S. H. Sun, *Nano Res.* **2008**, *1*, 229-234.

[13]   V. F. Puntes, K. M. Krishnan, A. P. Alivisatos, *Science* **2001**, *291*, 2115-2117.

[14]   C. Wang, S. Peng, L. M. Lacroix, S. H. Sun, *Nano Res.* **2009**, *2*, 380-385.

[15]   C. Wang, S. Peng, R. Chan, S. H. Sun, *Small* **2009**, *5*, 567-570.

[16]   H. Y. Zhu, A. Sigdel, S. Zhang, D. Su, Z. Xi, Q. Li, S. H. Sun, *Angew. Chem. Int. Ed.* **2014**, *53*, 12508-12512.

[17]   S. H. Sun, C. B. Murray, D. Weller, L. Folks, A. Moser, *Science* **2000**, *287*, 1989-1992.

[18]   M. Chen, J. Kim, J. P. Liu, H. Y. Fan, S. H. Sun, *J. Am. Chem. Soc.* **2006**, *128*, 7132-7133.

[19]   M. Chen, J. P. Liu, S. H. Sun, *J. Am. Chem. Soc.* **2004**, *126*, 8394-8395.

[20]   V. Santhanam, J. Liu, R. Agarwal, R. P. Andres, *Langmuir* **2003**, *19*, 7881-7887.

[21]   T. Wen, S. A. Majetich, *ACS Nano* **2011**, *5*, 8868-8876.

[22]   T. P. Bigioni, X. M. Lin, T. T. Nguyen, E. I. Corwin, T. A. Witten, H. M. Jaeger, *Nat. Mater.* **2006**, *5*, 265-270.

[23]   E. V. Shevchenko, D. V. Talapin, S. O'Brien, C. B. Murray, *J. Am. Chem. Soc.* **2005**, *127*, 8741-8747.

[24]   E. V. Shevchenko, D. V. Talapin, N. A. Kotov, S. O'Brien, C. B. Murray, *Nature* **2006**, *439*, 55-59.

[25]   A. G. Dong, J. Chen, P. M. Vora, J. M. Kikkawa, C. B. Murray, *Nature* **2010**, *466*, 474-477.

[26]   A. Dong, J. Chen, X. Ye, J. M. Kikkawa, C. B. Murray, *J. Am. Chem. Soc.* **2011**, *13*, 13296–13299.

[27]   X. C. Ye, J. Chen, C. B. Murray, *J. Am. Chem. Soc.* **2011**, *133*, 2613-2620.

[28]   R. P. Andres, J. D. Bielefeld, J. I. Henderson, D. B. Janes, V. R. Kolagunta, C. P. Kubiak, W. J. Mahoney, R. G. Osifchin, *Science* **1996**, *273*, 1690-1693.

[29]   J. Lee, S. Lee, G. L. Li, M. A. Petruska, D. C. Paine, S. H. Sun, *J. Am. Chem. Soc.*
        2012, *134*, 13410-13414.

[30]   S. K. Hau, H. L. Yip, N. S. Baek, J. Y. Zou, K. O'Malley, A. K. Y. Jen, *Appl.*
        Phys. Lett. **2008**, *92*.

[31]   L. Wu, P. O. Jubert, D. Berman, W. Imaino, A. Nelson, H. Zhu, S. Zhang, S. Sun,
        Nano Lett. **2014**, 14, 3395-3399.

Chapter 3. Monolayer Assembly of Ferrimagnetic $Co_{0.6}Fe_{2.4}O_4$ Nanocubes for Magnetic Recording

3.1. Introduction

The need for long-term and cost-effective digital archives requires state-of-the-art magnetic tape products with ever increased areal storage density.[1-4] To support such a high recording density, magnets used for tape recording must be made in nanometer-size regime and assembled with both their packing density maximized and their magnetization direction oriented. Conventional nanomagnets developed as magnetic tape media have been based on ferrimagnetic (FIM) iron oxides in needle-like shapes due to their acceptable shape-induced anisotropy/coercivity, medium high magnetization, high Curie temperature, and more importantly, their excellent chemical stability and corrosion resistance. Once stabilized with oxide coating, rod-shaped FeCo alloy particles have been used in tape media products, enabling recording densities up to 2 Gb/in^2. Recently, the demand for even higher recording density requires the nanomagnets to be smaller and smaller and shape anisotropy cannot be used to support such a dimension reduction.

Ferrite magnets with large magnetocrystalline anisotropy, such as cobalt ferrite (CoFe$_2$O$_4$ or CoO·Fe$_2$O$_3$)[5] and hexagonal barium hexaferrite (BaFe, BaO·6Fe$_2$O$_3$ or BaFe$_{12}$O$_{19}$),[6] have been considered as alternative media materials. For example, doped BaFe$_{12}$O$_{19}$, which are now used in commercial tape drives, have led to a 29.5 Gb/in^2 recording demonstration.[7] Magnetic studies have shown that magnetocrytalline anisotropy constant (K) of the non-stoichimetric Co-substituted magnetite Co$_x$Fe$_{3-x}$O$_4$ and hexagonal BaFe can be as high as 5×10^5 J/m^3,[8,9] which are close to those of the common hard magnetic FePt, SmCo and NdFeB magnets at $10^6 - 10^7$ J/m^3.[10,11] These suggest that Co$_x$Fe$_{3-x}$O$_4$ or BaFe, once prepared in a proper nanometer size and shape, can maintain

large magnetic coercivity, providing a more cost-effective system than other noble metal (FePt) and rare-earth metal (SmCo and NdFeB) magnets for magnetic tape applications.

In this chapter we report a new approach to FIM Co-ferrite nanocubes (NCs) and monolayer assemblies and demonstrate their capability for magnetic recording. Previously we developed a high temperature solution phase synthesis of monodisperse $CoFe_2O_4$ nanoparticles (NPs) via thermal decomposition of $Fe(acac)_3$ and $Co(acac)_2$ (acac = acetylacetonate) in the presence of oleic acid and oleylamine.[12] We extended this synthesis and prepared monodisperse $Co_xFe_{3-x}O_4$ NPs with x tuned by the molar ratio of $Co(acac)_2/Fe(acac)_3$.[13] These FIM NPs were dispersible in hexane and random assemblies had coercivities reaching as high as 3.1 kOe at room temperature. However, the size of these Co-ferrite NPs was around 35 nm, which was too large for high-density recording. We further improved the synthesis by replacing oleylamine with sodium oleate and found that FIM Co-ferrite nanocubes (NCs) were produced with their sizes (10-20 nm) and composition ($Co_{0.6}Fe_{2.4}O_4$) controlled by the $Co(acac)_2/Fe(acac)_3$ ratio. More importantly, these FIM NCs were well dispersed in hexane, allowing for self-assembly. We developed an organic liquid-water phase self-assembly approach and succeeded in depositing monolayer assembly of these FIM NCs on a solid substrate. These monolayer arrays showed FIM at room temperature and could be recorded using a static magnetic tester. The work demonstrates the great potential of Co-ferrite NCs as promising alternative media for tape recording applications.

3.2. Experimental Section

Chemicals and Materials. The following chemicals were used as received. Iron (III) acetylacetonate (99%) was purchased from Strem Chemicals. Sodium oleate (90%) was purchased from Spectrum Chemicals. Cobalt(II) acetylacetonate hydrate, oleic acid (90%) and benzyl ether (98%) were all purchased from Sigma Aldrich.

Synthesis of 20 nm $Co_{0.6}Fe_{2.4}O_4$ NCs: Under a gentle flow of Ar, iron(III) acetylacetonate (1.0 mmol, 350 mg), cobalt(II) acetylacetonate hydrate (0.48 mmol, 140 mg), sodium oleate (1 mmol, 300 mg) and oleic acid (2 mL) were mixed with benzyl ether (10 mL). The mixture was magnetically stirred under a flow of Ar and then heated to 120 ^{o}C for 1 h. Under Ar blanket, the solution was heated up to 290 ^{o}C at a heating rate of 15 ^{o}C/min and kept at this temperature for 1 h. Then the mixture was cooled down to room temperature by removing the heating mantle. Under ambient conditions, 10 mL of hexane and 30 mL of ethanol were added to the mixture to precipitate the product. Centrifugation (8500 rpm for 8 min) was applied to collect the product. The product was redispersed in hexane and precipitated out by addition of ethanol for further purification. Then the final product was dispersed in hexane for further characterizations.

For the synthesis of 15 nm $Co_{0.6}Fe_{2.4}O_4$ NCs, the synthetic procedure was the same except the amounts of metal precursors were decreased to 280 mg (0.8 mmol) of iron(III) acetylacetonate and 134 mg (0.46 mmol) of cobalt(II) acetylacetonate hydrate. By further decreasing the amount of cobalt(II) acetylacetonate hydrate to 122 mg (0.42 mmol), 10 nm $Co_{0.6}Fe_{2.4}O_4$ NCs were synthesized.

Monolayer Assembly of the NCs: Large-area monolayer assemblies of the 20 nm NCs were fabricated using the self-assembly approach at the water-air interface. Briefly, the NCs were diluted and dispersed in the mixture of toluene and hexane (volume ratio of 1:1) with the concentration of 0.5 mg/mL. 120 μL of the dispersion was drop-cast and spread onto the surface of deionized water in a Telfon column (diameter: 3.8 cm), which was then slowly dried at room temperature. After complete evaporation of toluene and hexane, the monolayer assemblies of the NCs floating on the water surface were transferred onto Cu TEM grids or Si substrates for further characterizations.

Characterization: TEM and HRTEM images were obtained on a Philips CM 20 microscope and a JEOL 2010 microscopy with an accelerating voltage of 200 kV, respectively. SEM images were acquired on a LEO 1530 microscope at an accelerating voltage of 10 kV. Elemental analysis was done on a JY2000 Ultrace ICP Atomic Emission Spectrometer equipped with a JY AS 421 autosampler and 2400g/mm holographic grating. X-ray diffraction was performed on a Bruker AXS D8-Advanced diffractometer with Cu Kα radiation (λ=1.5418 Å). Magnetic measurements were carried out using a Lakeshore 7404 high-sensitivity vibrating sample magnetometer (VSM). The magnetic recording performance was obtained using a contact magnetic tester. A Physik Instrumente piezoelectric nanopositioning stage was used to control the sample position during magnetic recording measurements. A hard disk drive (HDD) head with a Giant Magneto-Resistive (GMR) read sensor that is 115 nm wide and a longitudinal write element that is 160 nm wide was used to write and read magnetic signals on the sample.

3.3. Results and Discussion

3.3.1. Synthesis of Cobalt Ferrite Nanocubes

The $Co_xFe_{3-x}O_4$ NCs were synthesized by the thermal decomposition of $Fe(acac)_3$ and $Co(acac)_2$ in benzyl ether at 290 ^{o}C for 1 h. Oleic acid and sodium oleate were used as surfactants to direct the anisotropic growth. The as-synthesized NCs were characterized by transmission electron microscopy (TEM). **Figure 3-1A** shows the typical TEM image of the as synthesized NPs deposited on an amorphous carbon-coated Cu grid. These NCs have an average edge size of 10 $\pm$ 0.7 nm. By increasing the amount of $Fe(acac)_3$ and $Co(acac)_2$ while keeping other parameters unchanged, larger NCs were synthesized. **Figure 3-1B** and 3-**1C** show the TEM images of larger NCs with the size of 15 $\pm$ 0.6 nm and 20 $\pm$ 1 nm, respectively. The Co compositions in those NCs were determined by using inductively coupled plasma−atomic emission spectroscopy (ICP-AES). All of the three kinds of NCs showed the same composition of $Co_{0.6}Fe_{2.4}O_4$, which was in the right range for optimized magnetic coercivity.[8] The 20 nm NCs were further characterized by high resolution TEM (HR-TEM) (**Figure 3-1D**), which shows lattice fringes with the inter-fringe distance in a single NC at 2.9 Å, close to the lattice spacing of (220) planes at 2.96 Å in the reverse spinel $CoFe_2O_4$. Also the diagonal direction of (220) planes further confirmed the cubic shape of the nanoparticle. Some crystal defects were found in the HRTEM image as marked by dashed ellipses. These defects were probably caused by O vacancies formed in the inert reaction atmosphere. **Figure 3-1E** is the X-ray diffraction (XRD) pattern of the 20 nm NC powder dried from the hexane dispersion. The diffraction pattern corresponds well with the inverse spinel crystal

structure of $CoFe_2O_4$, which shows clear (220), (311), (222), (400), (422), (511) and (440) diffraction peaks.
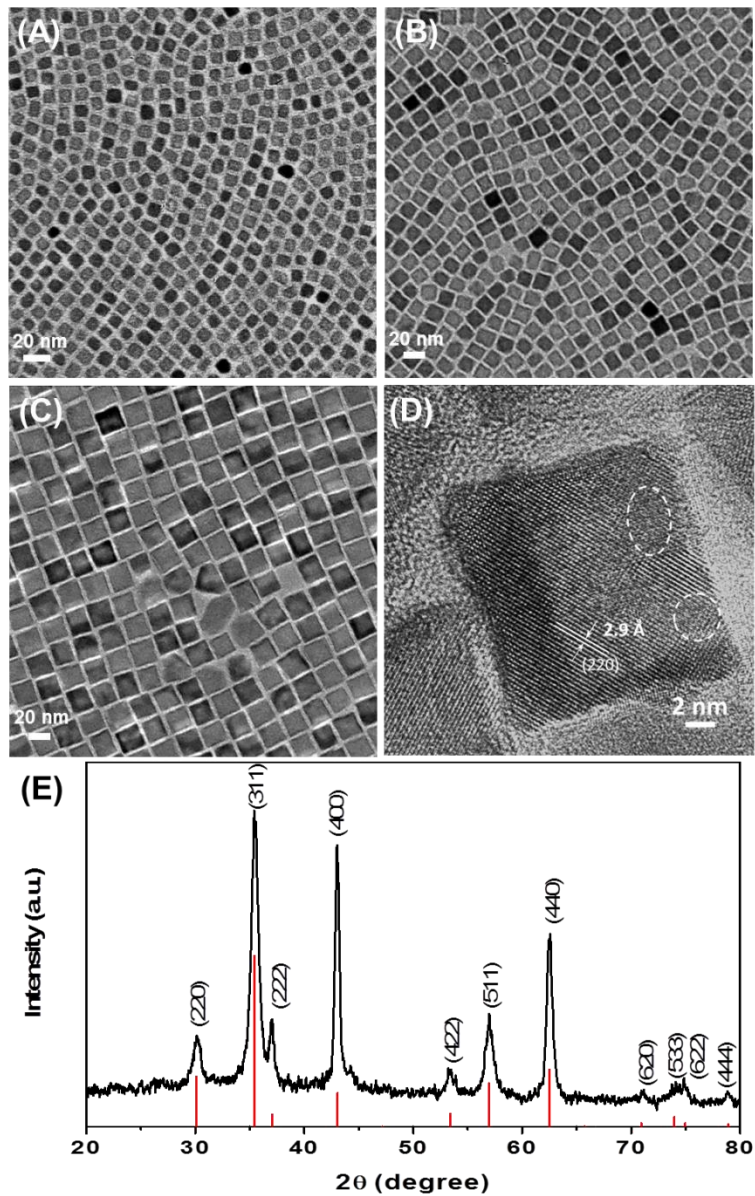
Figure 3-1. TEM images of the as-synthesized (A) 10 nm, (B) 15 nm, and (C) 20 nm $Co_{0.6}Fe_{2.4}O_4$ NCs; (D) HR-TEM image of a single 20 nm NC; (E) XRD pattern of the powder dried from hexane dispersion of 20 nm NCs.

To better understand the role of the surfactants in the NC growth, we did some control experiments. For the synthesis of 20 nm $Co_{0.6}Fe_{2.4}O_4$ NCs showing in **Figure 3-**

1C, 350 mg Fe(acac)$_3$ reacted with 140 mg Co(acac)$_2$ in the presence of 300 mg sodium oleate and 2 mL oleic acid. Without sodium oleate, polyhedral NPs were synthesized, as shown in **Figure 3-2A**. This indicates that the formation of NCs was initiated by the preferred binding of sodium oleate to the {100} planes, which promoted the faster growth along <111> directions. Oleic acid in the synthesis not only acts as the surfactant but also as the growth rate controller. For example, larger NCs (60 nm) were synthesized by decreasing the amount of oleic acid to 1.5 mL while maintaining other reaction conditions (**Figure 3-2B**).
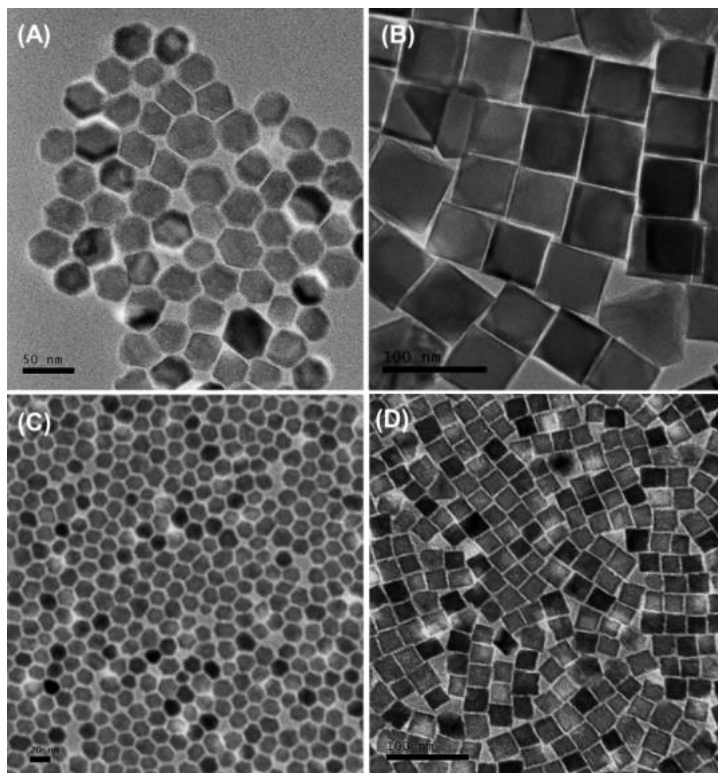
Figure 3-2. TEM images of Co-ferrite NPs (A) polyhedral NPs synthesized without using sodium oleate, (B) 60 nm cubic NPs, (C) 15 nm polyhedral NPs and (D) 25 nm cubic NPs.

It is worth emphasizing that enough precursors are also critical for the formation of cubic NPs. By just decreasing the amount of cobalt precursors from 140 mg to 120 mg,

smaller (15 nm) polyhedral NPs rather than NCs were obtained, as shown in **Figure 3-2C**. It seems that due to the lack of enough monomers, the growth along <111> direction was not complete which resulted in truncated cubic NPs. ICP analysis showed that the composition of the NPs was $Co_{0.4}Fe_{2.6}O_4$, which had lower Co content compared to the 20 nm NCs. However, if the amount of cobalt precursors was increased to 160 mg, the {111} were fully developed and NCs were formed. And more precursors resulted in larger NCs (25 nm) as confirmed by TEM image in **Figure 3-2D**. The composition was determined to be $Co_{0.7}Fe_{2.3}O_4$, which was more Co-rich than the 20 nm NCs. Our synthesis indicates that both surfactants and precursors need to be controlled in a proper amount to achieve the anisotropic growth of the Co-ferrite NPs into cubic shape and controlled compositions.

3.3.2. Magnetic Properties of $Co_{0.6}Fe_{2.4}O_4$ Nanocubes

Magnetic properties of the $Co_{0.6}Fe_{2.4}O_4$ NCs were characterized by a vibrating sample magnetometer (VSM) with fields up to 14.5 kOe at room temperature. The hysteresis loops of the as-synthesized NCs are shown in **Figure 3-3A**. These NCs exhibited clear size-dependent magnetic properties. For the 10 nm NCs, the coercivity was just 15 Oe. As the size increased to 15 nm, the coercivity increased to 170 Oe correspondingly. Further increasing the size to 20 nm resulted in the enhancement of coercivity to 810 Oe. Considering the defects present in each NP (**Figure 3-1D**) may result in low magnetic anisotropy of the ferrite NPs, we annealed the ferrite NPs in O_2 at 300 ^{o}C for 1 h. **Figure 3-3B** shows the hysteresis loops of the NCs after the annealing. The coercivity of the 10 nm, 15 nm and 20 nm NCs were significantly increased to 550

Oe, 1200 Oe and 1930 Oe, respectively. Besides, the saturation moment (Ms) of the NCs also increased after the annealing treatment. For instance, the Ms of 20 nm NCs enhanced to 78 emu/g, which was much higher than that of as-synthesized ones (55 emu/g).
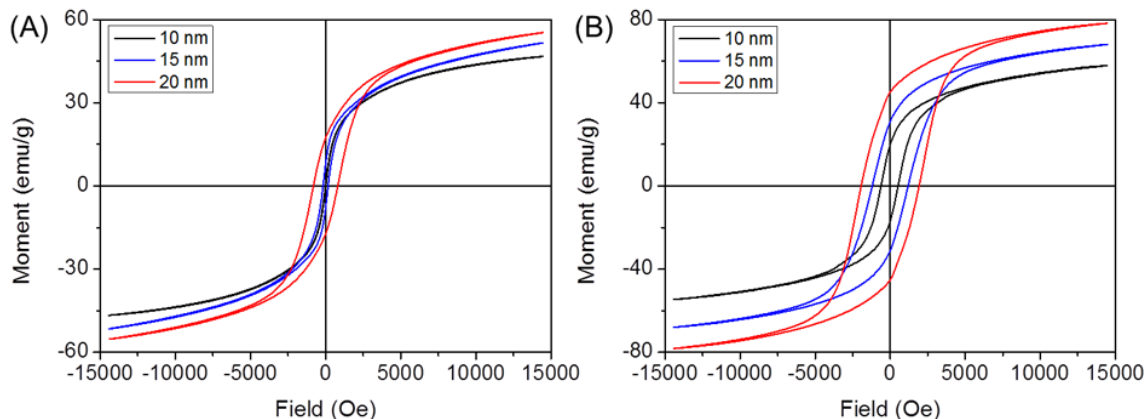
Figure 3-3. Hysteresis loops of (A) the as-synthesized NCs without annealing and (B) the annealed NCs (annealing in oxygen at 300 ^{o}C for 1h).
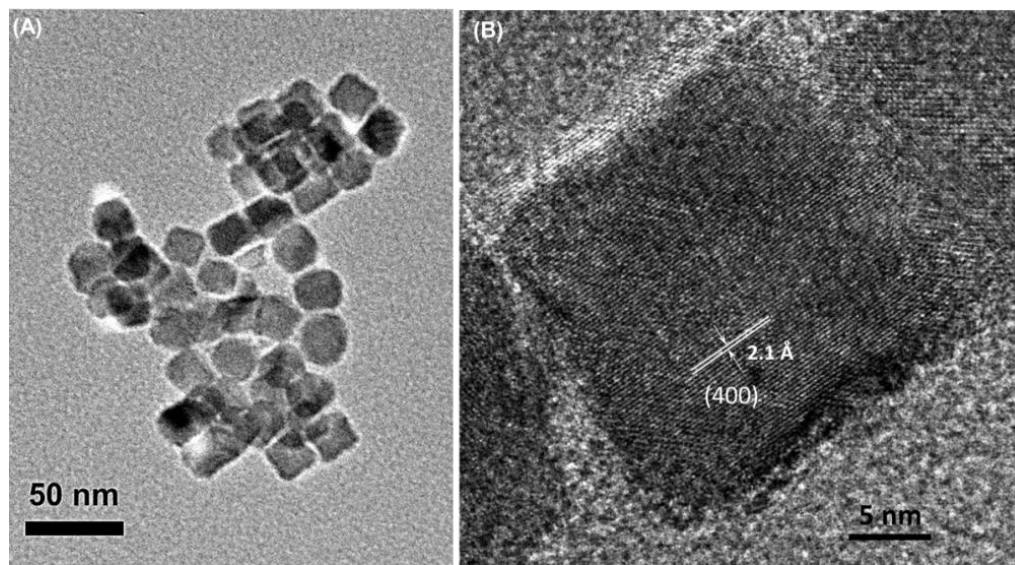
Figure 3-4. (A) TEM image of the 20 nm NCs and (B) HR-TEM image of a single 20 nm NC after annealing in oxygen at 300 ^{o}C for 1 h.

TEM image of the 20 nm NCs after annealing shows no aggregation/sintering (**Figure 3-4A**). The HR-TEM image of a single NC after annealing is shown in **Figure 3-**

4B, which clearly exhibits perfect lattice fringes of (400) planes in the single crystalline NC. Control experiment of annealing the NCs in inert Ar gas at 300 ^{o}C for 1 h shows that there is no obvious magnetic property change between the annealed and the as-synthesized (**Figure 3-5**). These controlled annealing and its effect on magnetic properties confirm that the defects observed in the as-synthesized ferrite NC (**Figure 3-1D**) indeed lead to decreased coercivity and annealing under O_2 is necessary to remove these defects and to increase magnetic anisotropy.
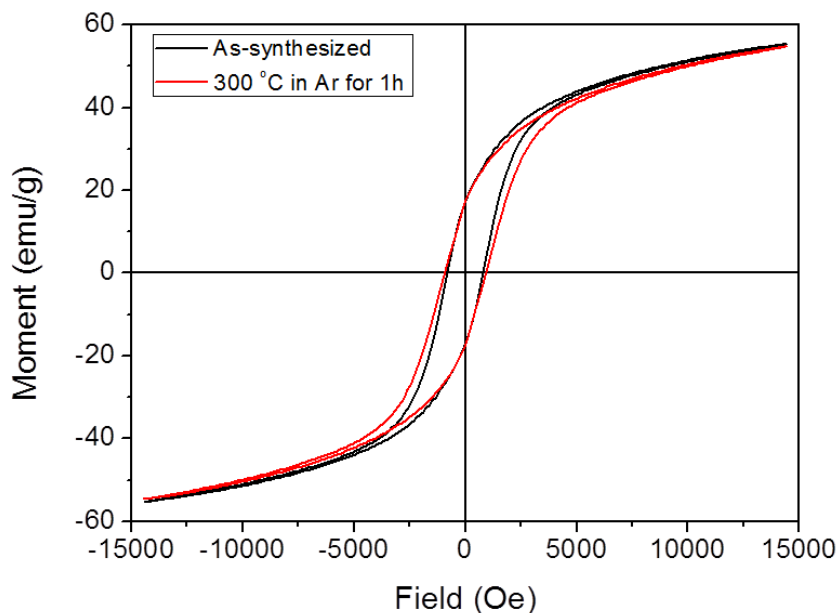
Figure 3-5. Hysteresis loops of the 20 nm NCs before and after annealing in Ar gas at 300 ^{o}C for 1 h.

3.3.3. Self-Assembly of Co$_{0.6}$Fe$_{2.4}$O$_4$ Nanocubes

To test the potential of these FIM NCs for data storage applications, they must first be assembled in uniform arrays with high packing density. We utilize the self-assembly technique at the liquid-air interface to fabricate ordered monolayer NC arrays for

magnetic recording demonstration.[14,15] We improved the liquid-air interfacial assembly and developed a facile approach to assemble NCs at organic solvent and water interface. To make the monolayer assembly, 120 μL of the NCs dispersion in the mixture of toluene and hexane (volume ratio 1:1) with the concentration of 0.5 mg/mL was drop-cast on the water surface in a Teflon column (diameter, 3.8 cm) and then dried at room temperature. By using the mixture of toluene and hexane, the evaporating rate was slowed which favored the NC face-to-face interaction for the assembly formation. After complete evaporation of the toluene and hexane, monolayer film formed on the water surface was transferred onto Cu TEM grids or Si substrates for further characterizations. **Figure 3-6A** shows the TEM image of the self-assembled monolayer array of the 20 nm $Co_{0.6}Fe_{2.4}O_4$ NCs. Scanning electron microscopy (SEM) image of the self-assembled NCs is shown in **Figure 3-6B**, which further confirms the formation of large-area densely packed monolayer.
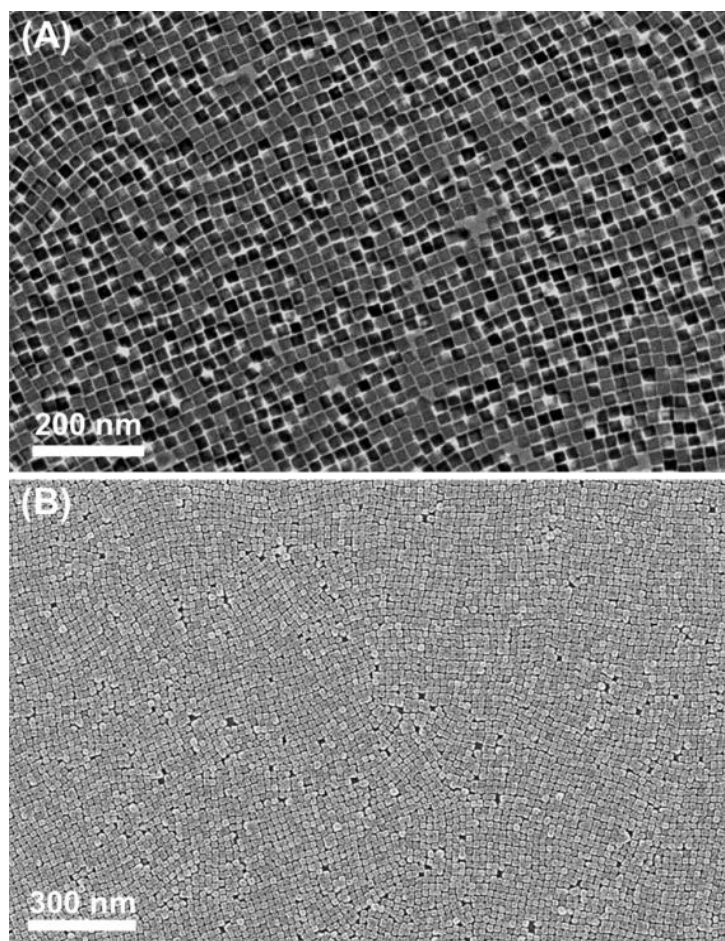
Figure 3-6. (A) TEM and (B) SEM image of the self-assembled monolayer of the 20 nm NCs

The crystal orientation of each NC in the self-assembly was further characterized by X-ray diffraction (XRD) (**Figure 3-7**). Different from the randomly oriented powder diffraction pattern of the 20 nm NCs which shows a strong (311) diffraction peak in **Figure 3-1E**, the XRD pattern of the self-assembled monolayer on Si substrate exhibits only one (400) diffraction peak. This (400)-only diffraction further indicates that NCs in the monolayer assembly have preferred orientation along <100> direction.
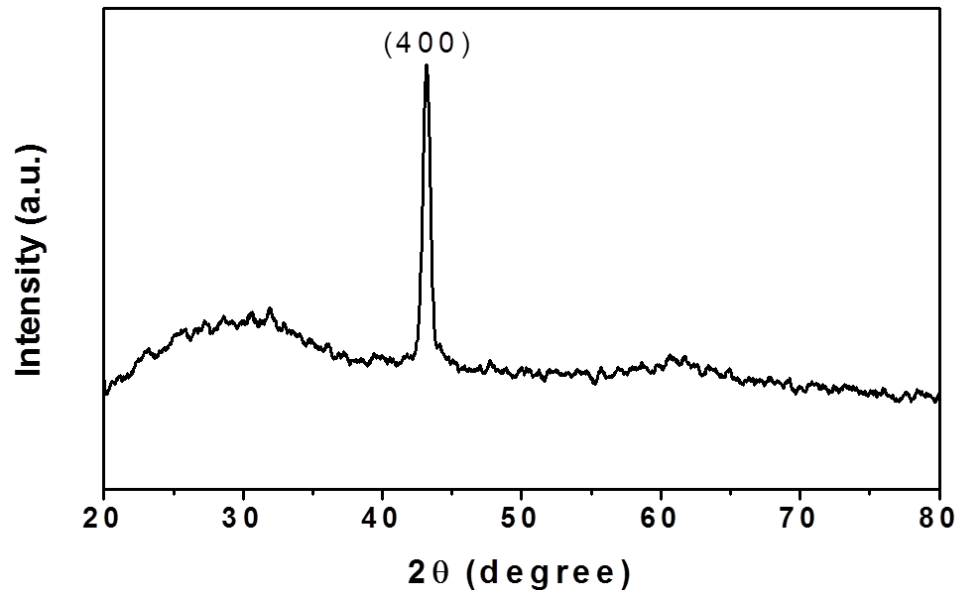
Figure 3-7. XRD pattern of the monolayer assembly deposited on a Si substrate.

It is worth mentioning that this water-air interfacial self-assembly process is very versatile to make monolayer assembly of the NCs with different sizes. Similar large-area monolayer assembly film of 15 nm and 10 nm NCs were also obtained, as demonstrated by the SEM and TEM images in **Figure 3-8**. Moreover, by tuning the amount of initial dispersion of the NCs, the thickness of the film can be changed. For example, increasing the volume from 120 μL to 160 μL resulted in the formation of bilayer assembly, as shown in **Figure 3-9**.
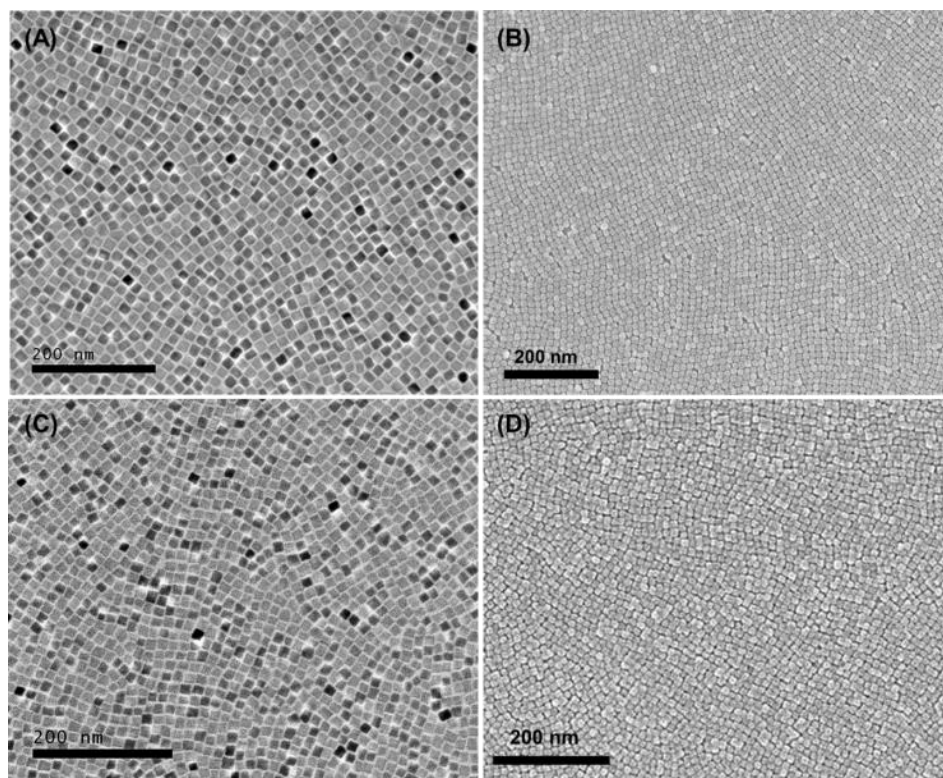
Figure 3-8. (A)TEM image and (B) SEM image of the self-assembled monolayer of 15 nm NCs; (C) TEM image and (D) SEM image of the self-assembled monolayer of 10 nm NCs.
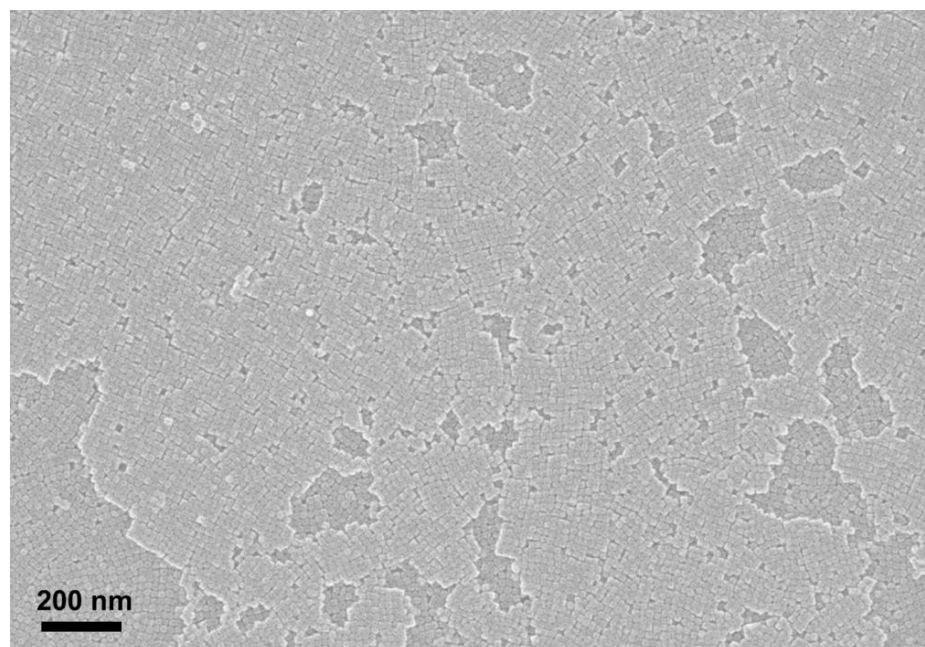
Figure 3-9. SEM image of the bilayer assembly of 20 nm NCs.

3.3.4. Magnetic Recording of 20 nm $Co_{0.6}Fe_{2.4}O_4$ Nanocubes

We chose the monolayer assembly of the 20 nm $Co_{0.6}Fe_{2.4}O_4$ NCs deposited on a Si substrate to demonstrate their capability in recording magnetization transitions. To ensure the assembly was magnetically and mechanically robust for the recording demonstration, we first annealed the monolayer assembly at 300 ^{o}C in O_2 for 1 h. **Figure 3-10** shows the SEM image of the annealed monolayer assembly. After this post treatment the monolayer array was well-maintained without any aggregation or sintering. Magnetic properties of the monolayer assembly were measured using VSM at room temperature. Due to the very weak signal of the monolayer, hysteresis loops were obtained roughly by subtracting the background signal from Si. As shown in **Figure 3-11**, O_2 annealing indeed increased the coercivity of the NCs in monolayer assembly. The monolayer assembly was then coated with a 15 nm SiN film deposited *via* sputtering step for magnetic recording test.
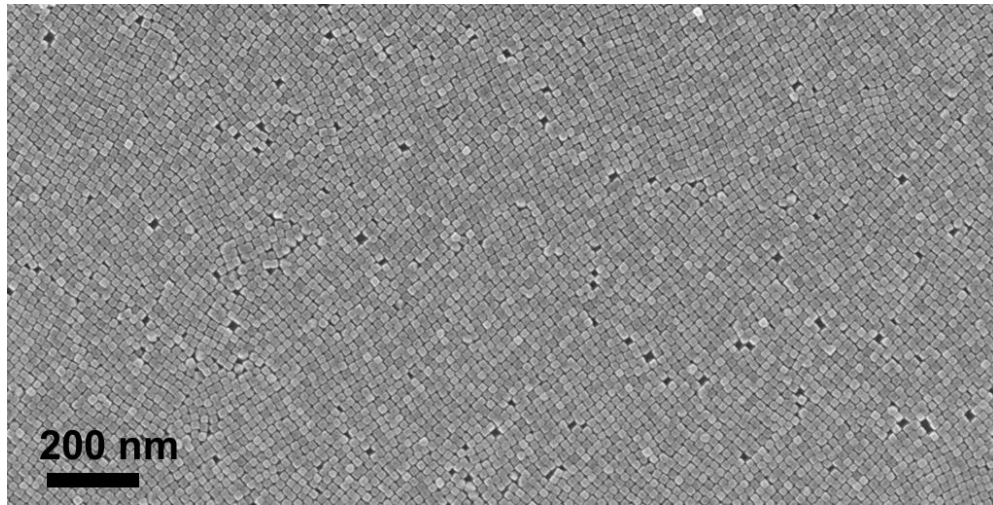
Figure 3-10. SEM image of the monolayer film after annealing at 300 ^{o}C for 1 h in oxygen.
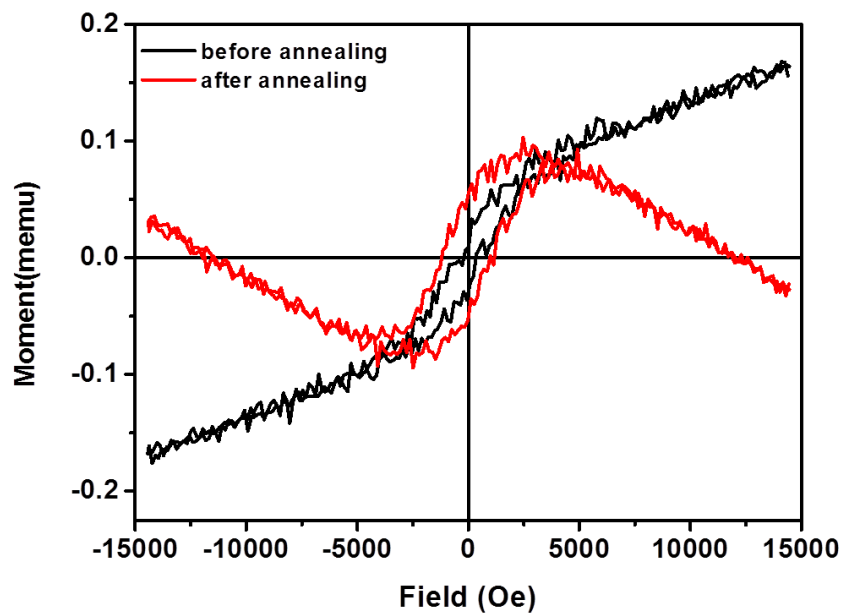
Figure 3-11. Out-of-plane hysteresis loops of the monolayer assembly on a Si before and after annealing in O_2 at 300 ^oC for 1h.
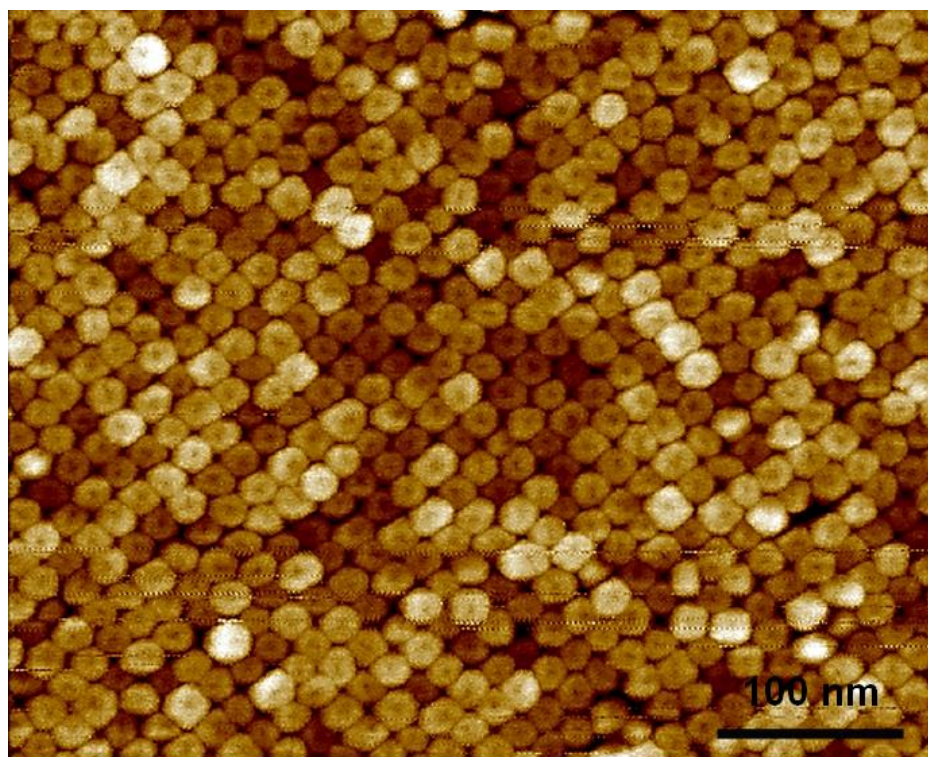
Figure 3-12. AFM image of the monolayer assembly on Si after O_2 annealing.
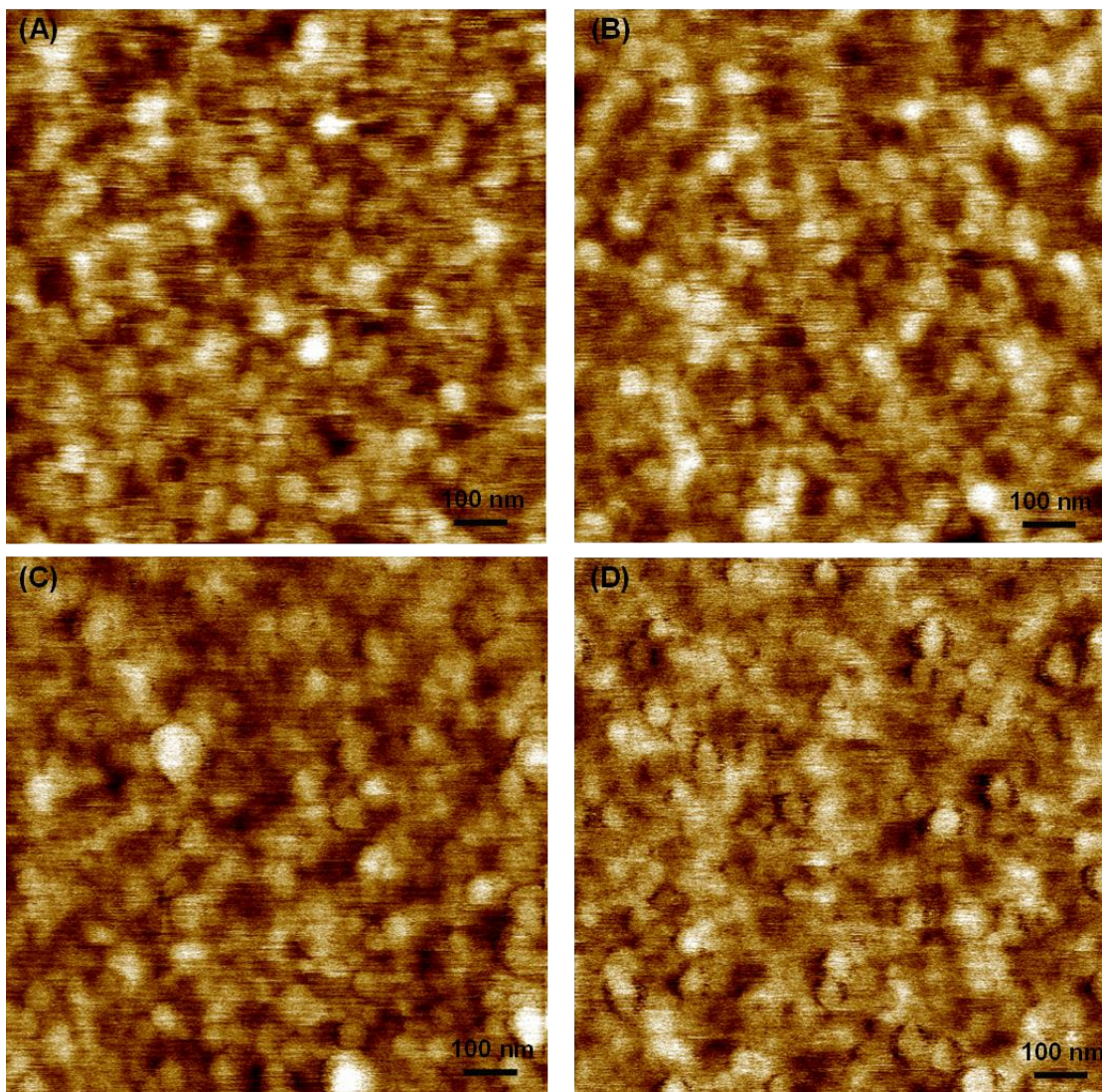
Figure 3-13. MFM images of the monolayer assembly subject to an in-plane field of (A) 0 Oe. (B) 1000 Oe. (C) 2000 Oe. (D) -2000 Oe.

To better understand the magnetic domain structures in the monolayer assembly, magnetic force microscopy (MFM) images were collected using a Dimension 3100 SPM system. **Figure 3-12** is the atomic force microscopy (AFM) image of the monolayer assembly on Si after O_2 annealing at 300 ^{o}C for 1h, which confirms a uniform surface constructed by the closely packed 20 nm NCs as demonstrated by those SEM and TEM images. MFM images of the monolayer were collected by applying an in-plane field from

-2000 to 2000 Oe. **Figure 3-13** presents the MFM images of the monolayer film subject to different in-plane (parallel to the plane of the film) fields. The MFM image without external field (**Figure 3-13A**) shows areas with different contrast, indicating the different magnetic domain directions (up direction, down direction and intermediate directions). When the field increases to 1000 Oe, due to the not enough field strength, the magnetic domains still exist different directions in the monolayer film, as indicated by the different contrast in the MFM image (**Figure 3-13B**). However, as the field continues to increase to 2000 Oe, it is strong enough to make the domains flip and align in the direction of the external field. In this case the MFM image in **Figure 3-13C** displays mainly the dark color. In the opposite direction of the external field, the MFM image (**Figure 3-13D**) is dominate by the white-colored area, indicating the reverse of the magnetic domains in the monolayer film. The dynamics of the magnetic domains in the monolayer assembly demonstrates their potential applications as the magnetic recording media for data storage applications.

The magnetic recording characteristics of the monolayer assembly were measured using a contact magnetic tester. The monolayer array was first written by the write head with different linear densities of the writing signal and then the recorded information was sensed by read head in the form of voltage. **Figure 3-14** is the magnetic field image of the readback amplitude at linear densities ranging from 254 to 31 kfci (thousand flux change per inch). The tracks are written along the vertical direction. The leftmost track corresponds to the highest linear density of 254 kfci. The linear density in the subsequent tracks towards the right is decreased with the rightmost track corresponding to the lowest

linear density of 31 kfci. The signal amplitude increased while decreasing the linear densities of the writing signal.
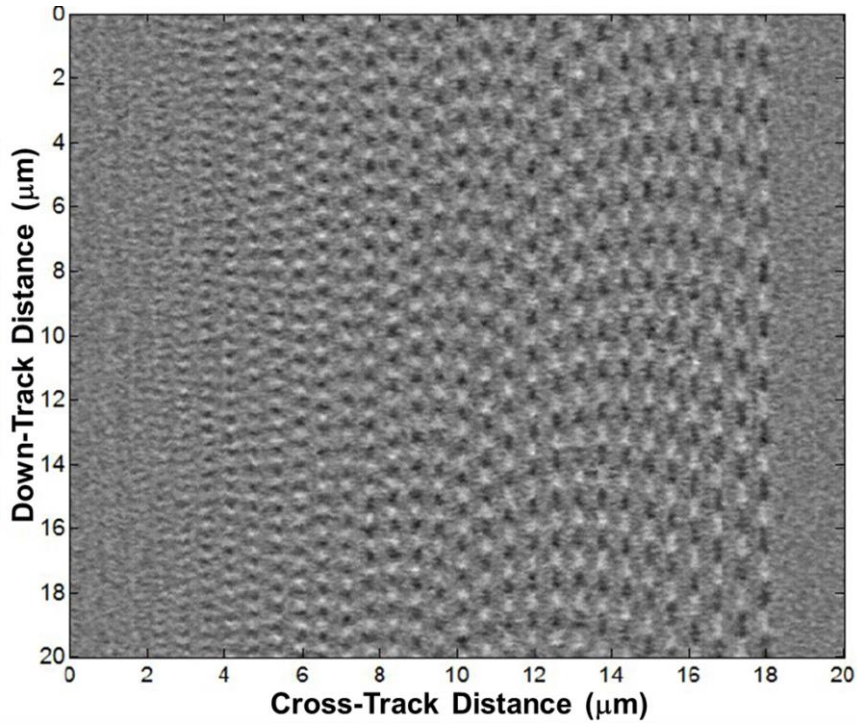
Figure 3-14. Magnetic field image of the readback amplitude at linear densities ranging from 254 to 31 kfci.

At the linear bit density of 125 kfci, the signal exhibited sufficiently strong signal to enable the study of the dependence of signal amplitude on write current, which is shown in **3-15A**. The signal amplitude enhanced while increasing the write current from 100 mA but saturated at around 250 mA. To further assess the write/read performance of the monolayer assembly, the signal-to-noise ratio (SNR) of the readback signal was tested at different linear bit density, as shown in **Figure 3-15B**. It can be found that the SNR value was around 10 dB at linear densities below 200 kfci, indicating that the signal could be easily resolved above the noise. Thus these write/read experiments clearly demonstrate

that the monolayer assembly of the ferrimagnetic $Co_{0.6}Fe_{2.4}O_4$ NCs can indeed be used as a magnetic recording medium.
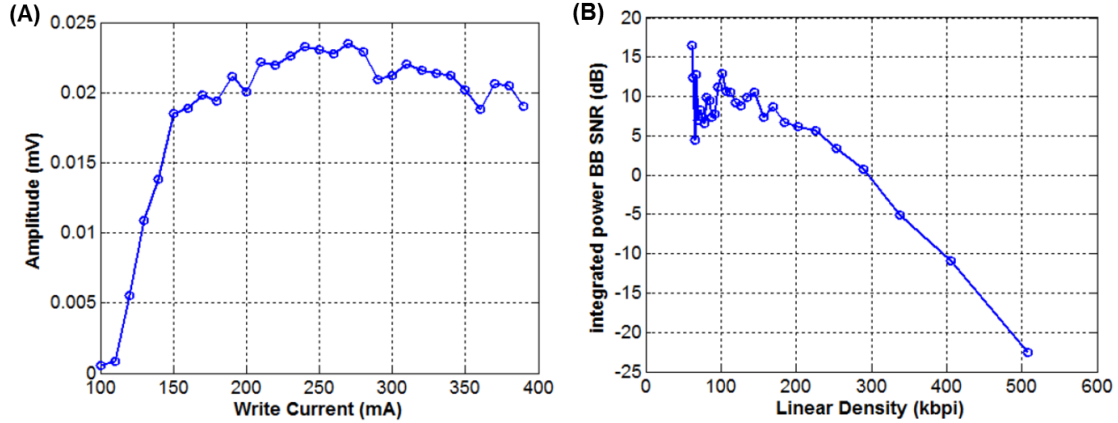
Figure 3-15. (A) Dependence of signal amplitude on the write current. (B) The dependence of SNR (signal-to-noise ratio) on the write signal at different linear densities.

3.4. Conclusion

In conclusion, we have reported an improved and facile approach to ferrimagnetic ferrite NCs of $Co_xFe_{3-x}O_4$. The NCs are synthesized by high temperature decomposition of $Fe(acac)_3$ and $Co(acac)_2$ and the NC shapes are controlled by oleic acid and sodium oleate. The synthesis allows easy control of NC sizes (from 10 nm to 60 nm) and Co/Fe compositions, and $Co_{0.6}Fe_{2.4}O_4$ NCs are found to be optimal to show ferrimagnetism with the 20 nm NCs having a room temperature $H_c = 1930$ Oe. The well-dispersed ferrimagnetic NCs can be assembled into monolayer array at the water-air interface and the monolayer array in centimeter square is readily transferred onto a solid substrate. The NCs in the monolayer array are densely packed and (100) textured. Once annealed in air and coated with a thin (15 nm) SiN film, the NC arrays become robust and can be used to record magnetic patterns. Our magnetic writing experiments show that the 20 nm NC

monolayer array can be recorded at linear densities ranging from 254 to 31 kfci (thousand flux change per inch), indicating the potential of self-assembled monolayer array as magnetic recording media. Our synthesis and self-assembly methods are not limited to ferrite NCs, but can be extended to other functional nanoparticles as well, providing a unique approach to monolayer nanoparticle array for important technological applications.

REFERENCES

[1]   Dee, R. H. *MRS Bull.* **2006**, 31, 404-408.

[2]   Argumedo, A. J.; Berman, D.; Biskeborn, R. G.; Cherubini, G.; Cideciyan, R. D.; Eleftheriou, E.; Haberle, W.; Hellman, D. J.; Hutchins, R.; Imaino, W.; Jelitto, J.; Judd, K.; Jubert, P. O.; Lantz, M. A.; McClelland, G. M.; Mittelholzer, T.; Narayan, C.; Olcer, S.; Seger, P. J. *IBM J. Res. Dev.* **2008**, 52, 513-527.

[3]   Holzner, F.; Paul, P.; Drechsler, U.; Despont, M.; Knoll, A. W.; Duerig, U. *Appl. Phys. Lett.* **2011**, 99, 023110.

[4]   Fontana, R. E.; Hetzler, S. R.; Decad, G. *IEEE Trans. Magn.* **2012**, 48, 1692-1696.

[5]   Dai, Q.; Berman, D.; Virwani, K.; Frommer, J.; Jubert, P. O.; Lam, M.; Topuria, T.; Imaino, W.; Nelson, A. *Nano Lett.* **2010**, 10, 3216-3221.

[6]   Kolev, S.; Lisjak, D.; Drofenik, M. *J. Exp. Nanosci*. **2011**, 6, 362-373.

[7]   Cherubini, G.; Cideciyan, R. D.; Dellmann, L.; Eleftheriou, E.; Haeberle, W.; Jelitto, J.; Kartik, V.; Lantz, M. A.; Olcer, S.; Pantazi, A.; Rothuizen, H. E.; Berman, D.; Imaino, W.; Jubert, P. O.; McClelland, G.; Koeppe, P. V.; Tsuruta, K.; Harasawa, T.; Murata, Y.; Musha, A.; Noguchi, H.; Ohtsu, H.; Shimizu, O.; Suzuki, R. *IEEE Trans. Magn.* **2011**, 47, 137-147.

[8]   Nlebedim, I. C.; Snyder, J. E.; Moses, A. J.; Jiles, D. C.; *IEEE Trans. Magn.* **2012**, 48, 3084-3087

[9]   Golubenko, Z. V.; Ol'khovik, L. P.; Popkov, Y. A.; Sizova, Z. I.; Kamzin, A. S. Phys. Solid State **1998**, 40, 1718-1720.

[10]   Weller, D.; Moser, A. *IEEE Trans. Magn.* **1999**, 35, 4423-4439.

[11]   Weller, D.; Doerner, M. F. *Annu. Rev. Mater. Sci.* **2000**, 30, 611-644.

[12]   Sun, S. H.; Zeng, H.; Robinson, D. B.; Raoux, S.; Rice, P. M.; Wang, S. X.; Li, G. X. *J. Am. Chem. Soc.* **2004**, 126, 273-279.

[13]   Yu, Y. S.; Mendoza-Garcia, A.; Ning, B.; Sun, S. H. *Adv. Mater.* **2013**, 25, 3090-3094.

[14]   Dong, A. G.; Chen, J.; Vora, P. M.; Kikkawa, J. M.; Murray, C. B. *Nature* **2010**, 466, 474-477.

[15]   Wen, T.; Majetich, S. A. *ACS Nano* **2011**, 5, 8868-8876.

Chapter 4. Synthesis and Assembly of Barium-doped Iron Oxide Nanoparticles and Nanomagnets

4.1. Introduction

Magnetic iron oxide nanoparticles (NPs) with controlled size and magnetic properties have attracted tremendous research and development interests due to their great application potentials for future nanomedicine,[1-8] high performance ferrite magnets,[9-11] and high density magnetic tape recording.[11-13] There are two common types of magnetic iron oxides: the cubic structured spinel-type ferrites with a general formula MFe_2O_4 (M = Mn, Fe, Co, Ni, etc) and hexagonal barium ferrite, or BaFe, with a general formula $BaFe_{12}O_{19}$. The spinel ferrites are magnetically isotropic and weakly ferrimagnetic. Their NPs in sub-10 nm are often superparamagnetic at room temperature. In contrast, the hexagonal BaFe support anisotropic spin alignment along the crystallographic c-direction and their magnetocrystalline anisotropy can reach 5×10^5 J/m^3.[14-15] This, plus their chemical stability, has made BaFe a class of well-known materials for permanent magnets.[11] Recently, the hard magnetic BaFe are also prepared in nanostructured plates and tested as a new medium for magnetic tape recording.[16-19] To maximize the magnetic recording density in tape recording media and magnetic energy storage capability in ferrite magnets, uniform BaFe NPs with controlled magnetic properties need to be prepared and assembled in either two dimensional (2D) arrays for magnetic recording or densely-packed 3D stacks for permanent magnets.

BaFe is normally synthesized by solid-state reactions between Ba- and Fe-precursors at temperatures higher than 1000 $^{\circ}$C due to the need to form hexagonal structure from the normal cubic oxide precursors. These include the direct solid reaction between metal hydroxides[20-21] or iron oxide and barium carbonate,[22-24] hydrothermal reaction of metal hydroxides followed by annealing,[25-27] and organic phase preparation of $Fe_3O_4/BaCO_3$

core/shell NPs followed by annealing in O_2.[28] However, these solid state reactions and high temperature annealing often result in incomplete alloy formation between the Ba- and Fe-oxides. The high temperature diffusion between Ba- and Fe-precursors also causes uncontrolled sintering of BaFe, making it extremely difficult to control BaFe sizes and magnetic properties.

To develop a better approach to BaFe NPs and their assemblies, we tested the organic-phase decomposition of both Fe- and Ba-precursors at temperatures above 200°C. We found that Ba-doped iron oxide NPs, denoted as Ba-Fe-O NPs could be easily prepared by thermal decomposition of $Fe(acac)_3$ (acac = acetylacetonate) and $Ba(stearate)_2$ at 320°C in 1-octadecene with oleic acid and oleylamine as surfactants. The as-synthesized Ba-Fe-O NPs were well-dispersed in hexane and could be easily assembled into 2D arrays. Upon thermal annealing, these NPs were converted to hexagonal BaFe NPs, showing much enhanced magnetic properties. Moreover, the synthesis could be generalized to make other doped iron oxide NPs, as demonstrated in the synthesis of strontium-doped iron oxide (Sr-Fe-O) NPs and hexagonal SrFe NPs. Here we highlight this new synthesis and self-assembly of Ba-Fe-O NPs to hexagonal BaFe magnet arrays.

4.2. Experimental Section

Chemicals: Iron(III) acetylacetonate (99%), barium stearate (technical grade) were purchased from Strem Chemicals. Strontium stearate (98.5%) was purchased from VWR. Oleic acid (90%), oleylamine (70%) and 1-octadecene (90%) were all purchased from Sigma-Aldrich. All chemicals were used as received without further purification.

Synthesis of Ba-Fe-O NPs: In a typical synthesis of $Ba_{0.082}$-Fe-O NPs, Ba-stearate (60 mg, 0.085 mmol), $Fe(acac)_3$ (300 mg, 0.85 mmol), oleic acid (1 mL), oleylamine (8 mL) and 1-octadecene (3 mL) were mixed and magnetically stirred at room temperature under a gentle flow of Ar gas for 20 min. Then the mixture was heated up directly to 320 ^{o}C at the heating rate of 10 ^{o}C/min. The reaction was kept at this temperature for 1.5 h. Then the mixture was cooled down to room temperature by removing the heating mantle. The NPs were precipitated by 2-propanol (30 mL) and collected by centrifugation (8500 rpm, 8 min). The product was re-dispersed in hexane and separated again by adding ethanol followed by centrifugation (8500 rpm, 8 min). The final product was dispersed in hexane for further characterization.

Self-assembly of Ba-Fe-O NPs: Monolayer assembly of the $Ba_{0.082}$-Fe-O NPs was prepared using the water-air interfacial self-assembly approach reported previously.[13] Briefly, the NPs were dispersed in the mixture of hexane and toluene (v:v = 1:1) at the concentration of 0.5 mg/mL. 160 μL of the dispersion was drop-cast on the water surface in the Teflon column (diameter: 3.8 cm). Upon complete evaporation of the organic solvent, the formed monolayer assembly floating on the water surface was transferred to TEM Cu grids or Si substrates for further characterization. Multilayer assembly of the NPs was prepared by drop-casting 16 μL of the dispersion on a Si substrate (0.7 cm $\times$ 0.7 cm).

Characterization: Transmission electron microscopy (TEM) and high-resolution TEM (HR-TEM) images were collected using a Philips CM20 and JEOL 2010 both with an accelerating voltage of 200 kV, respectively. Scanning electron microscopy (SEM)

images of the assemblies were acquired on a LEO 1530 microscope at an operating voltage of 10 kV. Energy dispersive X-ray (EDX) spectrum was obtained by Oxford energy-disperse X-ray spectroscopy equipped in the SEM at an operating voltage of 20 kV. X-ray diffraction (XRD) patterns of the samples were collected on a Bruker AXS D8-Advanced diffractometer with Cu Kα radiation (λ = 1.5418 Å). The Ba/Fe composition was determined by elemental analysis using a JY2000 Ultrace ICP Atomic Emission Spectrometer. Magnetic properties were measured on a Lakeshore 7404 high-sensitivity vibrating sample magnetometer (VSM) with fields up to 14.5 kOe at room temperature.

4.3. Results and Discussion

4.3.1. Synthesis of Barium-doped Iron Oxide Nanoparticles

To prepare Ba-Fe-O NPs, $Fe(acac)_3$ and $Ba(stearate)_2$ were dissolved in 1-octadecene solution of oleic acid and oleylamine and the solution was heated at 320 ^{o}C for 1.5 h (see the Experimental Section). Ba composition in the NP structure was analyzed by inductively coupled plasma−atomic emission spectroscopy (ICP−AES). In the synthetic condition with the amount of $Fe(acac)_3$ (300 mg) and oleic acid (1 mL) fixed, the composition of Ba in Ba-Fe-O NPs was controlled by the amount/concentration of $Ba(stearate)_2$ or oleylamine (**Table 4-1**). For example, adding 20 mg of $Ba(stearate)_2$ to the reaction mixture produced Ba-Fe-O NPs with a Ba/Fe atomic ratio of 0.04, denoted as $Ba_{0.04}$-Fe-O. 40 mg (or 60 mg) of $Ba(stearate)_2$ gave $Ba_{0.055}$-Fe-O (or $Ba_{0.065}$-Fe-O) NPs. In the synthesis, we also noticed that oleylamine played two roles in NP stabilization and in promoting metal precursor decomposition.[29-30] Reacting 300 mg of $Fe(acac)_3$ with 60

mg of Ba-stearate in 8 mL oleylamine and 7 mL 1-octadecene yielded $Ba_{0.075}$-Fe-O NPs. By reducing 1-octadecene to 3 mL, $Ba_{0.082}$-Fe-O NPs were obtained. These NPs have the Ba composition close to the ideal Ba/Fe ratio of 0.083 in the pure BaFe phase. If only oleylamine was used as the solvent, then $Ba_{0.095}$-Fe-O NPs were synthesized. The Ba/Fe ratio of 0.095 is very close to the initial precursor ratio of $Ba(stearate)_2/Fe(acac)_3$ (0.099) used in the reaction, indicating almost complete precursor decomposition and metal ratio carry-over to the final Ba-Fe-O product.

Reaction	Ba(stearate)$_2$	Oleylamine	1-Octadecene	Ba Composition
1	20 mg	6 mL	12 mL	0.040
2	40 mg	6 mL	12 mL	0.055
3	60 mg	6 mL	12 mL	0.065
4	60 mg	8 mL	7 mL	0.075
5	60 mg	8 mL	3 mL	0.082
6	60 mg	8 mL	0 mL	0.095

Table 4-1. Experimental conditions for synthesizing Ba-Fe-O NPs with different Ba compositions (the amount of $Fe(acac)_3$ (300 mg) and oleic acid (1 mL) was fixed).

Figure 4-1A shows a typical transmission electron microscopy (TEM) image of the 15 ± 0.5 nm $Ba_{0.04}$-Fe-O NPs. The high-resolution TEM image of a representative NP is shown in **Figure 4-1B**. The distance of the lattice fringe was measured to be ~2.6 Å, corresponding to the lattice spacing of (311) planes in the spinel Fe_3O_4. Obvious crystal defects exist in the NP as marked by dashed ellipses, which can be ascribed to the lattice mismatch caused by Ba doping. **Figure 4-1C** shows the TEM image of the monodisperse $Ba_{0.082}$-Fe-O NPs of 13 ± 0.5 nm.
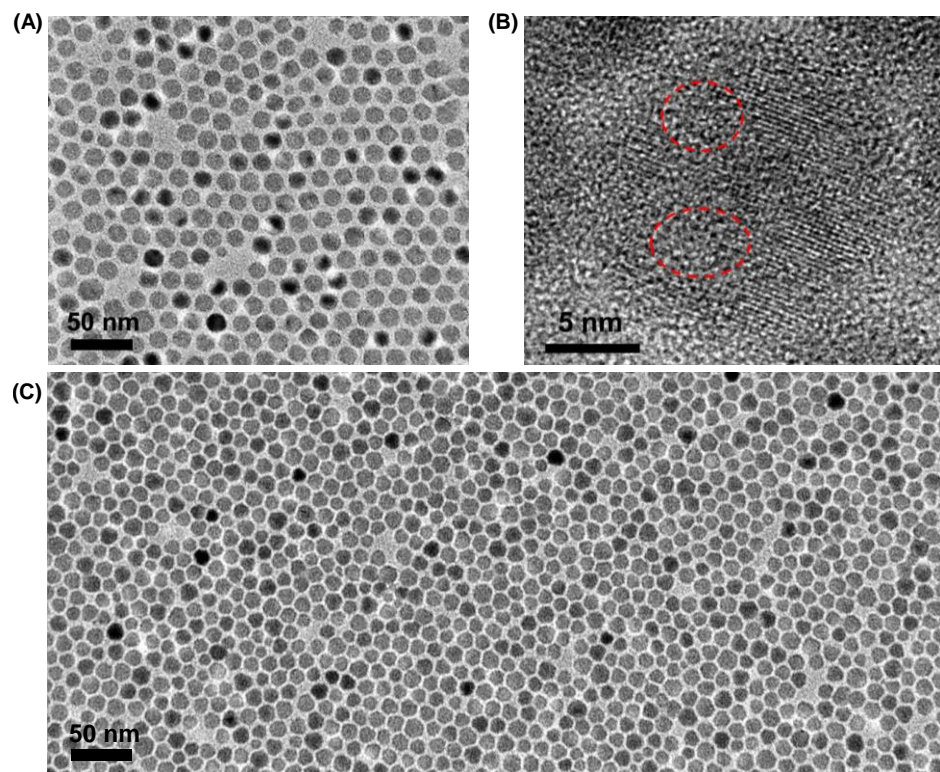
Figure 4-1. (A) TEM image of the as-synthesized $Ba_{0.04}$-Fe-O NPs. (B) HR-TEM image of a representative $Ba_{0.04}$-Fe-O NP. (C) TEM image of the as-synthesized $Ba_{0.082}$-Fe-O NPs.

TEM images of the as-synthesized Ba-Fe-O NPs with other Ba compositions are shown in **Figure 4-2**. For the synthesis of Ba-Fe-O NPs using 1-octadecene as the solvent, the morphology of the obtained NPs is spherical/polyhedral with the size of 13-15 nm. If using oleylamine as both the solvent and surfactant, the obtained $Ba_{0.095}$-Fe-O NPs are not well-shaped, probably due of the faster nucleation and growth rate caused by the oleylamine. The Ba-Fe-O NPs were further characterized by energy dispersive X-ray (EDX) spectroscopy. **Figure 4-3** is the EDX spectrum of the $Ba_{0.082}$-Fe-O NPs deposited on Si, confirming the existence of Ba and Fe at the atomic ratio of 0.093, which is close to that obtained from the ICP−AES analysis.
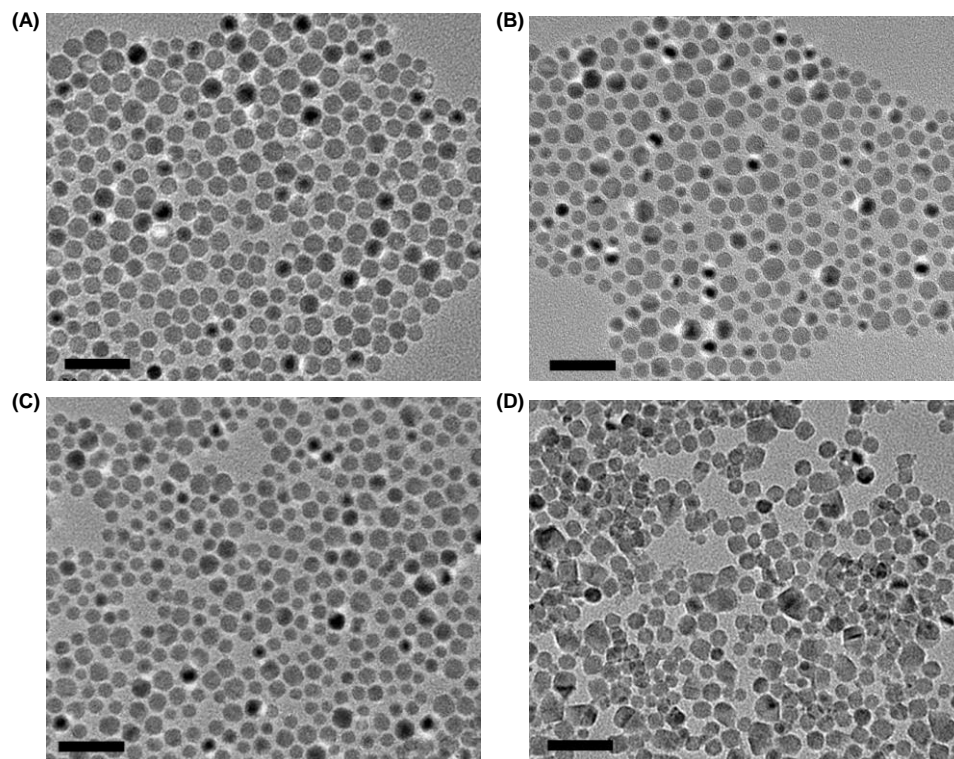
Figure 4-2. TEM images of the as-synthesized Ba-Fe-O NPs with different Ba compositions. (A) $Ba_{0.055}$-Fe-O NPs. (B) $Ba_{0.065}$-Fe-O NPs. (C) $Ba_{0.075}$-Fe-O NPs. (D) $Ba_{0.095}$-Fe-O NPs. All scale bars represent 50 nm.
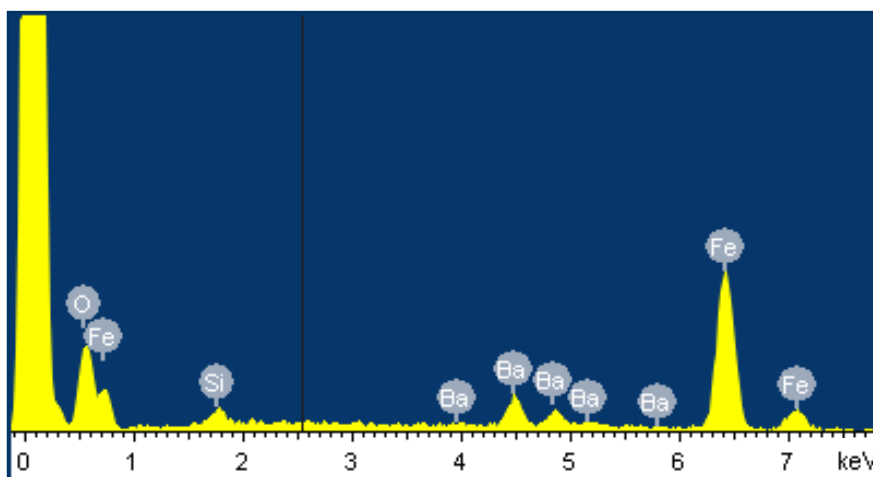
Figure 4-3. EDX spectrum of the $Ba_{0.082}$-Fe-O NPs deposited on a Si substrate.

4.3.2. Conversion of Ba-Fe-O Nanoparticles into BaFe Nanoparticles

X-ray diffraction (XRD) pattern of the as-synthesized $Ba_{0.04}$-Fe-O NPs is shown in **Figure 4-4A**. The pattern matches with the spinel Fe_3O_4 structure but the broad diffraction peaks infer the presence of small crystalline domains within each NP, which supports what is observed from **Figure 4-1B**. The magnetic hysteresis loop of the as-synthesized $Ba_{0.04}$-Fe-O NPs (**Figure 4-4B**) indicates that these NPs are superparamagnetic. Due to the existence of Ba and the induced crystal defects, the saturation moment (M_s) of the NPs is relatively small (~31 emu/g) compared to the pure single crystalline Fe_3O_4 NPs at a similar size (~ 65 emu/g).[29] In order to convert the as-synthesized Ba-Fe-O NPs into BaFe NPs, we first tested different annealing conditions to ensure that Fe_3O_4 structure could be oxidized to α-Fe_2O_3,[31] and BaFe phase was formed via the diffusion of Ba^{2+} into α-Fe_2O_3 lattice.[32] In O_2 at 600 ^{o}C for 1 h, the $Ba_{0.04}$-Fe-O NPs show no obvious structure change and diffraction peaks become sharper (**Figure 4-4A**), indicating the annealing enlarge the crystal domain within each NP, which is further supported by their superparamagnetic property with higher M_s than the as-synthesized NPs (**Figure 4-4B**). $Ba_{0.082}$-Fe-O NPs behave similarly once annealed the same way, as shown in the superparamagnetic hysteresis loop in **Figure 4-5**. It is worth mentioning that the saturation moment (35 emu/g) of the $Ba_{0.082}$-Fe-O NPs after annealing in O_2 at 600 ^{o}C for 1 h is even lower than that for $Ba_{0.04}$-Fe-O NPs (50 emu/g). This is because of the increasing impurity of Ba in the Fe-O matrix.
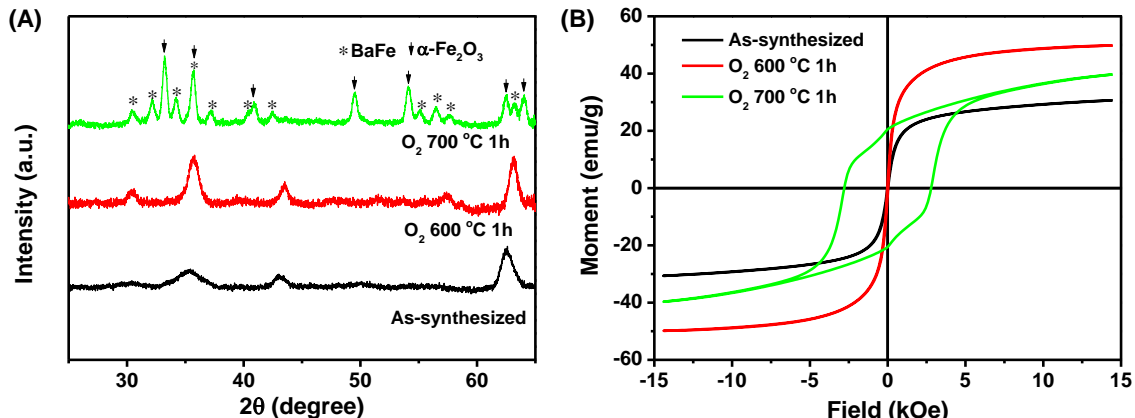
Figure 4-4. (A) XRD patterns and (B) Room temperature hysteresis loops of the $Ba_{0.04}$-Fe-O NPs before and after O_2 annealing treatment.
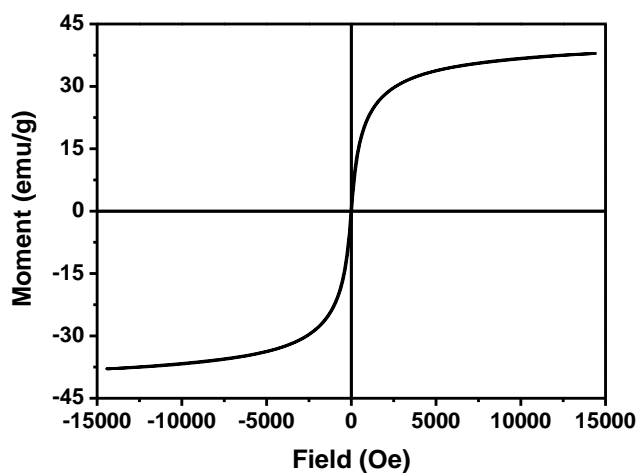
Figure 4-5. Hysteresis loop of $Ba_{0.082}$-Fe-O NPs after annealing in O_2 at 600 ^{o}C for 1h.

When annealed at 700 ^{o}C in O_2 for 1 h, the as-synthesized $Ba_{0.04}$-Fe-O NPs are converted into hexagonal BaFe, as confirmed in the XRD pattern in **Figure 4-4A**. The hysteresis loop of the obtained hexagonal BaFe in **Figure 4-4B** shows that it is ferromagnetic with the coercivity (H_c) of ~2800 Oe and M_s of 40 emu/g. However, both XRD and magnetic data (the loop shows a two-phase behavior) indicate that in the annealed $Ba_{0.04}$-Fe-O NPs, the α-Fe_2O_3 phase co-exists with the BaFe phase. This is due to the non-stoichiometric composition of Ba in the NP structure.

88

The increase of Ba composition from 0.055 to 0.065 reduces the amount of α-Fe_2O_3 presented in the annealed Ba-Fe-O NPs (**Figure 4-6**). For the $Ba_{0.055}$-FeO_x NPs, after annealing treatment the hexagonal BaFe is the dominated crystalline phase. Different from the $Ba_{0.04}$-Fe-O NPs with obvious impurity of α-Fe_2O_3 phase after annealing, only obvious (104) diffraction peak at $2\theta = 33.3^o$ of α-Fe_2O_3 appeared. The increase of Ba composition from 0.055 to 0.065 caused obvious weakening of the α-Fe_2O_3 (104) diffraction peak. In contrast, when the Ba composition is above 0.075, no obvious diffraction peaks of α-Fe_2O_3 are observed for the annealed Ba-Fe-O NPs. The diffraction peaks of the annealed $Ba_{0.082}$-Fe-O NPs in **Figure 4-6** match well with those of the hexagonal BaFe, indicating the formation of pure BaFe phase. It is worth noting that our annealing is performed at lower temperature and shorter time than previous syntheses,[20-25] therefore, the NP morphology is better preserved.
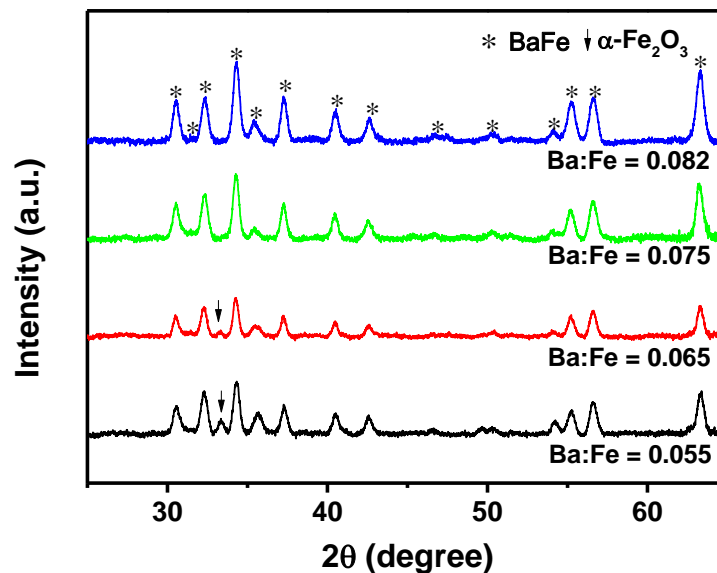
Figure 4-6. XRD patterns of the Ba-Fe-O NPs with different Ba compositions after annealing in O_2 at 700 ^{o}C for 1 h.

Ba/Fe composition dependent magnetic properties of the annealed Ba-Fe-O NPs were studied and their hysteresis loops are shown in **Figure 4-7**. As the Ba composition increases from 0.055 to 0.082, the H_c of the annealed NPs increases from 3120 Oe to 5260 Oe. Their M_s increase as well from 42 emu/g to 54 emu/g due to the increased BaFe phase purity, which is further confirmed by the single-phase hysteresis loop from the annealed $Ba_{0.082}$-Fe-O NPs. When the atomic ratio of Ba/Fe is over the optimal value required for the formation of BaFe (0.083) at 0.095, the annealed NPs show a decreased H_c (5150 Oe) and M_s (50 emu/g). **Figure 4-8** summarizes the H_c and M_s change of the hexagonal BaFe with different Ba compositions.
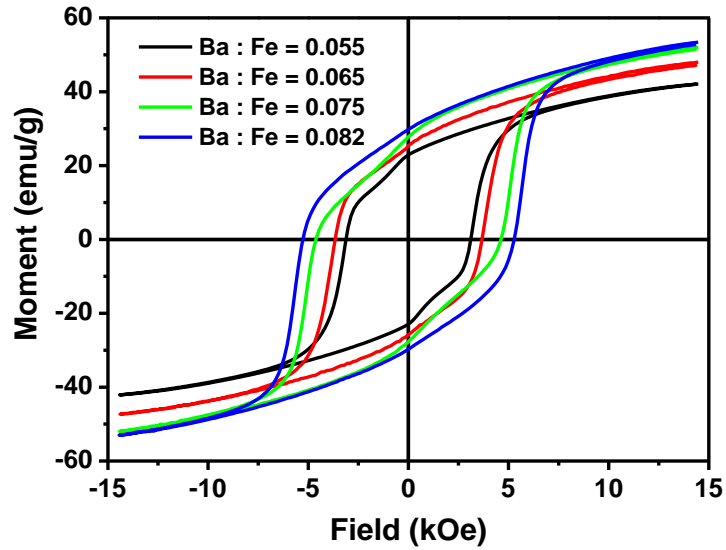
Figure 4-7. Room temperature hysteresis loops of the Ba-Fe-O NPs with different Ba compositions after annealing in O_2 at 700 ^{o}C for 1 h.
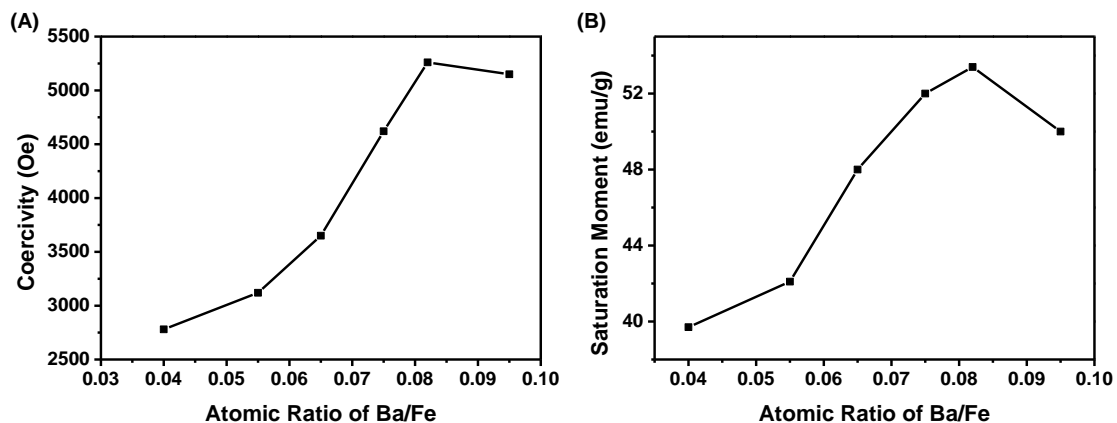
Figure 4-8. The change of magnetic coercivity and saturation moment of the annealed Ba-Fe-O NPs with different Ba compositions.

The above results demonstrate that the new synthetic method described in this paper is a facile approach to Ba-Fe-O and further to hard magnetic BaFe NPs. It is worth emphasizing that this synthetic method can be readily extended to the synthesis of Sr-Fe-O NPs. For example, by just replacing Ba(stearate)$_2$ with the same amount of Sr(stearate)$_2$ in the synthesis of Ba$_{0.082}$-Fe-O NPs, Sr-Fe-O NPs were synthesized (**Figure 4-9A**) with the size of 15 $\pm$ 1 nm. EDX spectrum in **Figure 4-9B** confirmed the Sr doping into Fe-O NPs with the Sr/Fe ratio of 0.078. After annealed at 700°C for 1 h in O$_2$, the NPs are ferromagnetic with the H_c of 4500 Oe and M_s of 50 emu/g (**Figure 4-10**), indicating the formation of hexagonal SrFe.
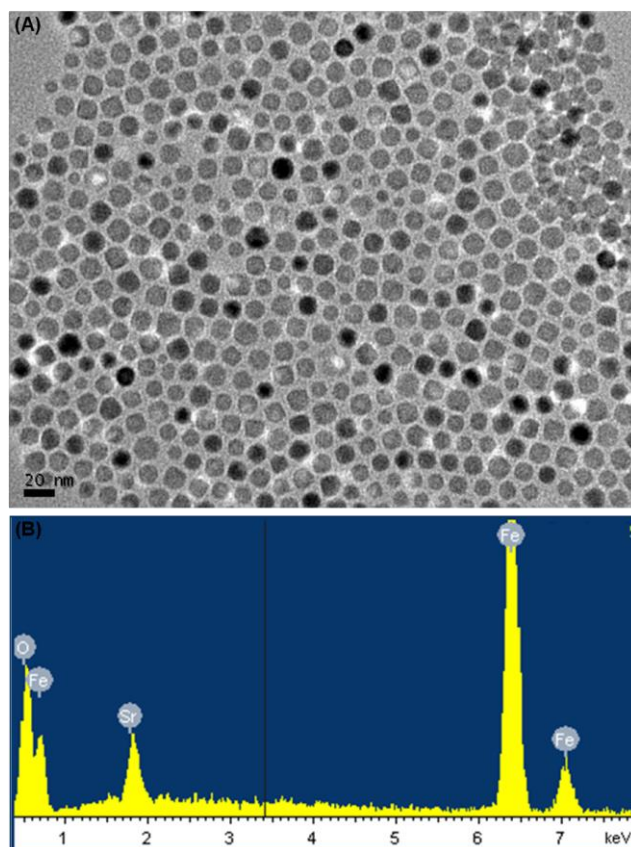
Figure 4-9. (A) TEM image of the as-synthesized $Sr_{0.078}$-Fe-O NPs. (B) EDX spectrum of the as-synthesized NPs deposited on a Si substrate.
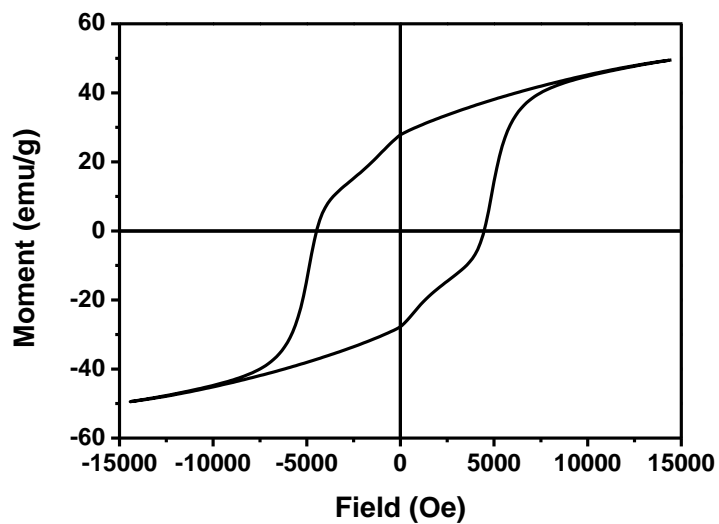
Figure 4-10. Hysteresis loop of the $Sr_{0.078}$-Fe-O NPs after annealing in O_2 at 700 ^{o}C for 1h.

4.3.3. Self-assembly of the Ba-Fe-O Nanoparticles and Their Conversion into BaFe Ferromagnetic Nanomagnets

The as-synthesized Ba-Fe-O NPs are well dispersed in hexane, allowing easy self-assembly of these NPs into well-defined NP arrays. Using water-air interface self-assembly method,[13] we fabricated a monolayer assembly of the $Ba_{0.082}$-Fe-O NPs. The morphology of the monolayer assembly is checked by TEM and SEM. **Figure 4-11A** shows a TEM image of the monolayer assembly transferred onto a carbon coated Cu grid. SEM image of the monolayer array transferred onto a Si substrate is also shown in **Figure 4-11B**. Those NPs are densely packed in the monolayer assembly. We utilized the same O_2 annealing treatment as described previous to convert the as-synthesized NPs into hexagonal BaFe NPs. After O_2 annealing at 700 ^{o}C for 1h, the morphology of the monolayer was well maintained, as shown in **Figure 4-12**. No obvious NP sintering/aggregation in the monolayer array was observed. However, hysteresis loop of the monolayer array after O_2 annealing (**Figure 4-13**) shows strong diamagnetic background from the SiO_2 substrate. The magnetic signal from the monolayer BaFe NP array is too weak to be detected. In order to increase the signal from the assembly, we prepared a multilayer array of the $Ba_{0.082}$-Fe-O NPs.
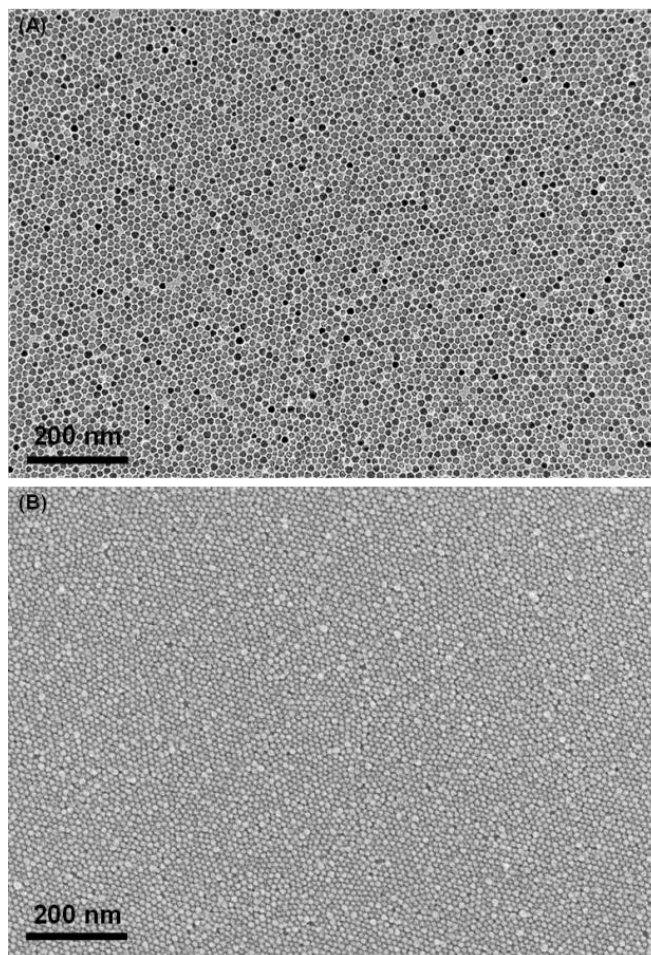
Figure 4-11. (A) TEM and (B) SEM image of the monolayer assembly of $Ba_{0.082}$-Fe-O NPs.
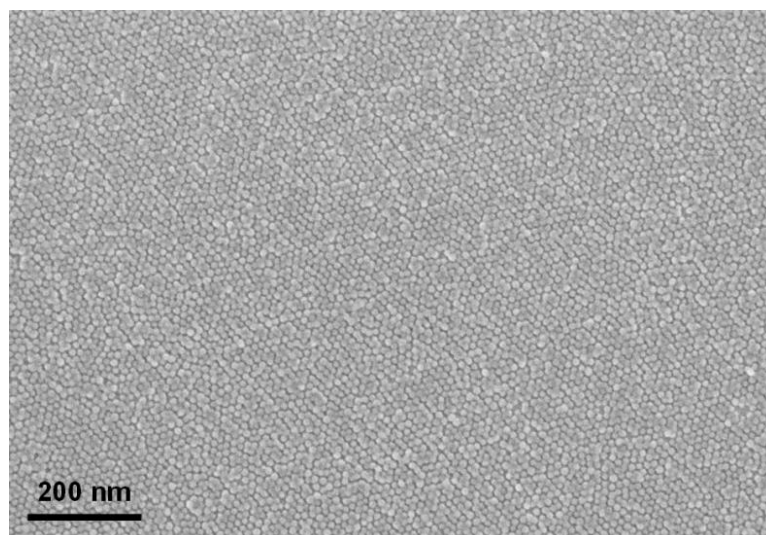
Figure 4-12. SEM image of the monolayer assembly of $Ba_{0.082}$-Fe-O NPs after O_2 annealing.
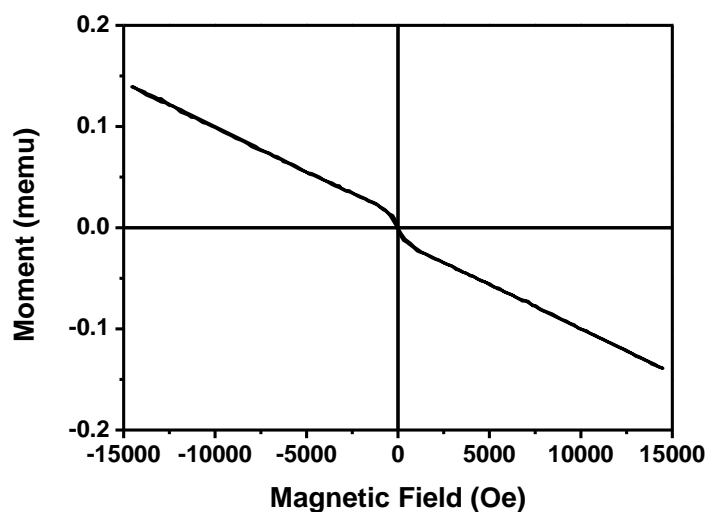
Figure 4-13. Hysteresis loop of annealed monolayer assembly of $Ba_{0.082}$-Fe-O NPs.

Multilayer assembly of the $Ba_{0.082}$-Fe-O NPs was fabricated by drop-casting the NP dispersion (0.5 mg/mL) directly on a Si substrate. Upon the evaporation of the solvent, densely packed assembly was obtained, as indicated by the SEM image in **Figure 4-14A**. SEM image of an edge of the assembled film created by physical scratching (**Figure 4-14B**) shows multilayer packing. Different from the monolayer assembly that maintains the morphology after O_2 annealing treatment, the multilayer assembly exhibits some NP aggregation/sintering after the same treatment (**Figure 4-14C**). However, the grain size of the NPs after annealing is still around 50 nm. Room temperature magnetic properties of the annealed multilayer assembly were measured using VSM with the assembled film perpendicular (out-of-plane) and parallel (in-plane) to the external field. **Figure 4-14D** is the hysteresis loops of the annealed multilayer assembly. The in-plane loop shows the H_c of 4100 Oe, which is much larger than that of the out-of-plane one (H_c = 2050 Oe). Moreover, the in-plane loop is squarer compared to the out-of-plane loop, suggesting the easy axis of the magnetization lies in the plane of the film. Such assembly may be

95

especially useful to fabricate 3D stacks of BaFe NPs as new nanostructured magnets for energy product optimization.
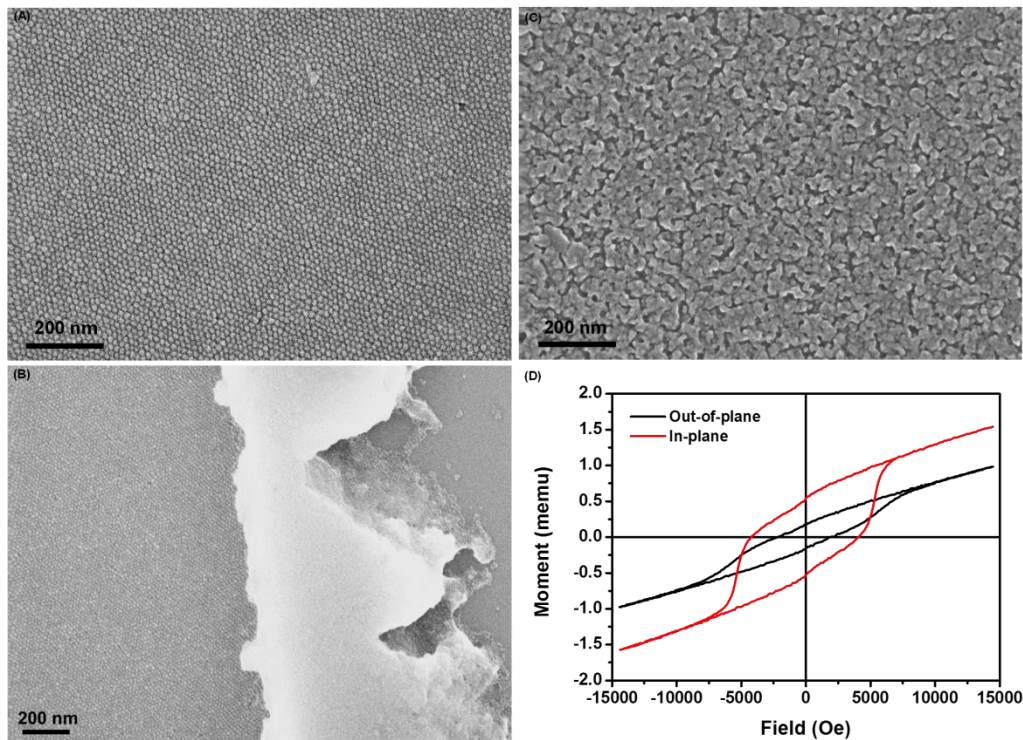
Figure 4-14. (A) SEM image of the multilayer assembly of $Ba_{0.082}$-Fe-O NPs. (B) SEM image of the edge of the multilayer assembly with a physical scratch showing the multilayer packing. (C) SEM image of the multilayer assembly after annealing in O_2 at 700 ^oC for 1h. (D) Hysteresis loop of the annealing multilayer assembly.

4.4. Conclusion

In summary, we have reported a facile organic-phase synthesis of monodisperse Ba-Fe-O NPs through thermal decomposition of $Ba(stearate)_2$ and $Fe(acac)_3$ in 1-octadecene with oleic acid and oleylamine as surfactants. The Ba/Fe composition is tuned from 0.04 to 0.095 by controlling the ratio of $Ba(strearate)_2/Fe(acac)_3$ or by the volume of oleylamine and 1-octadecene. The as-synthesized Ba-Fe-O NPs, especially the $Ba_{0.082}$-Fe-O NPs, can be easily converted into hexagonal BaFe by annealing in O_2 atmosphere at

700 ^{o}C for 1 h, showing strong ferromagnetic properties with H_c reaching 5260 Oe and M_s of 54 emu/g. More importantly, these monodisperse Ba-Fe-O NPs are well dispersed in hexane and can be easily assembled into densely packed 2D arrays and further converted into oriented BaFe magnets. Our reported synthetic method and self-assembly approach can also be extended to Sr-Fe-O and ferromagnetic SrFe NPs, providing a unique way of fabricating ferromagnetic ferrite arrays for magnetic energy and data storage applications.

REFERENCES

[1]   J. T. Jang, H. Nah, J. H. Lee, S. H. Moon, M. G. Kim, J. Cheon, *Angew. Chem. Int. Ed.* **2009**, *48*, 1234-1238.

[2]   W. K. Moon, J. Kim, H. S. Kim, N. Lee, T. Kim, H. Kim, T. Yu, I. C. Song, T. Hyeon, *Angew. Chem. Int. Ed.* **2008**, *47*, 8438-8441.

[3]   K. Cheng, S. Peng, C. J. Xu, S. H. Sun, *J. Am. Chem. Soc.* **2009**, *131*, 10637-10644.

[4]   T. Hyeon, J. E. Lee, N. Lee, H. Kim, J. Kim, S. H. Choi, J. H. Kim, T. Kim, I. C. Song, S. P. Park, W. K. Moon, *J. Am. Chem. Soc.* **2010**, *132*, 552-557.

[5]   J. H. Lee, Y. M. Huh, Y. Jun, J. Seo, J. Jang, H. T. Song, S. Kim, E. J. Cho, H. G. Yoon, J. S. Suh, J. Cheon, *Nat. Med.* **2007**, *13*, 95-99.

[6]   J. H. Lee, J. T. Jang, J. S. Choi, S. H. Moon, S. H. Noh, J. W. Kim, J. G. Kim, I. S. Kim, K. I. Park, J. Cheon, *Nat. Nanotechnol.* **2011**, *6*, 418-422.

[7]   C. Xu, J. Xie, D. Ho, C. Wang, N. Kohler, E. G. Walsh, J. R. Morgan, Y. E. Chin, S. Sun, *Angew. Chem. Int. Ed.* **2008**, *47*, 173-176.

[8]   C. J. Xu, B. D. Wang, S. H. Sun, *J. Am. Chem. Soc.* **2009**, *131*, 4216-4217.

[9]   N. Poudyal, J. P. Liu, *J. Phys. D: Appl. Phys.* **2013**, *46*.

[10]   J. Park, Y. K. Hong, S. G. Kim, S. Kim, L. S. I. Liyanage, J. Lee, W. Lee, G. S. Abo, K. H. Hur, S. Y. An, *J. Magn. Magn. Mater.* **2014**, *355*, 1-6.

[11]   R. C. Pullar, *Prog. Mater. Sci.* **2012**, *57*, 1191-1334.

[12]   Q. Dai, D. Berman, K. Virwani, J. Frommer, P. O. Jubert, M. Lam, T. Topuria, W. Imaino, A. Nelson, *Nano Lett.* **2010**, *10*, 3216-3221.

[13] L. Wu, P. O. Jubert, D. Berman, W. Imaino, A. Nelson, H. Zhu, S. Zhang, S. Sun, *Nano Lett.* **2014**, *14*, 3395-3399.

[14] Z. V. Golubenko, L. P. Ol'khovik, Y. A. Popkov, Z. I. Sizova, A. S. Kamzin, *Phys. Solid State.* **1998**, *40*, 1718-1720.

[15] J. Wang, F. Zhao, W. Wu, G. M. Zhao, *J. Appl. Phys.* **2011**, *110*.

[16] D. Berman, R. Biskeborn, N. Bui, E. Childers, R. D. Cideciyan, W. Dyer, E. Eleftheriou, D. Hellman, R. Hutchins, W. Imaino, G. Jaquette, J. Jelitto, P. O. Jubert, C. Lo, G. McClelland, S. Narayan, S. Oelcer, T. Topuria, T. Harasawa, A. Hashimoto, T. Nagata, H. Ohtsu, S. Saito, *IEEE Trans. Magn.* **2007**, *43*, 3502-3508.

[17] T. Harasawa, R. Suzuki, O. Shimizu, S. Olcer, E. Eleftheriou, *IEEE Trans. Magn.* **2010**, *46*, 1894-1897.

[18] P. O. Jubert, B. Biskeborn, D. N. Qiu, A. Matsumoto, H. Noguchi, O. Shimizu, *IEEE Trans. Magn.* **2011**, *47*, 386-394.

[19] G. Cherubini, R. D. Cideciyan, L. Dellmann, E. Eleftheriou, W. Haeberle, J. Jelitto, V. Kartik, M. A. Lantz, S. Olcer, A. Pantazi, H. E. Rothuizen, D. Berman, W. Imaino, P. O. Jubert, G. McClelland, P. V. Koeppe, K. Tsuruta, T. Harasawa, Y. Murata, A. Musha, H. Noguchi, H. Ohtsu, O. Shimizu, R. Suzuki, *IEEE Trans. Magn.* **2011**, *47*, 137-147.

[20] L. C. Li, K. Y. Chen, H. Liu, G. X. Tong, H. S. Qian, B. Hao, *J. Alloy Compd.* **2013**, *557*, 11-17.

[21] A. Yourdkhani, D. Caruntu, A. K. Perez, G. Caruntu, *J. Phys. Chem. C* **2014**, *118*, 1774-1782.

[22]   P. Xu, X. J. Han, M. J. Wang, *J. Phys. Chem. C* **2007**, *111*, 5866-5870.

[23]   J. Zhang, J. Fu, F. Li, E. Xie, D. Xue, N. J. Mellors, Y. Peng, *ACS Nano* **2012**, *6*, 2273-2280.

[24]   M. Manikandan, C. Venkateswaran, *J. Magn. Magn. Mater.* **2014**, *358*, 82-86.

[25]   D. Lisjak, S. Ovtar, *J. Phys. Chem. B* **2013**, *117*, 1644-1650.

[26]   D. Primc, D. Makovec, *Nanoscale* **2015**, *7*, 2688-2697.

[27]   D. Primc, D. Makovec, D. Lisjak, M. Drofenik, *Nanotechnology* **2009**, *20*.

[28]   J. Jalli, Y. K. Hong, S. Bae, G. S. Abo, J. J. Lee, J. C. Sur, S. H. Gee, S. G. Kim, S. C. Erwin, A. Moitra, *IEEE Trans. Magn.* **2009**, *45*, 3590-3593.

[29]   Z. C. Xu, C. M. Shen, Y. L. Hou, H. J. Gao, S. S. Sun, *Chem. Mater.* **2009**, *21*, 1778-1780.

[30]   S. Mourdikoudis, L. M. Liz-Marzan, *Chem. Mater.* **2013**, *25*, 1465-1476.

[31]   Y. L. Hou, Z. C. Xu, S. H. Sun, *Angew. Chem. Int. Ed.* **2007**, *46*, 6329-6332.

[32]   H. P. Steier, J. Requena, J. S. Moya, *J. Mater. Res.* **1999**, *14*, 3647-3652.

Chapter 5. Stable Cobalt Nanoparticles and Their Monolayer Array as an Efficient Electrocatalyst for Oxygen Evolution Reaction

5.1. Introduction

Oxygen evolution reaction (OER) is commonly referred to as electrochemical oxidation of "O^{2-}" to O_2. It is an important half-cell reaction and is coupled with hydrogen evolution reaction (HER) in a water-splitting cell for efficient proton reduction and hydrogen (H_2) generation.[1-3] As a thermodynamically "up-hill" reaction that involves multi-electron transfer, it requires the input of energy to drive its completion. In order to lower the kinetic barrier, an efficient catalyst is needed to promote the 4-electron oxidation process and make OER proceed at low overpotential. For this purpose, nanostructured iridium (Ir) or ruthenium (Ru) has been chosen as the-state-of-the-art OER catalysts.[4-10] Recently, earth-abundant transition metal oxides/hydroxides,[11-21] especially Co-O-based complexes,[22-25] thin films,[26-29] nanoparticles (NPs),[30-39] and layered structure,[40-43] are also explored as promising alternative catalysts for OER. However, these oxides have generally low electron conductivities, limiting their potential in electrocatalysis enhancemen.

One recent strategy applied to improve the OER catalytic activity of these oxides is to couple them with a conductive support such as graphene,[17] carbon nanotubes,[14, 33] metallic Au,[26, 44] or even Au NPs, as demonstrated in the core/shell Au/Co_3O_4 structure.[35] These studies indicate that catalytic activity may be further enhanced if the catalyst can be made more electron-conductive. Studying the general designs of the catalysts, we see that these conductive supports can only offer a partial solution to the desired enhancement in catalysis, as the electron transfer required for the OER on the catalytically active surface may only be possible at the catalyst-support interface, not entirely on the catalyst surface. To further enhance the OER activity on the catalyst

surface, the catalyst itself is better conductive to facilitate electron transfer for the OER.[45] This makes metallic Co NPs a promising catalyst choice. However, it is known that metallic Co NPs are chemically unstable, subject to fast oxidation when exposed to air or in an oxygenated solvent. It is therefore essential to stabilize metal Co NPs first before they can be studied for the OER. In this chapter, we report that when synthesized and treated properly, metallic Co NPs can be stabilized to serve as a new class of efficient catalyst for OER in 0.1 M KOH. Moreover, using a water-air interface self-assembly method, we prepared a well-defined monolayer array of Co NPs on the glassy carbon (GC) plate. The uniform Co NP array allows the detailed evaluation of the Co NP catalysis for OER. The monolayer catalyst shows about 15 times higher turnover frequency (TOF) and mass activity than the Co NPs deposited on conventional carbon support. The high activity and stability of the Co NPs make them among the best Co-based OER catalysts ever reported, even superior to the commercial Ir-catalyst (~ 2 nm Ir NPs on Vulcan carbon from Premetek Co.).

5.2. Experimental Section

Chemicals: Cobalt carbonyl ($Co_2(CO)_8$, stabilized with 1-5% hexane) was purchased from Strem Chemicals. Dioctylamine (98%), oleic acid (90%), 1,2,3,4-tetrahydronaphthalene (99%), and Nafion solution (5% in a mixture of lower aliphatic alcohols and water) were purchased from Sigma-Aldrich. The commercial Ir catalyst (10% mass loading on Vulcan carbon, particle diameter ~2 nm) was obtained from Premetek Co.. All chemicals were used without further purification.

Characterization: Transmission electron microscopy (TEM) images were collected from a Philips CM20 with operating voltage of 200 kV. High-resolution TEM (HR-TEM) images were obtained using a JEOL 2010 with an accelerating voltage of 200 kV. SEM images of the monolayer assembly were acquired on a LEO 1530 microscope at an operating voltage of 10 kV. X-ray diffraction (XRD) patterns of the NPs were collected on a Bruker AXS D8-Advanced diffractometer with Cu Kα radiation (λ = 1.5418 Å). Magnetic studies were performed on a Lakeshore 7404 high-sensitivity vibrating sample magnetometer (VSM) with fields up to 1.5 T at room temperature. The actual mass loading of Co on the carbon support was determined by elemental analysis using a JY2000 Ultrace ICP Atomic Emission Spectrometer. Ex-situ soft X-ray absorption spectroscopy (XAS) measurements on Co L-edge were done on Beamline 6.3.1.2 (ISAAC) at the Advanced Light Source, Lawrence Berkeley National Laboratory. All the XAS measurements were recorded in the total-electron-yield detection mode to make them sensitive to the surface of the NPs.

Synthesis of Co NPs: Uniform Co NPs were synthesized through thermal decomposition of $Co_2(CO)_8$. Briefly, 18 mL of 1,2,3,4-tetrahydrophthalene was mixed with 0.35 mL of oleic acid and 0.5 mL of dioctylamine and heated to 110 ℃ for 0.5 h under argon protection and then cooled down to room temperature. 0.54 g of $Co_2(CO)_8$ was quickly added into the above mixture, which was reheated to 100 ℃ for 20 min under argon flow. Then the solution was rapidly heated to 210 ℃ at the heating rate of 15 ℃/min under the blanket of argon and kept at this temperature for 30 min. After cooling down to room temperature by removing the heating mantle, the obtained Co NPs were precipitated with 60 mL of ethanol and collected by centrifugation (8500 rpm, 8 min).

The Co NPs were washed again with hexane and ethanol and then dispersed in hexane for further use.

Synthesis of carbon supported Co (C-Co) NPs: To prepare C-Co NPs, 20 mg of Ketjen carbon was dispersed in 10 mL of hexane under ultrasonication. 20 mg of Co NPs dispersed in 5 mL of hexane was added to the carbon support dropwise under sonication. After sonicating for 30 min, the C-Co NPs were collected by centrifugation and washed with ethanol twice and then dried under ambient condition. The acurate NP/C mass ratio is measured to be 42% by ICP-AES. The obtained C-Co NPs were annealed in Ar + 5% H_2 at 600 ^{o}C for 1 h to obtaine metallic C-Co NPs.

To make C-CoO NPs, the as-synthesized C-Co NPs were annealed in O_2 at 150 ^{o}C for 12 h.

Monolayer Assembly of Co NPs: Large-area monolayer assembly of the 10 nm Co NPs was fabricated through water-air interface self-assembly. Briefly, the NPs were dispersed in a mixture of toluene and hexane (volume ratio of 1:2) at the concentration of 0.5 mg/mL. 150 μL of the dispersion was drop-cast onto the surface of deionized water in a Teflon column, which was then slowly dried at room temperature. After complete evaporation of organic solvent, the monolayer assembly of Co NPs floating on the water surface was transferred onto Cu TEM grids and glassy carbon plate electrode for further characterization.

Electrochemical Measurements: Electrochemical measurements were carried out on an Autolab 302 potentiostat with glassy carbon rotating disk (5 mm in diameter) as a working electrode, Ag/AgCl (4 M KCl) as a reference electrode, and platinum wire as a

counter electrode. The reference was calibrated vs. reversible hydrogen electrode (RHE) before the measurements and all potentials were converted to the RHE scale. The catalyst was dispersed in a mixture containing water, isopropanol, and Nafion solution (5 wt%) (v/v/v 4:1:0.05, catalyst concentration: 2 mg/mL) by 30 min of sonication to form a homogeneous ink. Then 20 µL of catalyst ink was casted on the newly polished glassy carbon electrode and dried at ambient condition (loading 0.2 mg/cm^2). The catalyst was first subject to cyclic voltammetry (CV) scans between 0 and 1 V at 100 mV/s in N$_2$-saturated 0.1 M KOH until a stable CV was obtained. Then OER polarization curves were recorded by linear-sweep voltammetry (LSV) at a scan rate of 10 mV/s in O$_2$-saturated 0.1 M KOH with the GC-RDE rotating at 1600 rpm. Chronoamperometry data were collected for the annealed Co NPs and commercial Ir NPs at an overpotential of 0.4 V.

5.3. Results and Discussion

5.3.1. Synthesis of Stable Co Nanoparticles

The Co NPs were synthesized through the thermal decomposition of cobalt carbonyl [Co$_2$(CO)$_8$] in 1,2,3,4-tetrahydronaphthalene solution with oleic acid and dioctylamine as surfactants, as described in the experimental section.[46-47] **Figure 5-1A** shows a typical transmission electron microscopy (TEM) image of the as-synthesized Co NPs that are monodisperse with the diameter of 10 ± 1 nm. The as-synthesized Co NPs were then loaded on Ketjen carbon (C) at an initial mass ratio of 1:1 through sonication of Co NP dispersion and C support in hexane, denoted as C-Co NPs (**Figure 5-1B**). Inductively

coupled plasma atomic emission spectroscopy (ICP-AES) analysis confirmed the mass ratio of Co NPs in the C-Co catalyst was 42%.
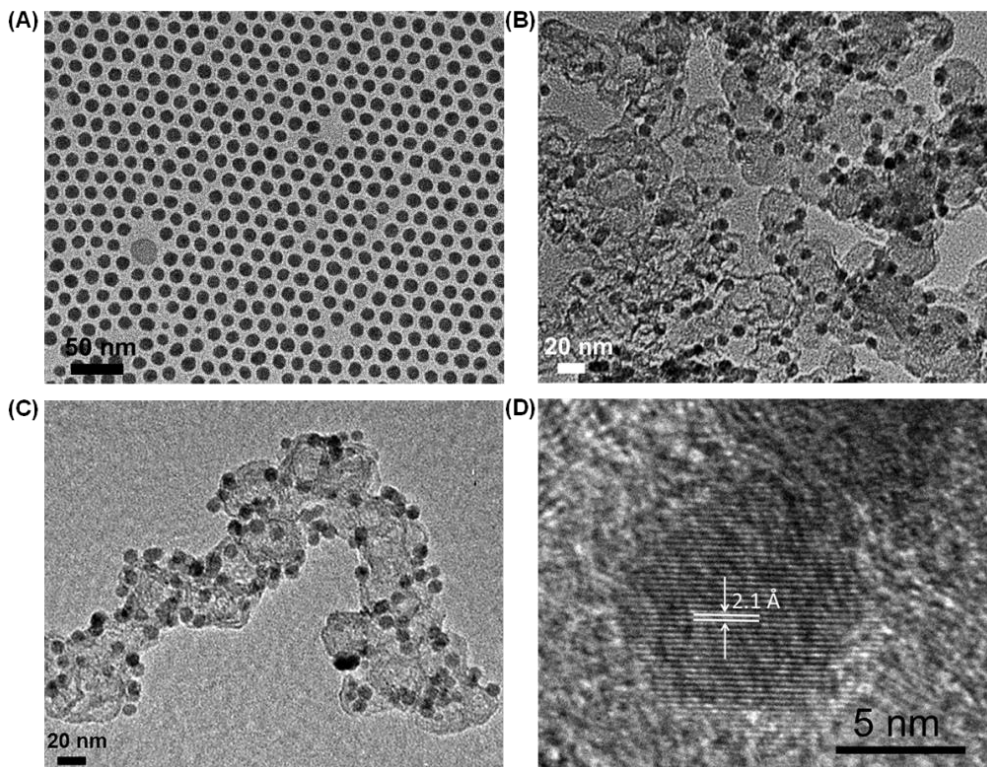
Figure 5-1. TEM images of (A) as-synthesized Co NPs. (B) The Co NPs loaded on C support (C-Co NPs). (C) The C-Co NPs after reductive annealing at 600 $^{\circ}$C for 1 h. (D) HR-TEM image of a representative Co NP in (C).

As demonstrated previously,[46] the as-synthesized magnetic Co NPs are not stable and subject to fast oxidation. To improve their stability, these C-Co NPs were annealed in Ar + 5% H$_2$ at 600 $^{\circ}$C for 1 h. This reductive annealing reduces the surface oxide to metallic Co, increases the Co crystallinity, and removes the surfactants to activate the catalyst for the subsequent electrochemical measurements. The TEM image of the annealed C-Co NPs in **Figure 5-1C** shows that due to the C-support stabilization, the annealing does not cause any sign of Co NP aggregation. High-resolution TEM (HR-

TEM) image of a representative Co NP deposited on C in **Figure 5-1D** confirms that the annealed Co NP is indeed well-crystallized with the lattice fringe spacing measured to be 2.1 Å, which is close to the (111) inter-planar spacing of the face-centered-cubic (fcc) Co. Due to the fast oxidation of the as-synthesized Co NPs, the C-Co NPs show no obvious X- ray diffraction (XRD) peaks from Co NPs. In the contrary, XRD pattern of the annealed C-Co NPs in **Figure 5-2** displays clear diffraction peaks, which can be ascribed to the (111) and (200) peaks of face-centered cubic Co. This result further reveals the crystallinity of Co NPs significantly enhanced after reductive annealing.
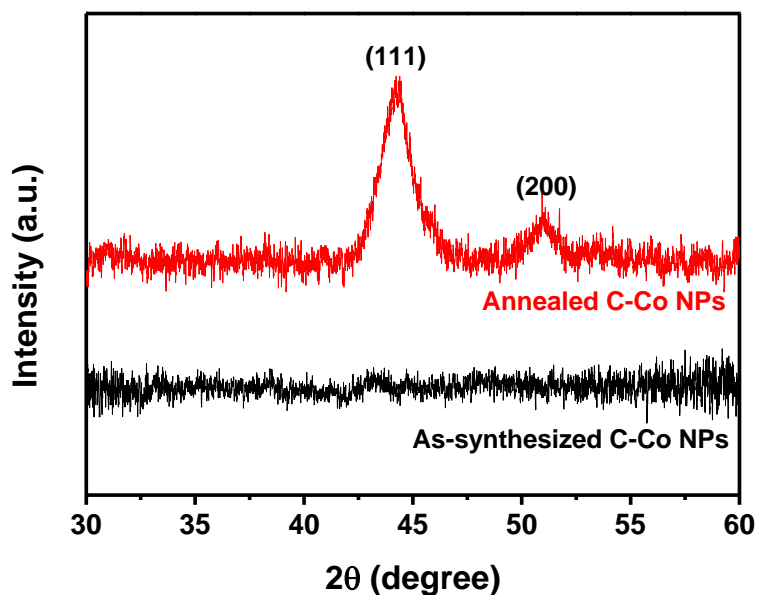
Figure 5-2. XRD patterns of the C-Co NPs before and after reductive annealing at 600 ^{o}C for 1 h.

Ex-situ X-ray absorption spectroscopy (XAS) was applied to study the chemical states of the annealed Co NPs. The XAS measurements were performed in the total-electron-yield detection mode to make them sensitive to the surface of the Co NPs. The XAS spectrum of the Co L-edge of the annealed Co NPs in **Figure 5-3** shows two peaks

at 778.0 eV and 793.3 eV that match those for the metallic Co reference foil, indicating that the surface of the annealed Co NPs is in metallic nature without obvious surface oxidation.
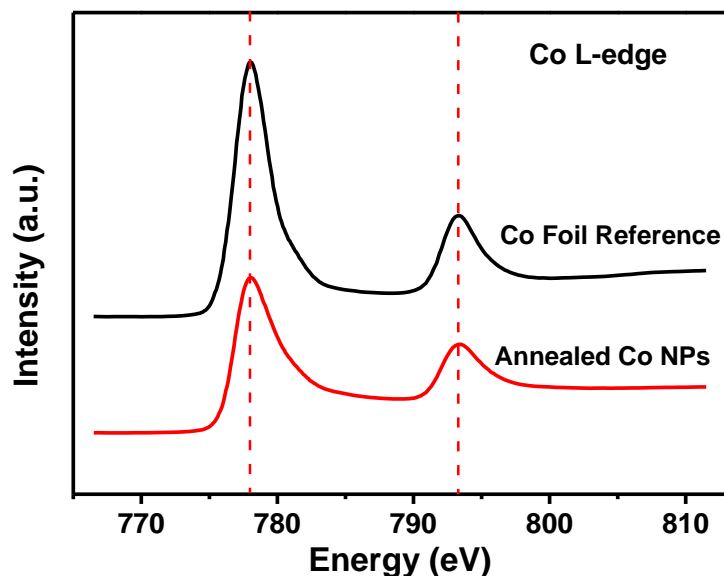
Figure 5-3. Ex-situ XAS spectra of Co L-edge of Co reference foil and the annealed C-Co NPs.

Chemical stability of the annealed C-Co NPs was monitored by the change of their magnetic properties using a vibrating sample magnetometer. **Figure 5-4A** is room-temperature magnetic hysteresis loops of the C-Co NPs before and after reductive annealing in Ar + 5% H_2 at 600 ^{o}C for 1 h. The magnetic moments were normalized to the mass of Co. Due to the surface oxidation, the initial Co NPs on the carbon support are superparamagnetic with the magnetic saturation moment (M_s) of 52 emu/g. After the reductive annealing, their M_s increases to 142 emu/g, which is close to the bulk value (~162 emu/g), and the annealed NPs show weak ferromagnetism with a coercivity of 120 Oe. The M_s change of the Co NPs exposed to air was monitored, as shown in **Figure 5-**

4B. The M_s of the as-synthesized Co NPs drops to 39 emu/g after 1 day and further decreases to 28 emu/g after 30 days (46% loss). As a comparison, the annealed Co NPs are much more stable with their M_s staying at 129 emu/g level even after 30 days, indicating that annealing indeed helps to stabilize Co NPs against air oxidation. This stability enhancement is even more significant than that for crystalline bcc-Fe NPs reported previously.[48-49]
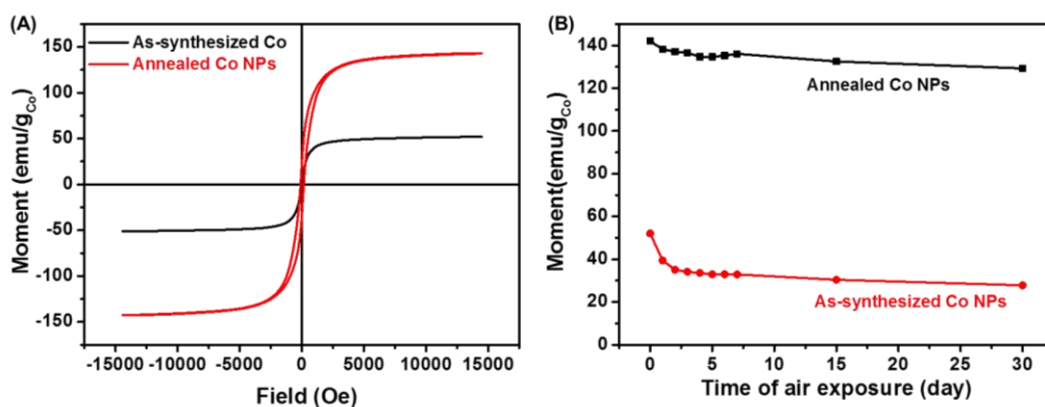
Figure 5-4. Room temperature hysteresis loops of the C-Co NPs before and after reductive annealing. (F) The change of magnetic moment of the Co NPs versus the time of air exposure at room temperature.

5.3.2. Oxygen Evolution Activity of the Cobalt Nanoparticles

The OER activity of the annealed Co NPs was evaluated in O_2-saturated 0.1 M KOH solution using a standard three-electrode system. The C-Co NP catalyst was cast onto the glassy carbon (GC) working electrode. The OER polarization curves were recorded by linear sweep voltammetry (LSV) at the scan rate of 10 mV/s and continuous rotating speed of 1600 rpm. **Figure 5-5** shows the polarization curves of the annealed C-Co catalyst with three different mass loadings without iR-correction. Two anodic peaks are observed at ca. 1.10 V and 1.46 V, respectively. The first peak is attributed to the

electrochemical oxidation of Co^{II} to Co^{III} and the second one can be assigned to further oxidation of Co^{III} to Co^{IV}.[26, 30] The overpotential at the current density of 10 mA/cm^2, which is normally used for evaluating the electrochemical activity of an OER catalyst,[11, 50] decreased from 0.45 V to 0.39 V while increasing the catalyst loading from 0.05 mg/cm^2 to 0.2 mg/cm^2. Further increasing the mass loading resulted in thicker catalyst film, causing limited mass transport and detachment of catalyst from the electrode during electrochemical measurement. Thus the optimal catalyst loading of 0.2 mg/cm^2 was chosen for the further study.
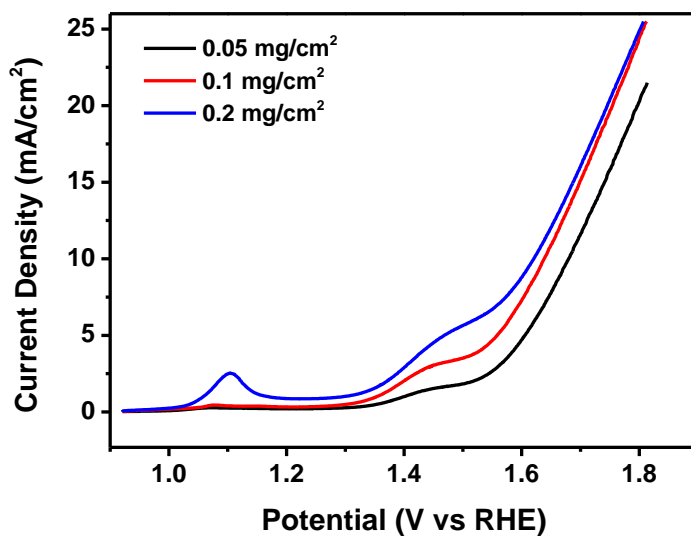
Figure 5-5. Polarization curves of the annealed C-Co NPs on GC electrode at three different mass loadings. The measurements were performed on GC electrode in 0.1 M KOH at the scan rate of 10 mV/s and rotating speed of 1600 rpm.
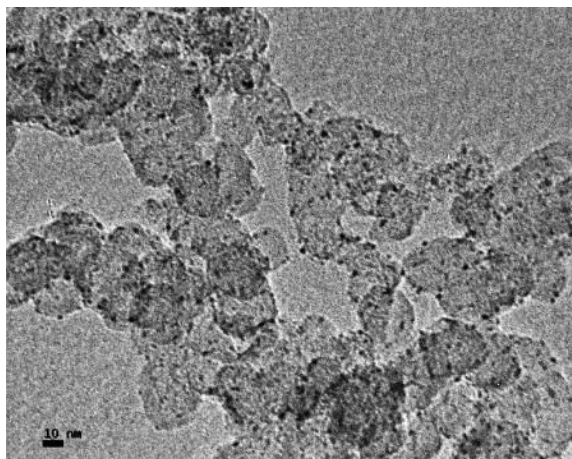
Figure 5-6. TEM image of the commercial Ir catalyst with 10 wt% Ir on Vulcan carbon black.

To better evaluate the OER activity of the annealed C-Co NPs catalyst, the commercial Ir catalyst (10 wt% Ir on Vulcan carbon black from Premetek Co.) was chosen as a reference. **Figure 5-6** is the TEM image of the commercial Ir catalyst. The size of the Ir NPs is ~ 2 nm. The polarization curve of the commercial Ir catalyst with the same mass loading of 0.2 mg/cm^2 is shown in **Figure 5-7A**. At a current density of 10 mA/cm^2, the overpotential for the annealed Co NPs was ~10 mV lower than the commercial C-Ir catalyst. We also tested the OER activity of the as-synthesized Co NPs. The annealed Co NPs exhibited much higher current density at all potentials and much smaller overpotential at the current density of 10 mA/cm^2 (0.39 V vs 0.43 V) than the as-synthesized Co NPs. During electrochemical oxidation, the surface of the Co NPs was oxidized to Co^{III} and Co^{IV}.[26] The metallic core of the annealed Co NPs increased their electrical conductivity and thus enhanced the catalytic activity. It is worth mentioning that all the polarization curves shown here are without any iR-correction. If considering the uncompensated resistance of the electrochemical cell, the overpotential for producing a current density of 10 mA/cm^2 decreased to ~0.3 V after iR-correction (**Figure 5-7B**),

which is comparable or even smaller than the values of some other non-precious catalysts under similar experimental conditions.[14, 16, 35, 42]
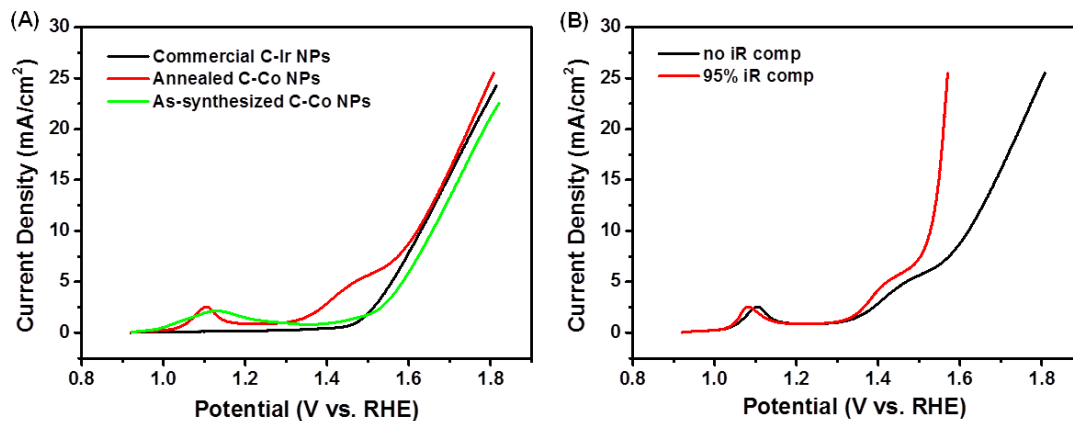
Figure 5-7. (A) Polarization curves of the annealed C-Co NPs, commercial C-Ir catalyst and as-synthesized C-Co NPs on GC electrode in 0.1 M KOH with a mass loading of 0.2 mg/cm^2. The measurements were performed at the scan rate of 10 mV/s and rotating speed of 1600 rpm. All polarization curves were collected without *iR*-correction. (B) Polarization curves of the annealed C-Co NP catalyst with and without *iR*-correction. The black curve is without iR-correction and the red curve is with 95% iR compensation. The uncompensated resistance R_u of our electrochemical cell was determined to be ~50 Ω by the current interrupt method (i-interrupt).

The stability of the annealed C-Co NPs and commercial C-Ir NPs was tested by using a chronoamperometric method at an overpotential of 0.4 V (**Figure 5-8**). After 1 h, the current density for the annealed C-Co NPs dropped 13% while the value from the C-Ir NPs decreased 45%. Even after 6 h test, the C-Co NPs still showed a slower rate of activity decrease than the commercial C-Ir, indicating that the annealed Co NPs are much more stable than the commercial Ir NPs.
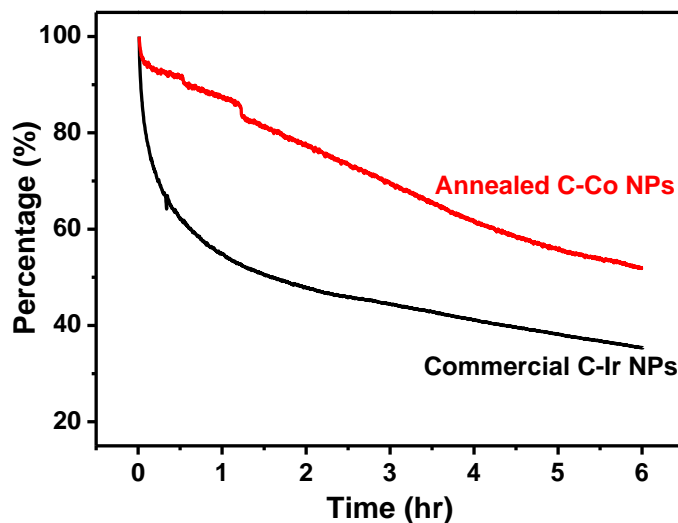
Figure 5-8. Chronoamperometric curves of the annealed C-Co NPs and commercial C-Ir catalyst on GC electrode at an overpotential of 0.4 V (1.63 V vs RHE) in 0.1 M KOH.

The NPs in the catalysts were further characterized after the stability test, as shown in the TEM images in **Figure 5-9**. The C-Ir NPs are aggregates/sintered while the C-NPs stay well dispersed on the carbon support, but have a core/shell structure due to surface oxidation of Co, which explains their slow activity drop over time. We should note that the oxidized Co can be readily reduced back to Co by the same reductive annealing described above and the C-Co catalyst can be re-generated and re-used for the OER.
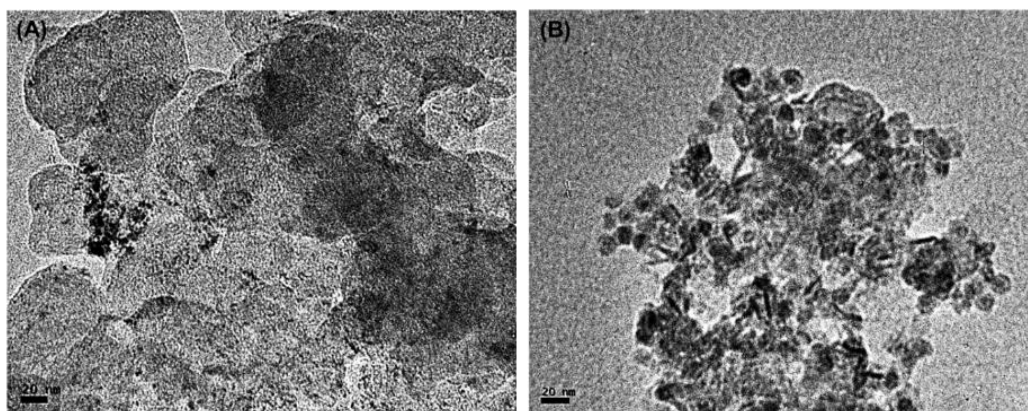
Figure 5-9. TEM images of (A) C-Ir NPs and (B) annealed C-Co NPs after stability test.

5.3.3. Metallic Core Effect on the Catalytic Activity

To confirm that the metallic core is indeed an important factor to enhance Co NP catalysis for the OER, we performed controlled oxidation of the Co NPs and studied the OER catalysis of the C-Co/CoO and C-CoO. After treating the annealed Co NPs in O_2 at 100 ^{o}C for 30 min, the morphology of the NPs was well maintained without any noticeable change (**Figure 5-10A**). HR-TEM image of a single NP in **Figure 5-10B** shows metallic Co core with amorphous oxide shell (thickness of ~1.5 nm). The catalyst after this O_2 treatment was denoted as C-Co/CoO NPs. XAS spectrum in total-electron-yield mode of the C-Co/CoO in **Figure 5-11** displays peak shift compared to metallic Co reference foil, further confirming the oxide formation.[51] When oxidized in O_2 at 150 ^{o}C for 12 h, the Co NPs were converted to hollow CoO NPs, as shown in **Figure 5-10C**. HR-TEM image of a representative CoO NP in **Figure 5-10D** shows the interfringe distance of 2.5 Å, corresponding to the lattice spacing of (111) planes of the fcc-CoO.
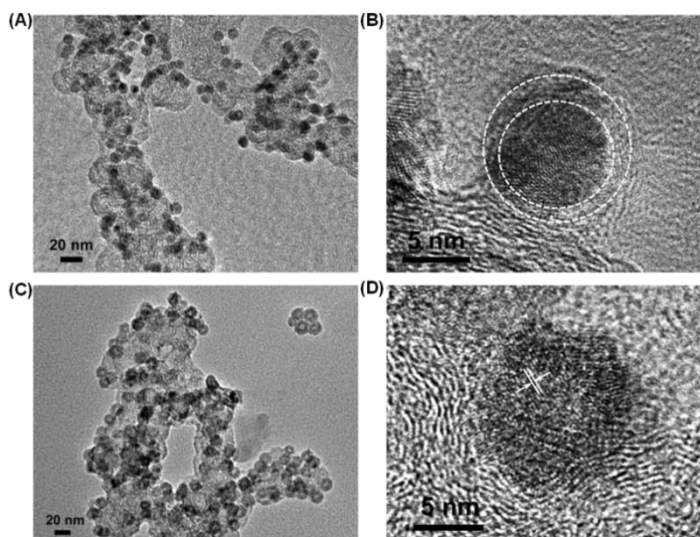
Figure 5-10. TEM image of C-Co/CoO NPs. (B) HR-TEM image of a Co/CoO core/shell NP on carbon support. (C) TEM image of C-CoO NPs. (D) HR-TEM images of a CoO NP on carbon support.
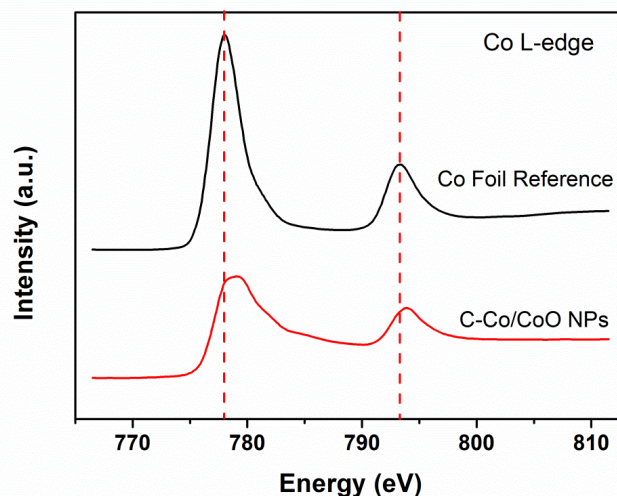
Figure 5-11. Ex-situ soft X-ray absorption spectra of Co L-edge of the Co reference foil and Co/CoO NPs by oxidizing the Co NPs in O_2 at 100 ^{o}C for 30 min. The measurement was performed in the total-electron-yield mode to make it sensitive to the surface of NPs.

The polarization curve of the C-Co/CoO NPs in **Figure 5-12A** exhibits an increase of the overpotential compared to the annealed C-Co NPs (0.43 V vs. 0.39 V at the current density of 10 mA/cm^2). For the CoO NPs, their overpotential is at 0.46 V, which is similar to recently reported Co$_x$O$_y$ NP catalysts.[31, 33] The OER data from the Co, Co/CoO and CoO NPs are summarized in **Figure 5-12B**. These results indicate that the metallic Co plays an important role in enhancing the OER activity. The formation of the thick CoO shell significantly degrades the catalytic performance due to the decrease in electron conductivity.
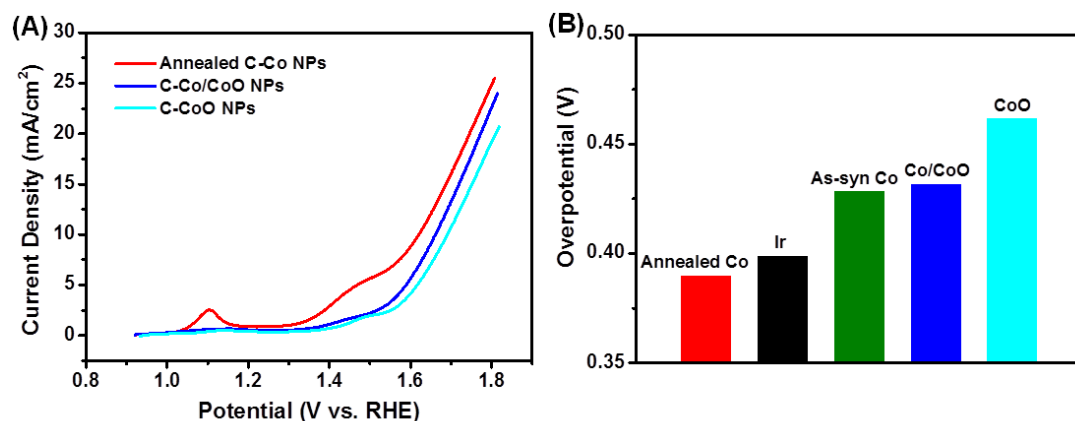
Figure 5-12. (A) Polarization curves of the annealed C-Co NPs, C-Co/CoO NPs and C-CoO NPs deposited on GC electrode in 0.1 M KOH at a mass loading of 0.2 mg/cm^2 without *iR*-correction. (B) Comparison of the overpotential for different catalysts at the current density of 10 mA/cm^2.

5.3.4. Monolayer Assembly of the Co NPs and Their OER Catalytic Activity

Previous studies have indicated that decreasing the thickness of the catalysts can increase the number of active sites and catalyst's TOF.[18, 26] Very recently, self-assembled monolayer or multilayer NP catalysts have been developed for enhanced activity.[52-54] To better evaluate the OER catalysis of the annealed Co NPs, we assembled the Co NPs into a monolayer array through a water-air interface self-assembly approach.[55-57] A monolayer array with the size of 0.6 cm $\times$ 0.7 cm was transferred onto a GC plate that would be used as a working electrode. This way, all Co NPs can be exposed to the reactants. Scanning electron microscopy (SEM) image of a representative area of the monolayer catalyst on the GC plate is shown in **Figure 5-13**. The assembly pattern is further confirmed by the TEM image of the monolayer array transferred on a carbon-coated copper grid (**Figure 5-14**). From the SEM and TEM images of the Co NP array, we estimate the Co NP packing density of ca. 4000 NPs/μm^2. The monolayer Co

NP array on GC plate was pre-annealed at 600°C as described and was used as a working electrode (Note: no NP aggregation was observed after the annealing treatment).
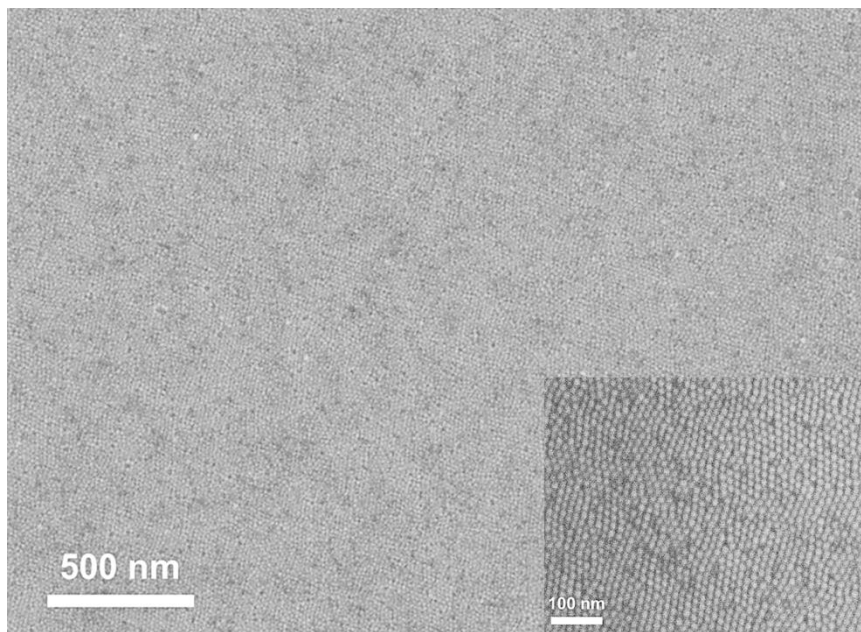
Figure 5-13. SEM images of the monolayer assembly of Co NPs on GC plate electrode. The inset is the SEM image of the assembly at higher magnification after reductive annealing.
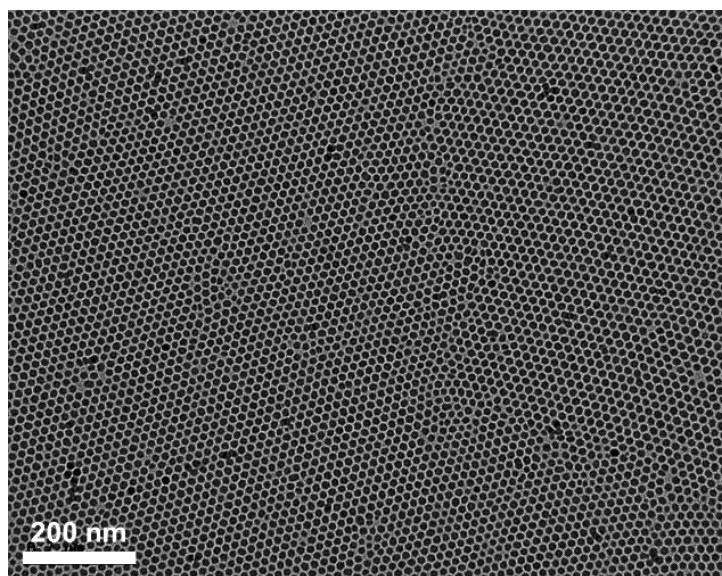
Figure 5-14. TEM image of the Co monolayer array.

After the reductive annealing, the Co NP monolayer catalyst was tested. Without Co

NPs, the bare GC plate is not active for OER; in contrast the Co monolayer catalyst

shows high OER activity (**Figure 5-15**). The TOFs were calculated by assuming that

each 10 nm Co NP has the fcc-structure and all the surface Co atoms are catalytically

active (see the Appendix for detailed calculation). **Figure 5-16A** shows the TOFs at an

overpotential of 0.4 V for the Co monolayer catalyst and the C-Co catalyst with different

mass loadings. For the catalyst with a mass loading of 84 $\mu g_{Co}/cm^2$ (C-Co catalyst at the

loading of 0.2 mg/cm^2 with 42 wt% Co), the TOF is 0.14 s^{-1}. However, by decreasing the

thickness of the catalyst to the monolayer level (1.1 $\mu g_{Co}/cm^2$), the TOF increases by

about 15 times to 2.13 s^{-1}. This TOF enhancement is in good agreement with previous

reports about the thickness effect on the TOFs.[18, 26] Moreover, the mass activity of the

monolayer catalyst was also calculated (**Figure 5-16B**). Compared to the C-Co NP

catalyst at a mass loading of 84 $\mu g_{Co}/cm^2$, the monolayer catalyst exhibits a dramatic

enhancement in mass activity by 15 times from 126 A/g to 1949 A/g. This value is also

much higher than that of the C-Ir catalyst (500 A/g). These results further suggest that

stabilized metallic Co NPs are promising catalyst for OER with catalyst efficiency

superior to the Ir catalyst.
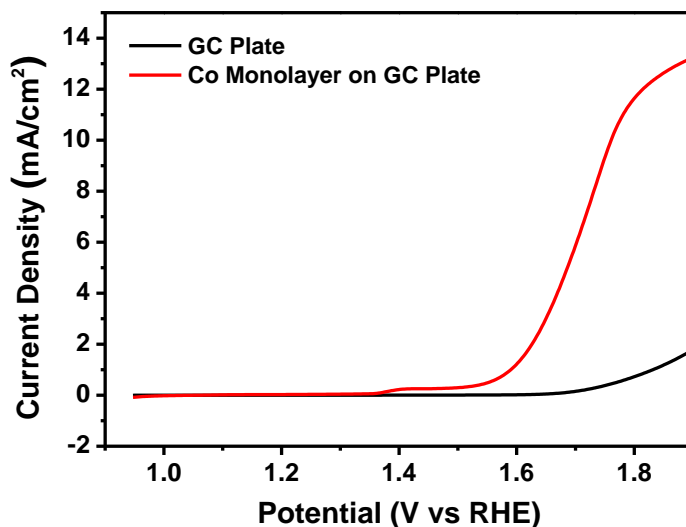
Figure 5-15. Polarization curves of the bare GC plate and the annealed Co NP monolayer catalyst on the GC plate at the scan rate of 10 mV/s in 0.1 M KOH.
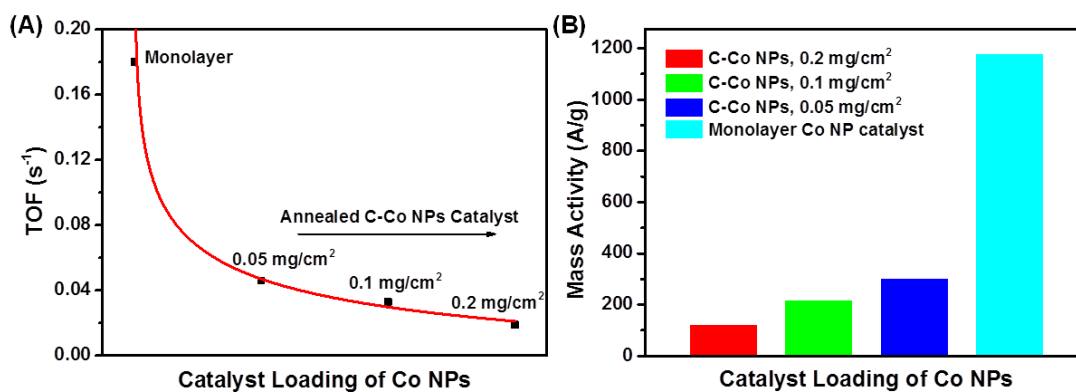
Figure 5-16. (A) TOFs and (B) mass activity of the annealed Co NP catalysts of different catalyst loadings at an overpotential of 0.4 V.

5.4. Conclusion

In summary, highly stable metallic Co NPs have been synthesized through a post reductive annealing process. These metallic Co NPs are more active and durable for OER than the commercial Ir catalyst. The high catalytic efficiency can be ascribed to better electron-conductivity of the metallic core. To better evaluate the intrinsic activity of the

metallic Co NPs, a monolayer array of Co NPs has been fabricated through Co NP self-assembly at water-air interface. The monolayer NP catalyst exhibits 15 times higher TOF and mass activity than the Co NPs deposited on conventional carbon support. With better activity and stability than the commercial Ir catalyst, these metallic Co NPs should serve as a promising noble-metal-free catalyst for efficient OER in alkaline media.

REFERENCES

[1] R. Subbaraman, D. Tripkovic, D. Strmcnik, K. C. Chang, M. Uchimura, A. P. Paulikas, V. Stamenkovic, N. M. Markovic, *Science* **2011**, *334*, 1256-1260.

[2] A. Kudo, Y. Miseki, *Chem. Soc. Rev.* **2009**, *38*, 253-278.

[3] M. G. Walter, E. L. Warren, J. R. McKone, S. W. Boettcher, Q. X. Mi, E. A. Santori, N. S. Lewis, *Chem. Rev.* **2010**, *110*, 6446-6473.

[4] M. Yagi, E. Tomita, T. Kuwabara, *J. Electroanal. Chem.* **2005**, *579*, 83-88.

[5] Y. H. Fang, Z. P. Liu, *J. Am. Chem. Soc.* **2010**, *132*, 18214-18222.

[6] Y. Lee, J. Suntivich, K. J. May, E. E. Perry, Y. Shao-Horn, *J. Phys. Chem. Lett.* **2012**, *3*, 399-404.

[7] H. G. S. Casalongue, M. L. Ng, S. Kaya, D. Friebel, H. Ogasawara, A. Nilsson, *Angew. Chem. Int. Ed.* **2014**, *53*, 7169-7172.

[8] N. D. Morris, M. Suzuki, T. E. Mallouk, *J. Phys. Chem. A* **2004**, *108*, 9115-9119.

[9] M. Yagi, E. Tomita, S. Sakita, T. Kuwabara, K. Nagai, *J. Phys. Chem. B* **2005**, *109*, 21489-21491.

[10] H. N. Nong, H. S. Oh, T. Reier, E. Willinger, M. G. Willinger, V. Petkov, D. Teschner, P. Strasser, *Angew. Chem. Int. Ed.* **2015**, *54*, 2975-2979.

[11] Y. Gorlin, T. F. Jaramillo, *J. Am. Chem. Soc.* **2010**, *132*, 13612-13614.

[12] D. C. Hong, Y. Yamada, T. Nagatomi, Y. Takai, S. Fukuzumi, *J. Am. Chem. Soc.* **2012**, *134*, 19572-19575.

[13] R. Subbaraman, D. Tripkovic, K. C. Chang, D. Strmcnik, A. P. Paulikas, P. Hirunsit, M. Chan, J. Greeley, V. Stamenkovic, N. M. Markovic, *Nat. Mater.* **2012**, *11*, 550-557.

[14]   M. Gong, Y. Li, H. Wang, Y. Liang, J. Z. Wu, J. Zhou, J. Wang, T. Regier, F. Wei, H. Dai, *J. Am. Chem. Soc.* **2013**, *135*, 8452-8455.

[15]   Y. Gorlin, B. Lassalle-Kaiser, J. D. Benck, S. Gul, S. M. Webb, V. K. Yachandra, J. Yano, T. F. Jaramillo, *J. Am. Chem. Soc.* **2013**, *135*, 8525-8534.

[16]   M. R. Gao, W. C. Sheng, Z. B. Zhuang, Q. R. Fang, S. Gu, J. Jiang, Y. S. Yan, *J. Am. Chem. Soc.* **2014**, *136*, 7077-7084.

[17]   X. Long, J. K. Li, S. Xiao, K. Y. Yan, Z. L. Wang, H. N. Chen, S. H. Yang, *Angew. Chem. Int. Ed.* **2014**, *53*, 7584-7588.

[18]   L. Trotochaud, S. L. Young, J. K. Ranney, S. W. Boettcher, *J. Am. Chem. Soc.* **2014**, *136*, 6744-6753.

[19]   M. J. Kenney, M. Gong, Y. G. Li, J. Z. Wu, J. Feng, M. Lanza, H. J. Dai, *Science* **2013**, *342*, 836-840.

[20]   L. Kuai, J. Geng, C. Y. Chen, E. J. Kan, Y. D. Liu, Q. Wang, B. Y. Geng, *Angew. Chem. Int. Ed.* **2014**, *53*, 7547-7551.

[21]   M. R. Gao, Y. F. Xu, J. Jiang, Y. R. Zheng, S. H. Yu, *J. Am. Chem. Soc.* **2012**, *134*, 2930-2933.

[22]   V. Artero, M. Chavarot-Kerlidou, M. Fontecave, *Angew. Chem. Int. Ed.* **2011**, *50*, 7238-7266.

[23]   D. K. Dogutan, R. McGuire, Jr., D. G. Nocera, *J. Am. Chem. Soc.* **2011**, *133*, 9178-9180.

[24]   Y. Surendranath, D. A. Lutterman, Y. Liu, D. G. Nocera, *J. Am. Chem. Soc.* **2012**, *134*, 6326-6336.

[25]   M. W. Kanan, D. G. Nocera, *Science* **2008**, *321*, 1072-1075.

[26]   B. S. Yeo, A. T. Bell, *J. Am. Chem. Soc.* **2011**, *133*, 5587-5593.

[27]   L. Trotochaud, J. K. Ranney, K. N. Williams, S. W. Boettcher, *J. Am. Chem. Soc.* **2012**, *134*, 17253-17261.

[28]   R. D. Smith, M. S. Prevot, R. D. Fagan, S. Trudel, C. P. Berlinguette, *J. Am. Chem. Soc.* **2013**, *135*, 11580-11586.

[29]   M. Bajdich, M. Garcia-Mota, A. Vojvodic, J. K. Norskov, A. T. Bell, *J. Am. Chem. Soc.* **2013**, *135*, 13521-13530.

[30]   N. H. Chou, P. N. Ross, A. T. Bell, T. D. Tilley, *ChemSusChem* **2011**, *4*, 1566-1569.

[31]   J. Masa, W. Xia, I. Sinev, A. Q. Zhao, Z. Y. Sun, S. Grutzke, P. Weide, M. Muhler, W. Schuhmann, *Angew. Chem. Int. Ed.* **2014**, *53*, 8508-8512.

[32]   M. Zhang, M. de Respinis, H. Frei, *Nat. Chem.* **2014**, *6*, 362-367.

[33]   A. Q. Zhao, J. Masa, W. Xia, A. Maljusch, M. G. Willinger, G. Clavel, K. P. Xie, R. Schlogl, W. Schuhmann, M. Muhlert, *J. Am. Chem. Soc.* **2014**, *136*, 7551-7554.

[34]   J. Rosen, G. S. Hutchings, F. Jiao, *J. Am. Chem. Soc.* **2013**, *135*, 4516-4521.

[35]   Z. B. Zhuang, W. C. Sheng, Y. S. Yan, *Adv. Mater.* **2014**, *26*, 3950-3955.

[36]   T. Y. Ma, S. Dai, M. Jaroniec, S. Z. Qiao, *J. Am. Chem. Soc.* **2014**, *136*, 13925-13931.

[37]   L. B. Liao, Q. H. Zhang, Z. H. Su, Z. Z. Zhao, Y. N. Wang, Y. Li, X. X. Lu, D. G. Wei, G. Y. Feng, Q. K. Yu, X. J. Cai, J. M. Zhao, Z. F. Ren, H. Fang, F. Robles-Hernandez, S. Baldelli, J. M. Bao, *Nat. Nanotechnol.* **2014**, *9*, 69-73.

[38]   F. Jiao, H. Frei, *Angew. Chem. Int. Ed.* **2009**, *48*, 1841-1844.

[39]   A. J. Esswein, M. J. McMurdo, P. N. Ross, A. T. Bell, T. D. Tilley, *J. Phys. Chem. C* **2009**, *113*, 15068-15072.

[40]   X. Zou, A. Goswami, T. Asefa, *J Am Chem Soc* **2013**, *135*, 17242-17245.

[41]   Y. Zhang, B. Cui, C. S. Zhao, H. Lin, J. B. Li, *Phys Chem Chem Phys* **2013**, *15*, 7363-7369.

[42]   F. Song, X. L. Hu, *J. Am. Chem. Soc.* **2014**, *136*, 16481-16484.

[43]   Z. Y. Lu, H. T. Wang, D. S. Kong, K. Yan, P. C. Hsu, G. Y. Zheng, H. B. Yao, Z. Liang, X. M. Sun, Y. Cui, *Nat. Commun.* **2014**, *5*, 4345.

[44]   Y. Gorlin, C. J. Chung, J. D. Benck, D. Nordlund, L. Seitz, T. C. Weng, D. Sokaras, B. M. Clemens, T. F. Jaramillo, *J. Am. Chem. Soc.* **2014**, *136*, 4920-4926.

[45]   V. Viswanathan, K. L. Pickrahn, A. C. Luntz, S. F. Bent, J. K. Norskov, *Nano Lett.* **2014**, *14*, 5853-5857.

[46]   S. Peng, J. Xie, S. H. Sun, *J. Solid State Chem.* **2008**, *181*, 1560-1564.

[47]   S. Guo, S. Zhang, L. Wu, S. Sun, *Angew. Chem. Int. Ed.* **2012**, *51*, 11770-11773.

[48]   L. M. Lacroix, N. F. Huls, D. Ho, X. L. Sun, K. Cheng, S. H. Sun, *Nano Lett.* **2011**, *11*, 1641-1645.

[49]   S. Zhang, G. Jiang, G. T. Filsinger, L. Wu, H. Zhu, J. Lee, Z. Wu, S. Sun, *Nanoscale* **2014**, *6*, 4852-4856.

[50]   C. C. McCrory, S. Jung, J. C. Peters, T. F. Jaramillo, *J. Am. Chem. Soc.* **2013**, *135*, 16977-16987.

[51]   A. Tuxen, S. Carenco, M. Chintapalli, C. H. Chuang, C. Escudero, E. Pach, P. Jiang, F. Borondics, B. Beberwyck, A. P. Alivisatos, G. Thornton, W. F. Pong, J.

H. Guo, R. Perez, F. Besenbacher, M. Salmeron, *J. Am. Chem. Soc.* **2013**, *135*, 2273-2278.

[52]   Y. J. Kang, X. C. Ye, J. Chen, Y. Cai, R. E. Diaz, R. R. Adzic, E. A. Stach, C. B. Murray, *J. Am. Chem. Soc.* **2013**, *135*, 42-45.

[53]   Y. Yamada, C. K. Tsung, W. Huang, Z. Y. Huo, S. E. Habas, T. Soejima, C. E. Aliaga, G. A. Somorjai, P. D. Yang, *Nat. Chem.* **2011**, *3*, 372-376.

[54]   D. Kim, J. Resasco, Y. Yu, A. M. Asiri, P. D. Yang, *Nat. Commun.* **2014**, *5*, 4948

[55]   A. G. Dong, J. Chen, P. M. Vora, J. M. Kikkawa, C. B. Murray, *Nature* **2010**, *466*, 474-477.

[56]   T. Wen, S. A. Majetich, *ACS Nano* **2011**, *5*, 8868-8876.

[57]   L. Wu, P. O. Jubert, D. Berman, W. Imaino, A. Nelson, H. Zhu, S. Zhang, S. Sun, *Nano Lett.* **2014**, *14*, 3395-3399.

APPENDIX: Calculation of the Turnover Frequency and Mass Activity

The TOF value is calculated as following:

$$TOF = \frac{jS}{4nF}$$

Here, j is the measured current density (mA/cm^2), S is the surface area of the GC electrode (0.196 cm^2 for the GC disk electrode and 0.42 cm^2 for the GC plate electrode for the monolayer measurement), n is the moles of active materials deposited on the electrode, F is the Faraday constant (96485 C/mol).

We assume that all the surface metal atoms are involved in the electrocatalysis. The surface atom percentage of the face-centered cubic (fcc) Co NPs is determined using previously reported model for fcc NPs (Owens, F. J.; Poole, C. P., *The Physics and Chemistry of Nanosolids*. Wiley, 2008): The diameter of a fcc metallic NPs is illustrated in this equation:

$$d = \frac{(2n_o - 1)a}{\sqrt{2}}$$

Here n_o is the layers of atoms, a is the unit constant of fcc-Co (a = 3.5447 Å). The size of our fcc-Co NPs is 10 nm, so n_o is calculated to be n_o = 21.

Total metal atoms (N) of a 10 nm NP:

$$N = \frac{1}{3}(10n_o{}^3 - 15n_o{}^2 + 11n_o - 3) = 28741$$

Surface metal atoms (N_{surf}) of a 10 nm NP:

$$N_{surf} = 10n_o{}^2 - 20n_o + 12 = 4002$$

Percentage of atoms on the surface of 10 nm Co NPs:

$$\frac{4002}{28741} \times 100\,\% = 14\,\%$$

TOF and mass activity of the annealed C-Co NPs at the mass loading of 0.2 mg/cm²:

At the overpotential of 0.4 V, j = 10.63 mA/cm²

m(Co) = 0.2 mg/cm² × 0.196 cm² × 0.42 = 1.65 × 10⁻⁵ g

Moles of surface active Co atoms:

$$n(Co) = \frac{1.65 \times 10^{-5}}{58.933}\ mol \times 14\,\% = 3.92 \times 10^{-8}\ mol$$

$$TOF = \frac{10.63 \times 0.196\ mA}{4 \times 3.92 \times 10^{-8} \times 96485\ C} = 0.14\ s^{-1}$$

$$Mass\ activity = \frac{10.63 \times 0.196\ mA}{1.65 \times 10^{-5}\ g} = 126\ A\ g^{-1}$$

TOF and mass activity of the monolayer of Co NPs:

The mass of each NP can be calculated:

$$m\ (NP) = \frac{28741}{6.022 \times 10^{23}} \times 58.933\ g = 2.81 \times 10^{-18} g$$

The monolayer assembly has a packing density of 4000 NPs/μm^2 (4×10^{11} NPs/cm^2), the area of the monolayer catalyst is 0.42 cm^2, and thus the total mass of Co in the monolayer is estimated to be:

$$M = 0.42 \times 4 \times 10^{11} \times 2.81 \times 10^{-18}\,g = 4.72 \times 10^{-7}\,g$$

Co mass loading in the monolayer catalyst:

$$\text{Mass loading} = \frac{4.72 \times 10^{-7}\,g_{Co}}{0.42\,cm^2} = 1.12\,ug_{Co}/cm^2$$

Moles of surface active Co atoms in the monolayer catalyst:

$$n(\text{Co}) = \frac{4.72 \times 10^{-7}}{58.933}\,mol \times 14\,\% = 1.12 \times 10^{-9}\,mol$$

The current density is 2.19 mA/cm^2 at the overpotential of 0.4 V, so the TOF for the monolayer catalyst is:

$$\text{TOF} = \frac{2.19 \times 0.42\,\text{mA}}{4 \times 1.12 \times 10^{-9} \times 96485\,C} = 2.13\,s^{-1}$$

$$\text{Mass activity} = \frac{2.19 \times 0.42\,\text{mA}}{4.72 \times 10^{-7}\,g} = 1949\,A\,g^{-1}$$

Chapter 6. New Approach to Fully-Ordered fct-FePt

Nanoparticles for Much Enhanced Electrocatalysis in Acid

6.1. Introduction

Developing highly efficient catalysts for oxygen reduction reaction (ORR) and hydrogen evolution reaction (HER) in acid media is crucial for promoting electrochemical energy conversion in fuel cells and for facile production of clean fuel, hydrogen, *via* water splitting. Nanostructured platinum (Pt), especially Pt nanoparticles (NPs), have been selected either as a model system for understanding electrochemical reduction mechanism or as a practical catalyst to achieve high-enough energy conversion efficiency in electrochemical devices. Recent studies have been focusing heavily on Pt-based alloy NPs, hoping to further enhance Pt catalysis and to lower Pt loadings. As a result, these alloy NPs can now be synthesized with the desired dimension controls and their catalytic activities are tuned not only by NP sizes/compositions/shapes,[1-8] but also by the core/shell structure in which Pt alloys serve as a shell.[9-15] Alternatively, a Pt-catalyst can be embedded in an ionic liquid medium to improve its ORR catalysis.[3, 16] Despite this progress, there is still no definite answer on what form of the catalyst can yield maximal activity with much improved durability in the acidic electrochemical reduction conditions.

In the efforts of searching for the most active form of Pt, a new strategy of controlling Pt alloy structure attracts much attention. For example, the FePt alloy NPs prepared for ORR studies often have a solid solution structure in which Fe and Pt occupy randomly the face-centered cubic (fcc) lattice. For notation convenience, these NPs are referred to as fcc-FePt NPs. With the proper composition control, the fcc structure can be converted to chemically ordered face-centered tetragonal (fct) structure. Earlier studies have indicated that the fct-FePt is not only magnetically hard,[17] but also chemically robust

against Fe leaching in acid[18] and catalytically more active for ORR than the fcc-FePt.[18-19] This structure-induced catalytic enhancement is also observed in CoPt[20] and CuPt[21] NP systems. In general, high temperature annealing (>500 ℃) is required to convert the fcc structure to the fct one, which causes NP to aggregate/sinter.[22-23] Although NPs coated with a layer of robust oxide (such as MgO[18, 24] and SiO$_2$[25-26]) or supported on carbon can be stabilized against aggregation/sintering, the protection also limits atom mobility within the NP structure, making it more difficult for structure transformation from fcc to fct. As a result, partially ordered fct-FePt NPs are often obtained and studied,[18, 27] compromising the benefit of fct-structure effect on ORR. In this chapter, we report a new strategy to improve fcc-fct transition and demonstrate that the increase in fct-ordering in the FePt structure is indeed an effective way of enhancing NP catalytic efficiency for electrochemical reduction reactions - the fully ordered fct-FePt NPs serve as a robust catalyst for both ORR and HER.

The new strategy applied to the synthesis of FePt NPs with increased Fe, Pt ordering is illustrated in **Figure 6-1**. In this new synthesis, the dumbbell-like fcc-FePt-Fe$_3$O$_4$ NPs were firstly prepared by controlled decomposition of iron pentacarbonyl (Fe(CO)$_5$) and reduction of platinum acetylacetonate (Pt(acac)$_2$) at temperatures 220 ℃ and 300 ℃. Here, 220 ℃ heating was used to form Pt-rich fcc-FePt NPs and 300 ℃ was for more Fe growth on the fcc-FePt. Upon air oxidation, dumbbell fcc-FePt-Fe$_3$O$_4$ NPs were obtained. In the process, the amount of Fe(CO)$_5$ was optimized so that the Fe/Pt composition in the as-synthesized dumbbell fcc-FePt-Fe$_3$O$_4$ NPs was at 52/48, as analyzed by inductively coupled plasma-atomic emission spectroscopy (ICP-AES), to facilitate fcc-fct transition.[17] The dumbbell NPs were then coated with MgO through thermal

decomposition of magnesium (II) acetylacetonate in the presence of 1,2-tetradecanediol, oleic acid and oleylamine in benzyl ether at 300 ℃. The fcc-FePt-Fe$_3$O$_4$/MgO NPs were then annealed at 700 ℃ under Ar + 5% H$_2$ to reduce Fe$_3$O$_4$ into Fe (to create O-vacancies) and to promote Fe, Pt diffusion into fully-ordered fct-structure within the MgO enclosure. The MgO coating was removed by diluted nitric acid washing and the fct-FePt NPs were dispersed in ethanol and deposited on Ketjen carbon for further studies.
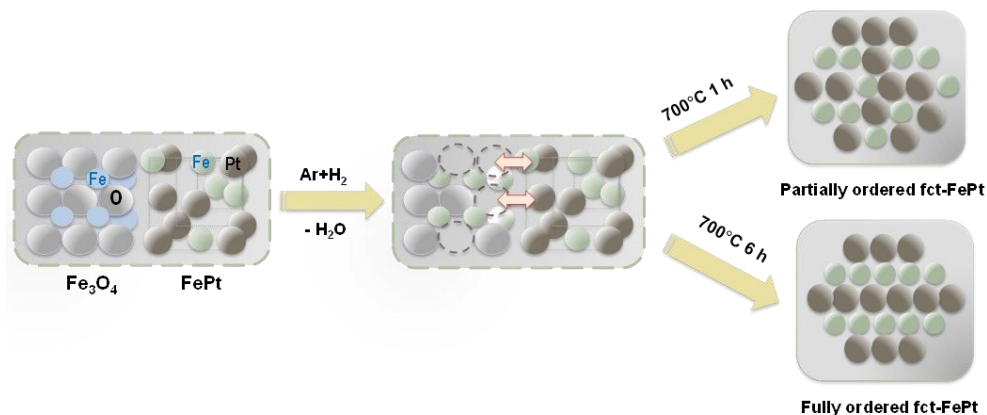
Figure 6-1. Schematic illustration of the formation of fct-FePt NPs via reductive annealing of the dumbbell FePt-Fe$_3$O$_4$ NPs embedded in MgO matrix.

6.2. Experimental Section

Chemicals and Materials: Pt(acac)$_2$ (98%), Mg(acac)$_2$ (anhydrous, 98%) (acac = aceylacetonate) were purchased from Strem Chemicals. Oleylamine (70%), oleic acid (90%), 1-octadecene (90%), benzyle ether (98%), Fe(CO)$_5$, 1,2-tetradecanediol (90%) and Nafion (5% in a mixture of lower aliphatic alcohols and water) were purchased from Sigma-Aldrich. All chemicals were used without further purification. The commercial Pt catalyst (20% mass loading on carbon, Pt particle diameter at 2.5-3.5 nm) was obtained from Fuel Cell Store.

Characterization: X-ray diffraction (XRD) patterns of the NPs were collected on a Bruker AXS D8-Advanced diffractometer with Cu Kα radiation (λ = 1.5418 Å). Transmission electron microscopy (TEM) images were acquired from a Philips CM20 operating at 200 kV. High-resolution TEM (HR-TEM) images were recorded using a JEOL 2010 with an accelerating voltage of 200 kV. TEM and HR-TEM samples were prepared by depositing a single drop of diluted NPs dispersion on amorphous carbon-coated copper grids. Scanning transmission electron microscopy (STEM) analyses were carried out on a Hitachi HD2700C (200 kV) with a probe aberration corrector, at the Center for Functional Nanomaterials, Brookhaven National Lab. The electron energy loss spectroscopy (EELS) line-scan was obtained by a high-resolution Gatan-Enfina ER with a probe size of 1.3 Å. A power law function was used for EELS background subtraction. Magnetic studies were performed on a Quantum Design Superconducting Quantum Interface Device (SQUID) with a field up to 70 kOe. The inductively coupled plasma-atomic emission spectroscopy (ICP-AES) measurements were carried on a JY2000 Ultrace ICP atomic emission spectrometer equipped with a JY AS 421 autosampler and 2400g/mm holographic grating.

Synthesis of dumbbell fcc-FePt-Fe$_3$O$_4$ NPs: In a four-neck flask, a mixture of 0.1g Pt(acac)$_2$, 0.7 mL oleylamine, 0.65 mL oleic acid and 5 mL 1-octadecene was stirred and degassed at 120 ℃ under an Ar atmosphere for 30 min. Under a blanket of Ar, Fe(CO)$_5$ (0.05 mL) was injected into the mixture solution. Subsequently, the temperature was raised to 220 ℃ at a rate of 5 ℃/min and kept at this temperature for 30 min. Then the mixture was heated to 300 ℃ at a rate of 10 ℃/min and maintained at this temperature for 10 min before cooled down to room temperature. The product was precipitated by 2-

propanol and collected by centrifugation (8500 rpm, 8 min). The product was redispersed in hexane and separated by adding ethanol and centrifugation (8500 rpm, 8 min). The final product was dispersed in hexane for further use.

Synthesis of FePt-Fe₃O₄/MgO and fct-FePt/MgO NPs: A mixture of 0.4 g Mg(acac)$_2$, 0.42 g 1,2-tetradecanediol, 0.9 mL oleylamine, 0.6 mL oleic acid was dissolved in 18 mL benzyl ether under vigorously stirring and degassed at 120 ℃. 60 mg of the as-synthesized fcc-FePt-Fe$_3$O$_4$ NPs dispersed in 5 mL of hexane was added into the flask. The mixture was kept degassed for 20 min to remove hexane. Then under the blanket of Ar, the solution was heated up to 300 ℃ and maintained at this temperature for 60 min before cooled down to room temperature. The product was precipitated with ethanol, centrifuged (8500 rpm, 8 min) and dried. After annealing at 700 ℃ under Ar + 5%H$_2$, fct-FePt/MgO NPs were obtained.

Synthesis of carbon supported fct-FePt (C-fct-FePt) NPs: To prepare C-fct-FePt NPs, 20 mg of fct-FePt/MgO was dispersed in 20 mL ethanol under ultrasonication, and 0.6 mL of concentrated HNO$_3$ was then added dropwise into the dispersion. The solution was sonicated for 5 min and 10 mg Ketjen carbon power was added. The mixture was kept sonicated for 1 h. Then the C-fct-FePt NPs were separated by centrifugation and washed with ethanol and DI water. The NP/C weight ratio is ~1/2 measured by ICP-AES.

Synthesis of fcc-FePt NPs and C-fcc-FePt catalyst: In a four-neck flask, a mixture of 0.1 g Pt(acac)$_2$, 0.7 mL oleylamine, 0.65 mL oleic acid, and 5 mL 1-octadecene, was stirred and degassed at 120 ℃ under an Ar atmosphere for 30 min. Under a blanket of Ar, 0.09 mL Fe(CO)$_5$ was injected into the mixture solution. Subsequently, the temperature

was raised to 220 ℃ at a rate of about 5 ℃/min and kept at this temperature for 1 h before it was cooled to room temperature. The product was precipitated by 2-propanol and collected by centrifugation (8500 rpm, 8 min). The product was redispersed in hexane and separated by adding ethanol and centrifugation (8500 rpm, 8 min). The final product was dispersed in hexane for further use. ICP-AES measurement confirmed the molar ratio of Fe/Pt to be 50/50. To load the NPs on carbon, the as-synthesized fcc-FePt NPs and Ketjen-300J carbon at a weight ratio of 1:2 were mixed in 20 mL of hexane and 10 mL of isopropanol and sonicated for 1 h. The product was separated by centrifugation. The C-fcc-FePt were dried under ambient conditions and annealed at 400 ℃ for 1 h in a gas flow of Ar + 5% H_2 to remove the surfactant.

Electrochemical Measurements: Electrochemical measurements were performed on an Autolab 302 potentiostat with glassy carbon rotating disk (5 mm in diameter) as a working electrode, Ag/AgCl (4 M KCl) as a reference electrode, and platinum wire as a counter electrode. The potential difference between Ag/AgCl and RHE was measured in H_2 saturated 0.1 M $HClO_4$ electrolyte and the value is 0.260 ± 0.001 V. All potentials were later converted to the RHE scale. All catalysts were dispersed in a mixture containing water, isopropanol, and Nafion (5%) (v/v/v 4:1:0.05) to form a 2 mg/mL ink. 20 μL of catalyst ink was casted on the newly polished glassy carbon electrode and dried at ambient condition. The Pt loadings of fully-ordered fct-FePt, partially-ordered fct-FePt, fcc-FePt and commercial Pt were calculated to be 45.5, 47.1, 37.6 and 40 $\mu g_{Pt}/cm^2$, respectively. The catalysts were first subject to cyclic voltammetry (CV) scans between 0.05 and 1.3 V at 100 mV/s in N_2-saturated 0.1 M $HClO_4$ until a stable CV was obtained. The electrochemically active surface area (ECASA) was calculated by measuring the

charge collected in the hydrogen adsorption/desorption regions after double-layer correction, assuming a value of 210 mC/cm^2 for the adsorption of a hydrogen monolayer on polycrystalline Pt. ORR polarization curves were recorded by linear-sweep voltammetry (LSV) at a scan rate of 10 mV/s in O_2-saturated 0.1 M $HClO_4$ with the GC-RDE rotating at 1600 rpm. The kinetic current was calculated from the ORR polarization curve according to the Koutecky–Levich equation. Accelerated durability tests (ADT) of the catalysts for ORR were conducted by cycling the potential between 0.6 and 1.0 V at 100 mV/s. To evaluate the production of H_2O_2 of fct-FePt during the ORR, rotating ring/disk electrode (RRDE) experiments were carried out with the ring potential setting to 1.2 V. The four-electron selectivity of catalysts was evaluated based on the H_2O_2 yield, calculated from the following equation:

$$H_2O_2(\%) = 200 \times \frac{I_R/N}{(I_R/N) + I_D}$$

Here, I_D and I_R are the disk and ring currents, respectively, and N is the ring collection efficiency (~37%) provided by the manufacturer based on the geometry of the electrodes.

HER polarization curves were recorded by LSV at a scan rate of 2 mV/s in O_2-saturated 0.5 M H_2SO_4 without electrode rotation. Durability of catalysts for HER was conducted by cycling the potential between -0.3 and 0.9 V at 100 mV/s.

MEA Preparation and Fuel Cell Testing: The membrane electrode assemblies (MEAs) were fabricated using Nafion® 212 membrane in an acid form and catalyst inks. 20% C-Pt (E-TEK) and fully-ordered fct-FePt NPs were used as cathode catalysts. Anode catalysts of all the studied cells were 20% C-Pt. The inks were prepared by ultrasonically

mixing appropriate amounts of catalyst powders with de-ionized water (Millipore, 18 MΩ cm) and 5% Nafion® suspension (Ion Power, Inc.) for 90 seconds. Subsequently, the inks were brush-painted onto the membrane at 75 °C and dried for 30 min. The catalyst loadings were 0.2 mg_{Pt}/cm^2 for all the catalysts tested. The active cell area was 5 cm^2. H_2-air fuel cell testing was carried out in a single cell using a commercial fuel cell test system (Fuel Cell Technologies Inc.). The MEA was sandwiched between two graphite plates with single-serpentine flow channels machined in them. The cell was operated at 80 °C. Pure hydrogen and air, humidified at 85 °C, were supplied to the anode and cathode at a flow rate of 200 and 500 standard cubic centimeters per minute (sccm), respectively. Both electrodes were maintained at the same absolute pressure of 2.8 bar.

6.3. Results and Discussion

6.3.1. Synthesis of Fully Ordered fct-FePt Nanoparticles

Uniform dumbbell FePt-Fe_3O_4 NPs were synthesized. TEM image of the as-synthesized dumbbell FePt-Fe_3O_4 NPs is shown in **Figure 6-2A**, which have an average size of 8.0 (± 0.6)-3.9 (± 0.3) nm. HR-TEM image of a typical NP in **Figure 6-2B** exhibits a lattice fringe spacing at 0.19 nm in the black FePt NP and at 0.30 nm in the grey Fe_3O_4 NP, corresponding to the lattice planes of fcc-FePt (200) and fcc-Fe_3O_4 (220), respectively. X-ray diffraction (XRD) patterns of the as-synthesized FePt-Fe_3O_4 NPs powder were collected, as shown in **Figure 6-3**. The as-synthesized FePt-Fe_3O_4 shows typical fcc diffraction pattern of the FePt NPs and Fe_3O_4 NPs.
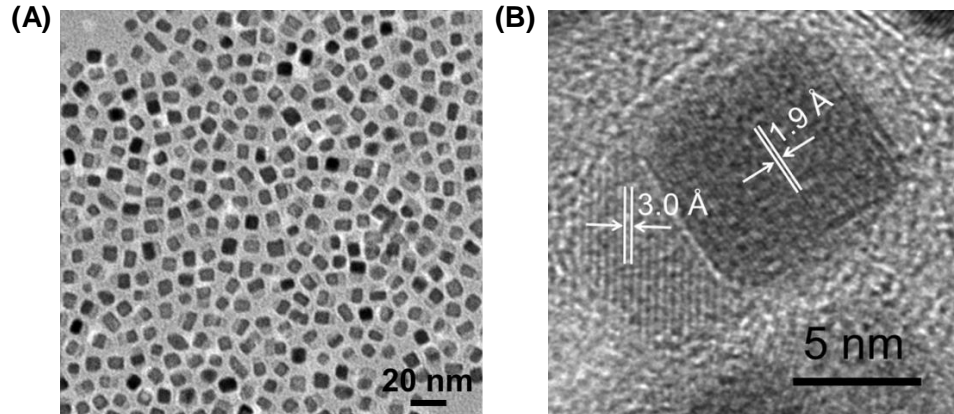
Figure 6-2. (A) TEM image and (B) HR-TEM image of the as-synthesized dumbbell fcc-FePt-Fe_3O_4 NPs.
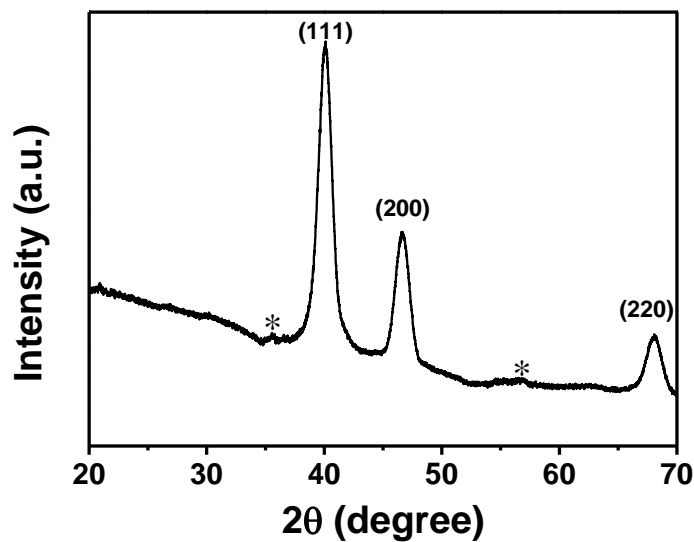
Figure 6-3. XRD pattern of the as-synthesized dumbbell fcc-FePt-Fe_3O_4 NPs. Due to the small size of Fe_3O_4, the diffraction peaks of Fe_3O_4 are much weaker compared to the strong diffraction peaks of fcc-FePt. * denotes the weak diffraction peaks of Fe_3O_4.

In order to prevent the aggregation/sintering of those NPs during heating treatment for the phase conversion, MgO shell was uniformly coated on each NP. TEM image of the fcc-FePt-Fe_3O_4/MgO NPs (**Figure 6-4A**) shows that all NPs are covered by the MgO shell. Thanks to this protection, the FePt NPs show no aggregation/sintering after

139

annealing at 700 °C for 1h and 6 h (**Figure 6-4B** and **Figure 6-4C**). The average size of the annealed FePt NPs after removing the MgO matrix by acid wash was measured to be 8.8 ±0.5 nm. **Figure 6-4D** shows the HR-TEM image of a typical annealed FePt NP after acid wash, with the lattice spacing of 0.24 nm, corresponding to (111) plane of fct-FePt. The detailed structure analysis will be discussed later.
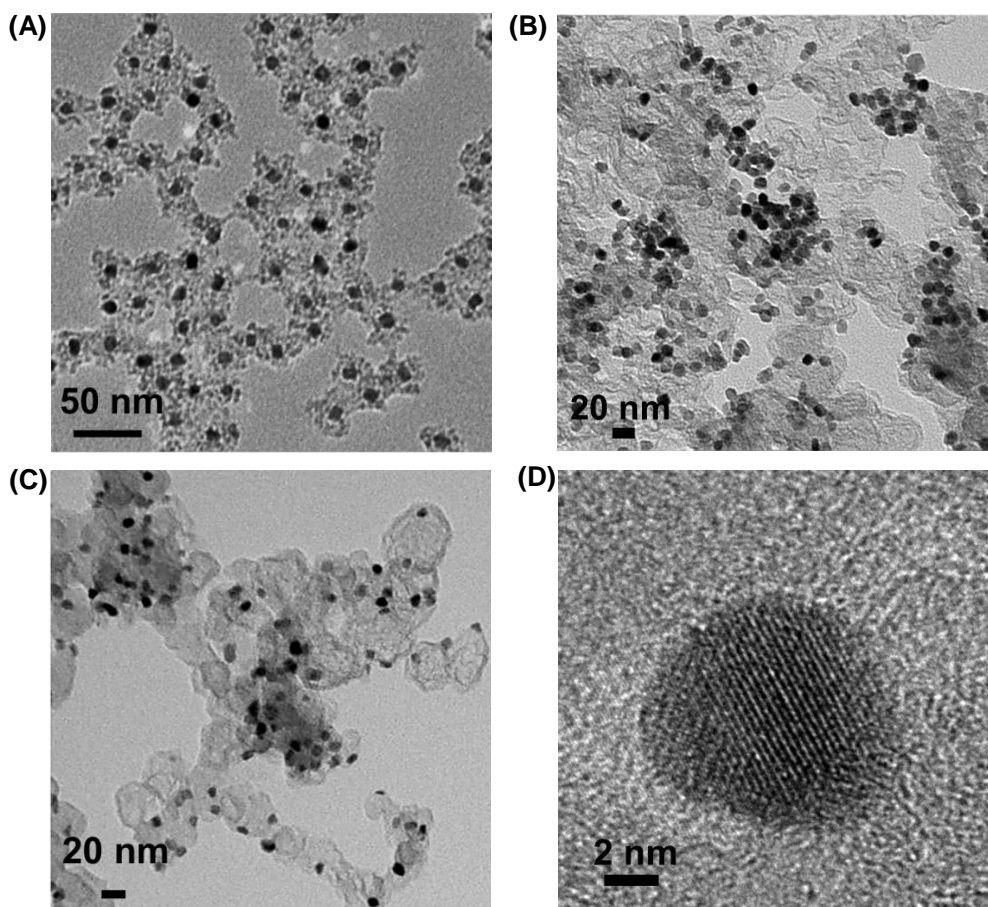
Figure 6-4. TEM images of (A) fcc-FePt-Fe$_3$O$_4$/MgO NPs. (B) the obtained fct-FePt NPs (thermal annealing at 700 °C under Ar + 5% H$_2$ for 1 h and acid wash to remove MgO) deposited on Ketjen carbon support. (C) the obtained fct-FePt (thermal annealing at 700 °C under Ar + 5% H$_2$ for 6 h and acid wash to remove MgO) deposited on Ketjen carbon support. (D) HR-TEM image of a typical fct-FePt NP.

X-ray diffraction (XRD) patterns of the fct-FePt NPs were collected to characterize structure transition from fcc to fct upon thermal annealing. **Figure 6-5** shows the XRD patterns of the fct-FePt NPs after removing the MgO coating. After annealing in Ar + 5% H_2 at $700^{\circ}C$ for 1 h, the FePt NPs show the (001)/(110) peaks that are associated with the fct structure. The Fe, Pt ordering in the fct-structure is further improved by increasing the annealing time to 6 h, as indicated by much more visible (001)/(110) peaks.
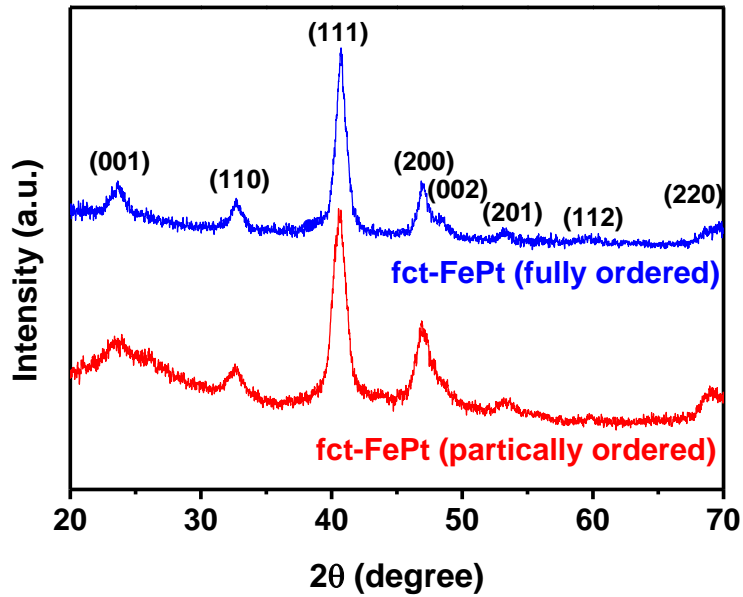
Figure 6-5. XRD patterns of the fct-FePt NPs after different annealing time. The pattern in red represents the fct-FePt NPs after annealing at 700 $^{\circ}$C for 1 h and the pattern in blue represents the fct-FePt NPs after annealing at 700 $^{\circ}$C for 6 h.

This fcc-fct structure transition is further supported by magnetic measurements. Different from the fcc-FePt NPs that are superparamagnetic at room temperature, the fct-FePt, due to the strong d electron interaction between Fe and Pt in the chemically ordered fct structure,[28-29] are strongly ferromagnetic (**Figure 6-6**). Magnetically, a sub-10 nm fct-FePt with coercivitiy reaching 20 kOe (or 2 T) is considered to have good chemical

ordering.[30] The 1 h annealed FePt NPs show a two-phase hysteresis behavior with the coercivity at 14 kOe. The soft behavior comes most likely from the existing Fe phase. These FePt NPs are denoted as "partially-ordered" fct-FePt NPs. As a comparison, the 6 h annealed FePt NPs have a single-phase loop and their coercivity reaches 33 kOe (or 3.3 T). This is a very large magnetic coercivity value for the sub-10 nm NPs,[24-26, 31-32] further confirming that the long time annealing does result in much higher degree of chemical ordering within the FePt structure. These FePt NPs are denoted as "fully-ordered" fct-FePt.
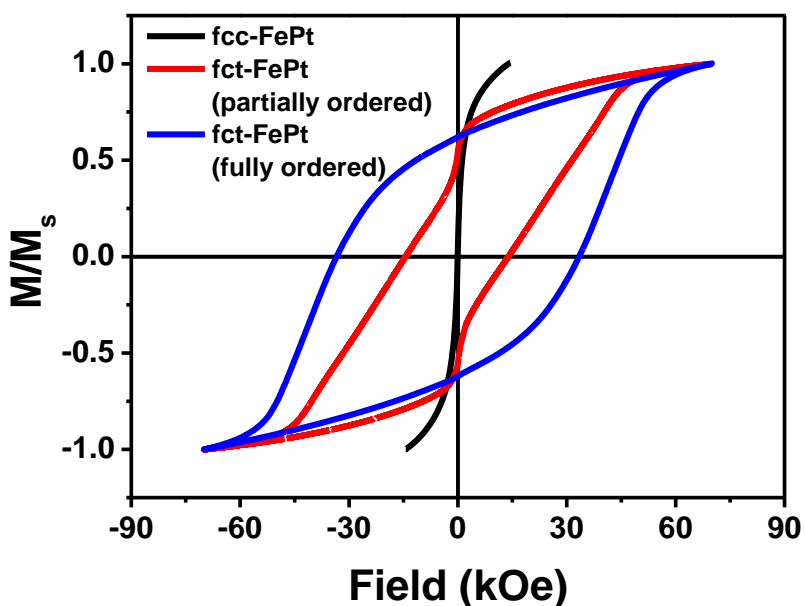
Figure 6-6. Hysteresis loops of the fcc-FePt, fully- and partially-ordered fct-FePt NPs.

The high degree of fct-ordering between Fe and Pt in FePt tends to stabilize Fe in FePt against Fe leaching in an acid solution. For example, when suspended in a 0.5 M nitric acid for 1 h, the fully-ordered fct-FePt NPs showed a very small Fe/Pt composition change from 52/48 to 50/50, but the partially ordered fct-FePt NPs had their Fe/Pt

composition decreased to 41/59. Clearly the Fe layer sandwiched by two Pt layers in the fct-FePt is greatly stabilized by strong d-orbital interactions between Fe and Pt.

As a control for catalytic evaluation, 8 ± 0.5 nm fcc-FePt NPs were also synthesized according to the methods in the experimental section. **Figure 6-5** shows the TEM images of the as-synthesized fcc-FePt NPs and the NPs loaded on Ketjen carbon (denoted as C-fcc-FePt NPs).
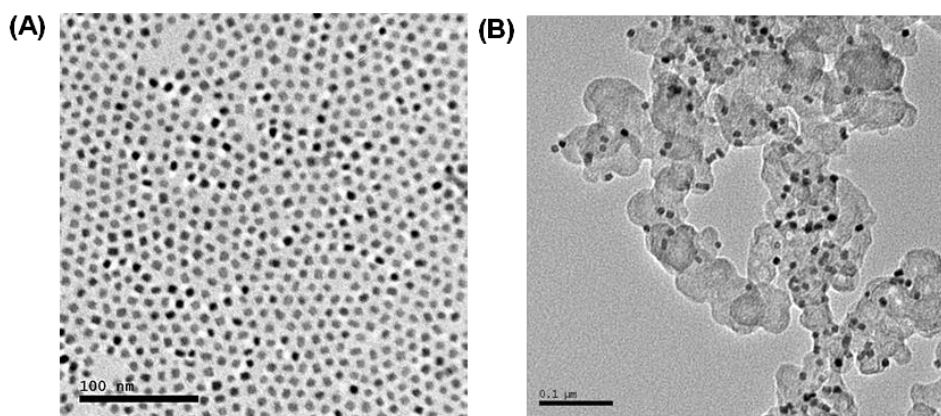
Figure 6-7. TEM images of 8 ± 0.5 nm fcc-FePt NPs and C-fcc-FePt catalyst.

6.3.2. ORR Catalysis of the Fully Ordered fct-FePt Nanoparticles

To evaluate the fct-FePt NP catalysis for ORR, the carbon-supported catalyst was suspended in deionized water + isopropanol + 5% Nafion and deposited on glassy carbon rotating disk electrode (GC-RDE). The commercial Pt and the fcc-FePt NPs were also prepared and studied similarly as the controls. The electrode was subject to 200 cycles of potential scans between 0.05 and 1.3 V (vs. RHE) in the N_2-saturated 0.1 M $HClO_4$ to obtain a stable current-potential curve. The electrochemically active surface area (ECASA) of the catalysts was calculated by integrating the hydrogen underpotential desorption (H_{upd}) peaks of their cyclic voltammograms (CVs) (**Figure 6-8**)
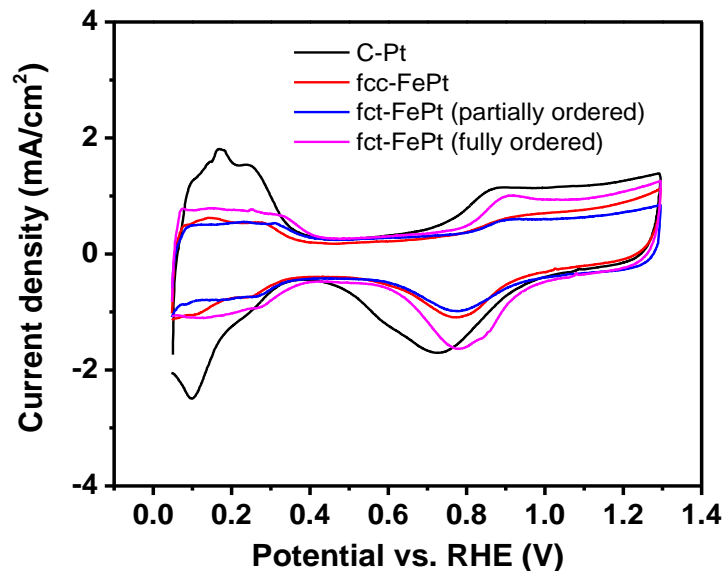
Figure 6-8. CVs of the commercial Pt, *fcc*-FePt, partially ordered *fct*-FePt and fully ordered *fct*-FePt NPs in N_2-saturated 0.1 M $HClO_4$ with a scan rate of 50 mV/s.

ORR measurements were performed in O_2-saturated 0.1 M $HClO_4$ solution at room temperature. **Figure 6-9A** shows the ORR polarization curves for the fully- and partially-ordered fct-FePt NPs, fcc-FePt NPs, and commercial Pt. The polarization curves display the diffusion-limiting current region from ca. 0.3 to 0.8 V and the mixed kinetic-diffusion control region between ca. 0.8 and 1.0 V. The activity, as measured by the ORR onset and half-wave potentials ($E_{1/2}$) in the RDE polarization plots, increases in the following order: commercial Pt < fcc-FePt < partially-ordered fct-FePt < fully-ordered fct-FePt. The $E_{1/2}$ of the ORR on the commercial Pt is 0.883 V. Upon the Pt alloying with Fe to form fcc-FePt NPs, the $E_{1/2}$ value is positively shifted to 0.890 V, which is consistent with the Fe enhancement effect on Pt.[1] After fcc-fct transition, $E_{1/2}$'s of the partially-ordered fct-FePt and the fully-ordered fct-FePt NPs are further improved to 0.927 V and 0.958 V, respectively. This 0.958 V is the most positive value obtained on ORR catalysis by the fct-MPt NPs tested in the similar conditions,[13, 20-21] demonstrating the dramatic

144

catalytic enhancement effect of the fully ordered fct-structure on ORR. **Figure 6-9B** is the Tafel plots of the catalysts studied. All catalysts exhibit slopes of ca. -120 mV/dec at high overpotentials and ca. -60 mV/dec at low overpotentials, suggesting that the ORR rate-determining steps involve the migration of reaction intermediates and charge transfer, respectively.[33] The kinetic current density (j_k) was calculated from the ORR polarization curve according to the Koutecky-Levich equation (Experimental Section) and was further used to obtain mass activity (Pt utilization) and specific activity (intrinsic activity of Pt), as shown in **Figure 6-9C** and **6-9D**. The specific and mass activities of the fully-ordered fct-FePt NPs reach 3.16 mA/cm^2 and 0.69 A/mg$_{Pt}$ respectively at 0.9 V, which are larger than those from the commercial Pt we tested in this work (0.28 mA/cm^2 and 0.13 A/mg$_{Pt}$) and from other fct-MPt NPs reported previously.[13, 20-21]
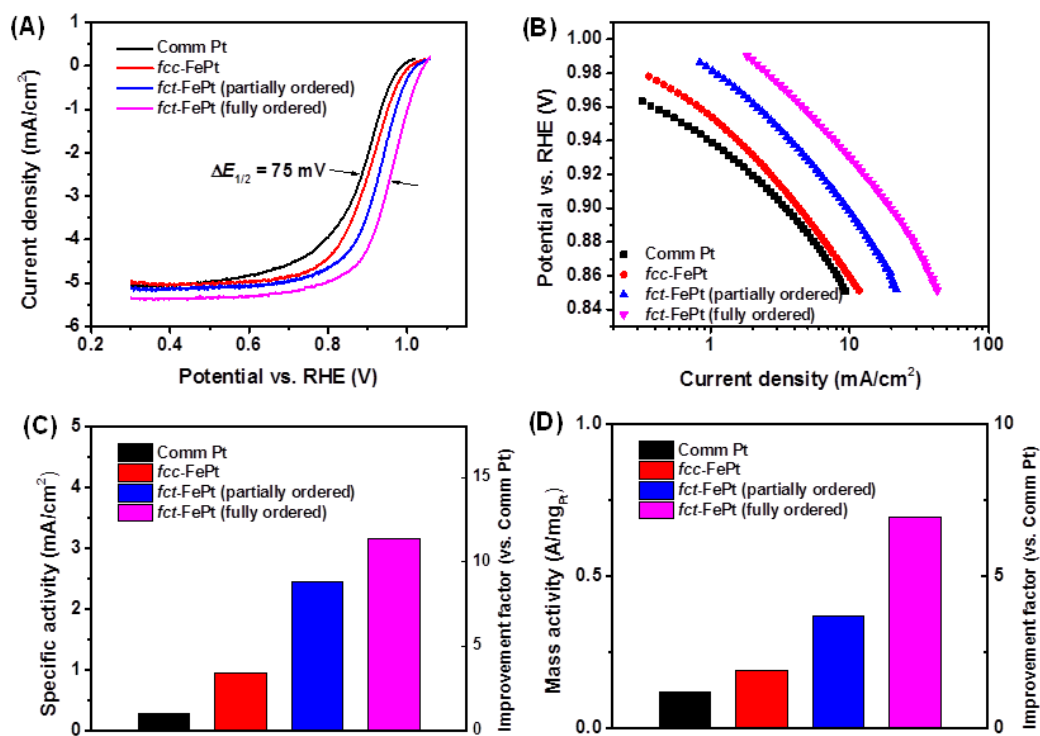
Figure 6-9. (A) ORR polarization curves of C-Pt, C-fcc-FePt, partially- and fully-ordered C-fct-FePt NPs in 0.1 M HClO$_4$ (rotating speed: 1600 rpm, scan rate: 10 mV/s). (B) Tafel plots for the

ORR on different catalysts. (C) The specific activities of different catalysts at 0.9 V. (D) The mass activities of different catalysts at 0.9 V.

The H_2O_2 content in ORR catalyzed by the fully-ordered fct-FePt was measured (by rotating ring/disk electrode) to be ~1% (**Figure 6-10**), further attesting the high selectivity of these FePt NPs on catalyzing ORR *via* a four-electron process.
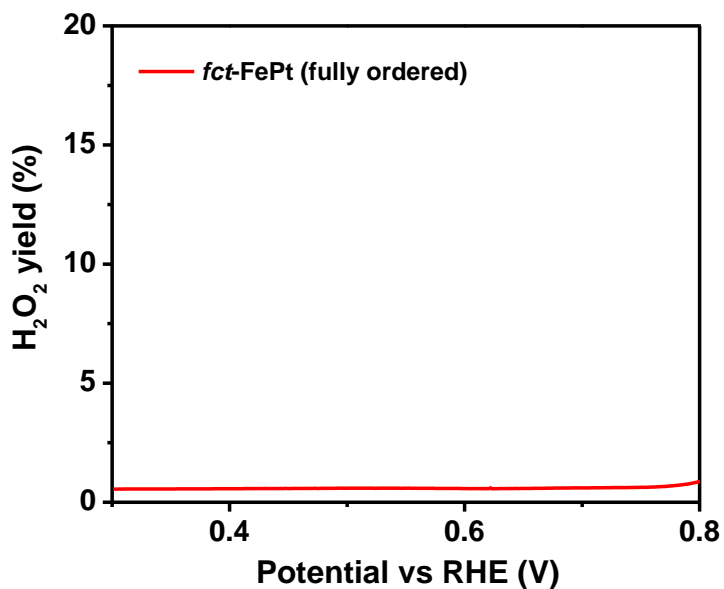
Figure 6-10. H_2O_2 yield of fully-ordered fct-FePt NPs during ORR in 0.1 M $HClO_4$.

The fully-ordered fct-FePt NPs also showed remarkable durability in the ORR test condition. Accelerated durability tests (ADT) of the catalysts were conducted by cycling the potential between 0.6 and 1.0 V in an O_2-saturated 0.1 M $HClO_4$ at room temperature, which is close to the typical potential range at fuel cell cathodes. For the Pt and fcc-FePt catalysts, 5000 cycles caused $E_{1/2}$ a negative shift of ~60 mV (**Figure 6-11A**) and ~80 mV (**Figure 6-11B**), respectively. The stability of the partially-ordered fct-FePt was much improved, showing only slight performance loss after 10000 cycles (**Figure 6-11C**).

The fully-ordered fct-FePt NPs were the most durable catalyst, showing no obvious performance loss (**Figure 6-11D**). TEM image of the fully ordered fct-FePt NPs after stability test indicates no obvious NP morphology changes (**Figure 6-12**). ICP analysis of the NP catalysts after the stability test showed very small Fe/Pt composition decrease from 50/50 to 47/53 after 20000 potential cycles. As a comparison, for the partially-ordered fct-FePt NPs reported previously, their Fe/Pt composition decreases from 50/50 to 26/74 after only 300 potential cycles.[27]
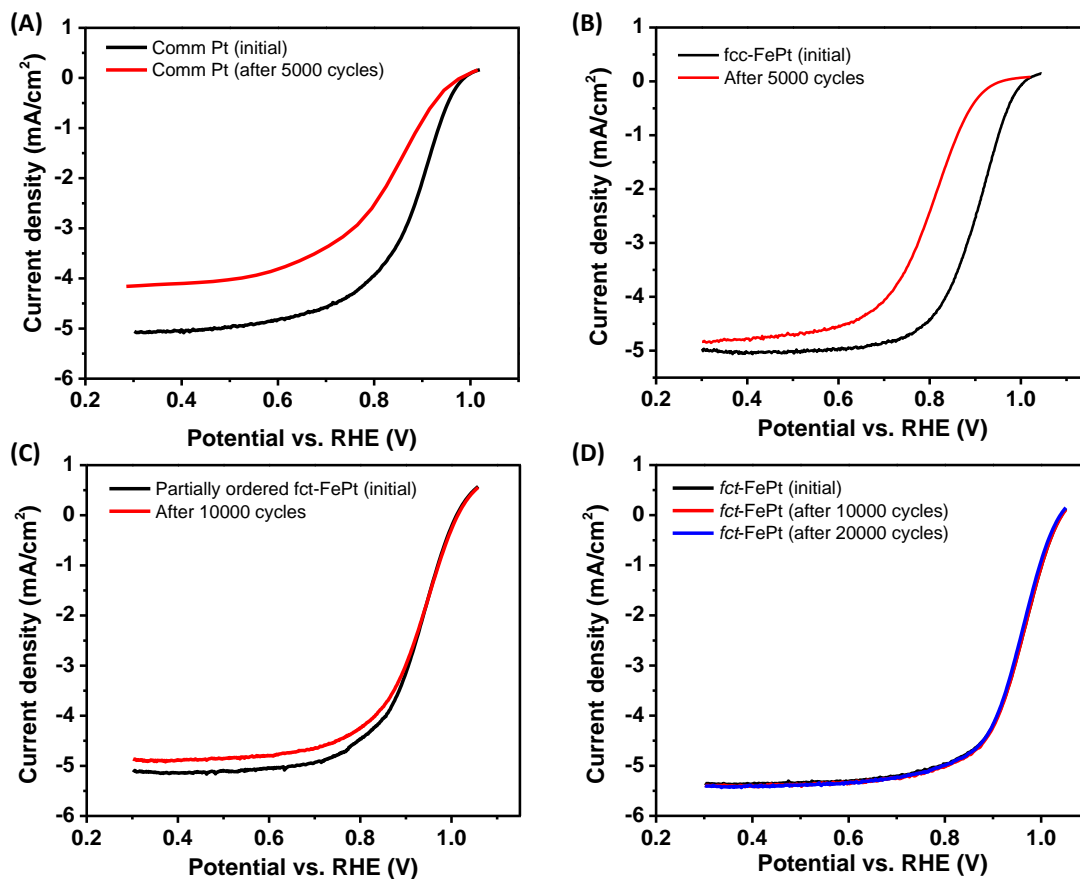
Figure 6-11. ORR polarization curves of (A) commercial Pt catalyst, (B) fcc-FePt NPs, (C) partially ordered fct-FePt NPs and (D) fully ordered fct-FePt NPs before and after stability test. The potential scans were performed between 0.6 and 1.0 V.
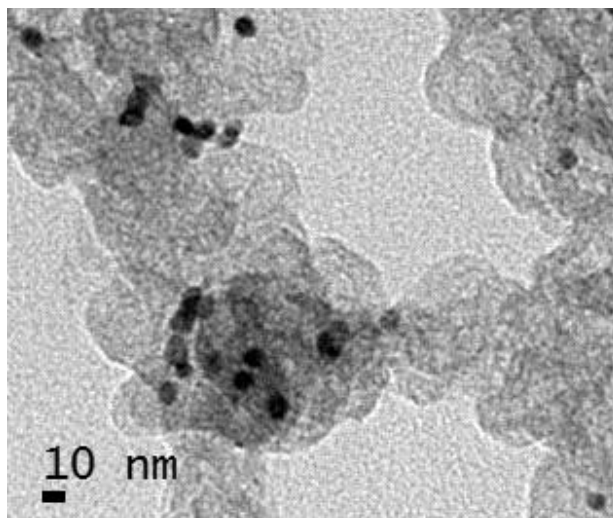
Figure 6-12. TEM image of the fully ordered fct-FePt NPs after the stability test.

The fully-ordered fct-FePt NP catalyst performed equally well in the H_2-air proton exchange membrane fuel cell (PEMFC) cathode under typical operating conditions.[34] The open circuit voltage (OCV) for the commercial Pt (0.959 V) is *ca.* 30 mV lower than that of the fct-FePt catalyst (0.989 V) at the same Pt loading (**Figure 6-13**). The fct-FePt shows ~48% improved performance in the kinetically limited region than the Pt catalyst (0.378 A/cm^2 vs. 0.256 A/cm^2 at 0.8 V). The maximum power density measured from the fct-FePt-based cells was 0.70 W/cm^2, higher than that from the Pt-based one (0.63 W/cm^2). These preliminary data indicate that the fully ordered fct-FePt is a new class of Pt-based catalyst with much desired activity and durability for practical applications in PEMFC.
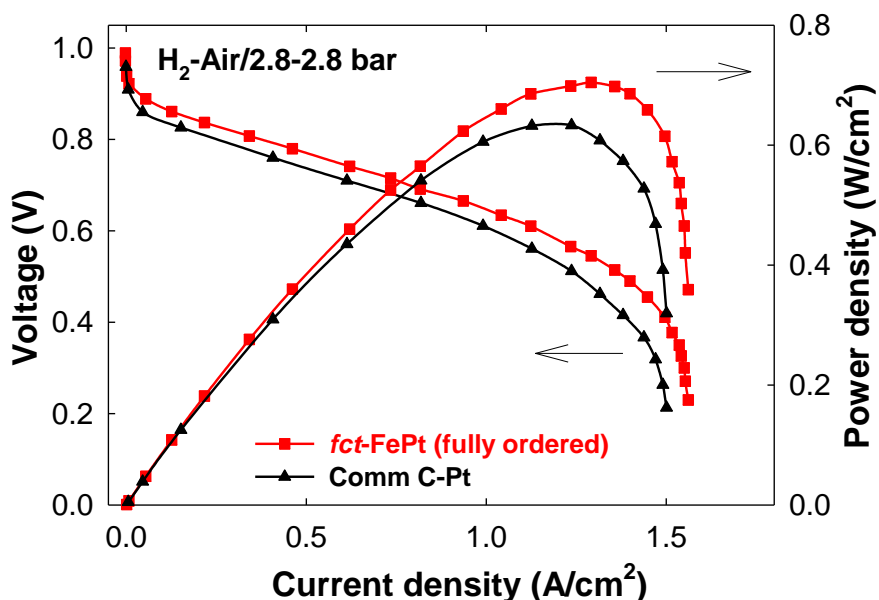
Figure 6-13. H$_2$-air fuel cell polarization plots recorded with various cathode catalysts. Anode: 0.2 mg$_{Pt}$/cm^2 20% C-Pt, 200 scccm H$_2$, backpressure 2.8 bar; cathode: 0.2 mg$_{Pt}$/cm^2 20% C-Pt or fully-ordered C-fct-FePt NPs, 500 sccm air, backpressure 2.8 bar; membrane: 2×Nafion® 212; cell temperature: 80 ℃.

6.3.3. Structure Analysis of the Fully Ordered fct-FePt Nanoparticles

To get more insights of the intermetallic fct-FePt NPs and further confirm the stability enhancement caused by the unique ordered structure, we characterized the fully-ordered fct-FePt NPs after 20000 potential cycles by aberration-corrected high-angle annular dark field scanning transmission electron microscopy (HAADF-STEM) and STEM-electron energy loss spectroscopy (STEM-EELS). **Figure 6-14A** clearly shows the Fe/Pt ordering in the fct-FePt NP by the high (Pt) and low (Fe) Z contrasts. The alternating intensity profile shown in the HAADF-STEM image (**Figure 6-14B**) further confirms the Fe/Pt ordering within the fct-FePt NP.
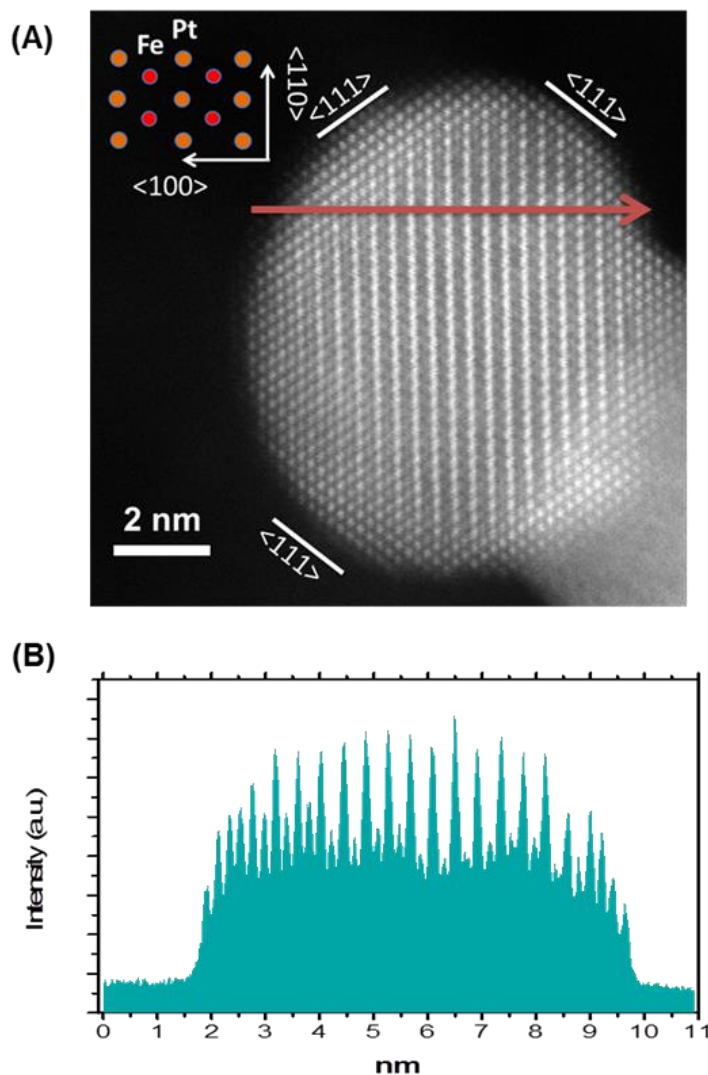
Figure 6-14. (A) HAADF-STEM image of a representative fully-ordered fct-FePt NP after 20000 potential cycles. The arrow indicates the line scan position. An atomic model of the ordered structure is show at the inset. (B) Corresponding HAADF line profile across the line scan position shown in (A).

At the NP surface, a thin Pt layer of ~0.6 nm (ca. 2-4 atomic layers) is shown in the STEM-EELS line scans and 2D elemental mapping image (**Figure 6-15**), but overall, the NP is dominated by the layered Fe/Pt structure, proving that the fully ordered fct-FePt NPs are stable in the ORR condition.
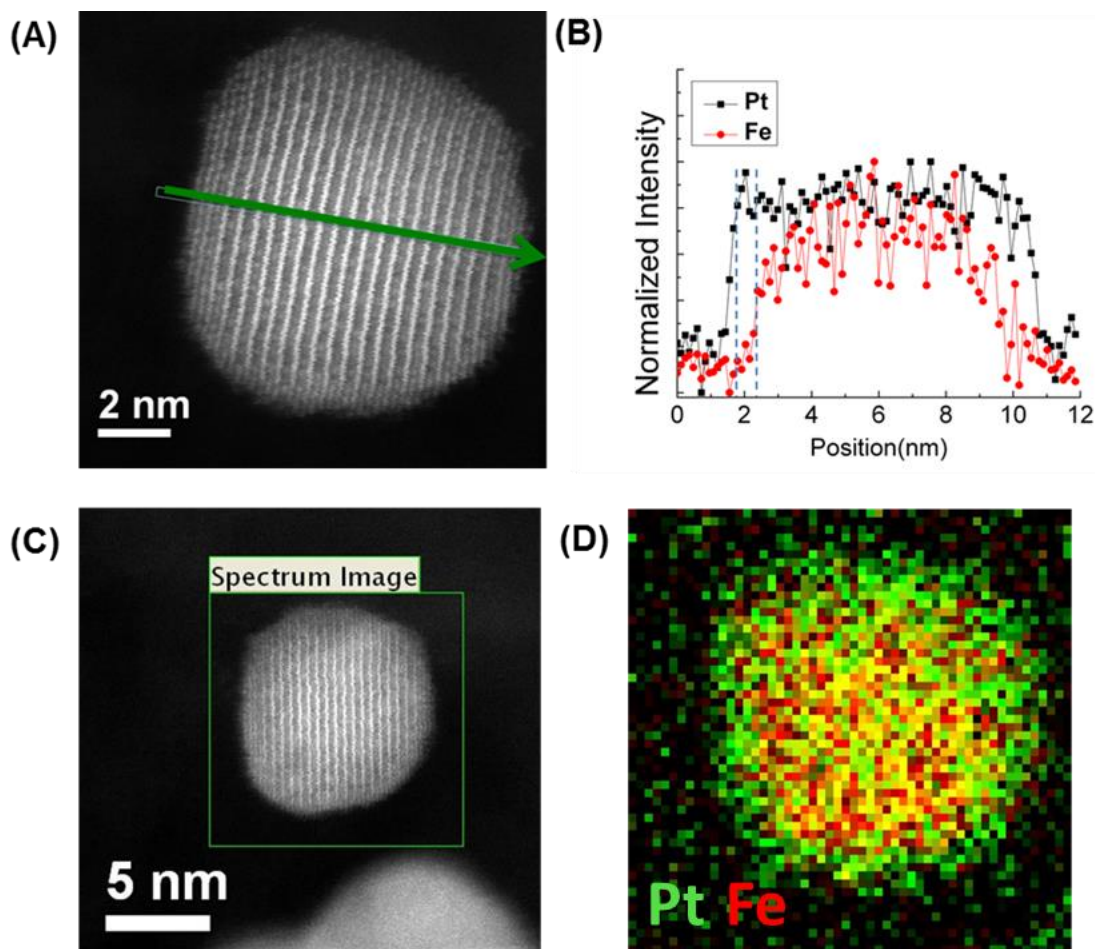
Figure 6-15. (A) and (C) HAADF-STEM image of a representative fully-ordered fct-FePt NP after 20000 potential cycles. (B) STEM-EELS line scan crossing the fct-FePt NP shown in (A). (D) 2D EELS elemental mapping of the fct-FePt NP shown in (C).

6.3.4. HER Catalysis of the Fully Ordered fct-FePt Nanoparticles

The excellent ORR performance of the fully-ordered fct-FePt NPs motivated us to study their catalysis for other electrochemical reduction reactions. Here we chose to study HER, an important half-reaction in the electrochemical water splitting for hydrogen generation.[35] Although Pt has been the state-of-the-art catalyst used to catalyze HER,[3] it is still subject to acid etching and activity degradation. **Figure 6-16** lists HER performance of the commercial Pt, fcc-FePt and fully-ordered fct-FePt in 0.5 M H_2SO_4,

151

showing the activity increase in the order of Pt < fcc-FePt < fct-FePt. The fct-FePt NPs even exhibit higher activity than other Pt-based catalysts reported.[3, 36] The catalyst durability was assessed by applying 10000 potential sweeps between -0.3 and 0.9 V (**Figure 6-16B**). For the Pt catalyst, the potential cycling causes the obvious potential shift (~7 mV at 10 mA/cm^2). For the fct-FePt NPs, two polarization curves obtained before and after the cycling test nearly overlap. The tests prove that the fully ordered fct-FePt NPs are a class of new catalyst with efficiency much superior to any other Pt-based catalysts ever developed for HER.
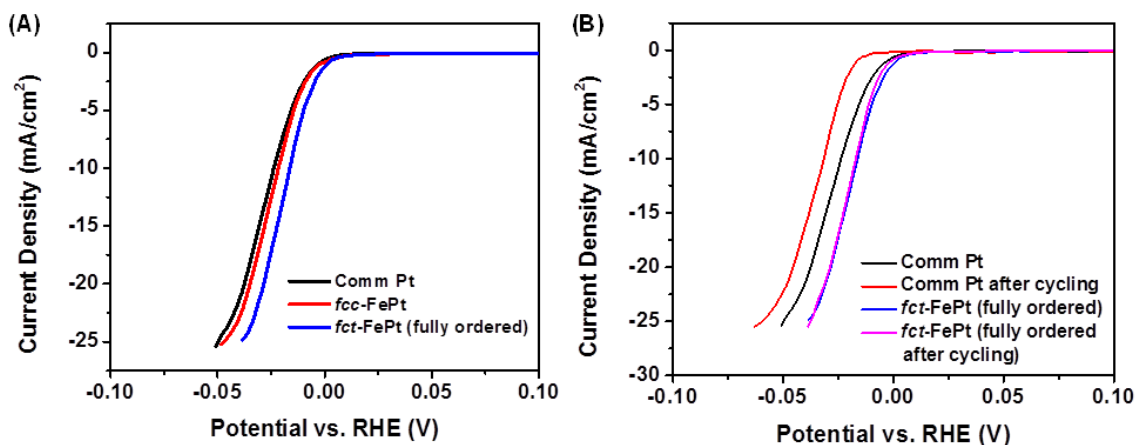
Figure 6-16. (A) HER polarization curves obtained with different catalysts as indicated. (B) HER activity of the commercial C-Pt and fully ordered C-fct-FePt before and after 10000 potential cycling.

6.4. Conclusion

In summary, in this chapter we report a new approach to monodisperse fully-ordered fct-FePt NPs via controlled annealing of MgO-coated dumbbell fcc-FePt-Fe$_3$O$_4$ NPs. In the synthesis, MgO functions as a protecting layer to prevent NPs from sintering in the high temperature annealing condition, Fe$_3$O$_4$ helps to create defects upon Fe$_3$O$_4$ reduction

to Fe, and the dumbbell structure ensures the easy Fe/Pt diffusion to form fully ordered fct-structure. The fully-ordered fct-FePt NPs are characterized by their much enhanced ferromagnetism (room temperature coercivity reaching 33 kOe) and robust chemical stability against Fe etching in the strong acid solution. Compared with other fct-structured alloy NPs in the similar test conditions, the fully-ordered fct-FePt NPs show the highest activity and longest durability in catalyzing ORR in 0.1 M $HClO_4$ and HER in 0.5 M H_2SO_4 without obvious Fe loss and NP degradation. The synthetic strategy demonstrated here is not limited to FePt, but can be extended to other Pt alloy NPs, such as CoPt NPs, and non-Pt alloy NPs, such as FePd and CuAu NPs, providing a versatile approach to fct-alloy NPs with much enhanced catalytic stability and activity for important energy conversion applications.

REFERENCES

[1]   V. R. Stamenkovic, B. S. Mun, M. Arenz, K. J. J. Mayrhofer, C. A. Lucas, G. F. Wang, P. N. Ross, N. M. Markovic, *Nat. Mater.* **2007**, *6*, 241-247.

[2]   S. J. Guo, S. Zhang, S. H. Sun, *Angew. Chem. Int. Ed.* **2013**, *52*, 8526-8544.

[3]   C. Chen, Y. J. Kang, Z. Y. Huo, Z. W. Zhu, W. Y. Huang, H. L. L. Xin, J. D. Snyder, D. G. Li, J. A. Herron, M. Mavrikakis, M. F. Chi, K. L. More, Y. D. Li, N. M. Markovic, G. A. Somorjai, P. D. Yang, V. R. Stamenkovic, *Science* **2014**, *343*, 1339-1343.

[4]   B. Lim, M. J. Jiang, P. H. C. Camargo, E. C. Cho, J. Tao, X. M. Lu, Y. M. Zhu, Y. N. Xia, *Science* **2009**, *324*, 1302-1305.

[5]   S. J. Guo, D. G. Li, H. Y. Zhu, S. Zhang, N. M. Markovic, V. R. Stamenkovic, S. H. Sun, *Angew. Chem. Int. Ed.* **2013**, *52*, 3465-3468.

[6]   J. B. Wu, L. Qi, H. J. You, A. Gross, J. Li, H. Yang, *J. Am. Chem. Soc.* **2012**, *134*, 11880-11883.

[7]   S. I. Choi, S. F. Xie, M. H. Shao, J. H. Odell, N. Lu, H. C. Peng, L. Protsailo, S. Guerrero, J. H. Park, X. H. Xia, J. G. Wang, M. J. Kim, Y. N. Xia, *Nano Lett.* **2013**, *13*, 3420-3425.

[8]   C. H. Cui, L. Gan, M. Heggen, S. Rudi, P. Strasser, *Nat Mater* **2013**, *12*, 765-771.

[9]   J. Zhang, F. H. B. Lima, M. H. Shao, K. Sasaki, J. X. Wang, J. Hanson, R. R. Adzic, *J. Phys. Chem. B* **2005**, *109*, 22701-22704.

[10]   J. X. Wang, H. Inada, L. J. Wu, Y. M. Zhu, Y. M. Choi, P. Liu, W. P. Zhou, R. R. Adzic, *J. Am. Chem. Soc.* **2009**, *131*, 17298-17302.

[11]   C. Wang, D. van der Vliet, K. L. More, N. J. Zaluzec, S. Peng, S. H. Sun, H. Daimon, G. F. Wang, J. Greeley, J. Pearson, A. P. Paulikas, G. Karapetrov, D. Strmcnik, N. M. Markovic, V. R. Stamenkovic, *Nano Lett.* **2011**, *11*, 919-926.

[12]   K. Sasaki, H. Naohara, Y. M. Choi, Y. Cai, W. F. Chen, P. Liu, R. R. Adzic, *Nat. Commun.* **2012**, *3*, 1115

[13]   G. W. Wang, B. Huang, L. Xiao, Z. D. Ren, H. Chen, D. L. Wang, H. D. Abruna, J. T. Lu, L. Zhuang, *J. Am. Chem. Soc.* **2014**, *136*, 9643-9649.

[14]   S. Zhang, Y. Z. Hao, D. Su, V. V. T. Doan-Nguyen, Y. T. Wu, J. Li, S. H. Sun, C. B. Murray, *J. Am. Chem. Soc.* **2014**, *136*, 15921-15924.

[15]   Y. J. Kang, J. Snyder, M. F. Chi, D. G. Li, K. L. More, N. M. Markovic, V. R. Stamenkovic, *Nano Lett.* **2014**, *14*, 6361-6367.

[16]   J. Snyder, T. Fujita, M. W. Chen, J. Erlebacher, *Nat. Mater.* **2010**, *9*, 904-907.

[17]   S. H. Sun, C. B. Murray, D. Weller, L. Folks, A. Moser, *Science* **2000**, *287*, 1989-1992.

[18]   J. Kim, Y. Lee, S. H. Sun, *J. Am. Chem. Soc.* **2010**, *132*, 4996-4997.

[19]   S. Prabhudev, M. Bugnet, C. Bock, G. A. Botton, *ACS Nano* **2013**, *7*, 6103-6110.

[20]   D. L. Wang, H. L. L. Xin, R. Hovden, H. S. Wang, Y. C. Yu, D. A. Muller, F. J. DiSalvo, H. D. Abruna, *Nat. Mater.* **2013**, *12*, 81-87.

[21]   D. L. Wang, Y. C. Yu, H. L. L. Xin, R. Hovden, P. Ercius, J. A. Mundy, H. Chen, J. H. Richard, D. A. Muller, F. J. DiSalvo, H. D. Abruna, *Nano Lett.* **2012**, *12*, 5230-5238.

[22]   K. E. Elkins, T. S. Vedantam, J. P. Liu, H. Zeng, S. H. Sun, Y. Ding, Z. L. Wang, *Nano Lett.* **2003**, *3*, 1647-1649.

[23]   Z. R. Dai, S. H. Sun, Z. L. Wang, *Nano Lett.* **2001**, *1*, 443-447.

[24]   J. M. Kim, C. B. Rong, J. P. Liu, S. H. Sun, *Adv. Mater.* **2009**, *21*, 906-909.

[25]   S. Yamamoto, Y. Morimoto, T. Ono, M. Takano, *Appl. Phys. Lett.* **2005**, *87*, 032503.

[26]   Y. Tamada, S. Yamamoto, M. Takano, S. Nasu, T. Ono, *Appl. Phys. Lett.* **2007**, *90*, 162509.

[27]   S. Zhang, X. Zhang, G. M. Jiang, H. Y. Zhu, S. J. Guo, D. Su, G. Lu, S. H. Sun, *J. Am. Chem. Soc.* **2014**, *136*, 7734-7739.

[28]   G. Brown, B. Kraczek, A. Janotti, T. C. Schulthess, G. M. Stocks, D. D. Johnson, *Phys. Rev. B* **2003**, *68*, 052405.

[29]   T. Burkert, O. Eriksson, S. I. Simak, A. V. Ruban, B. Sanyal, L. Nordstrom, J. M. Wills, *Phys Rev B* **2005**, *71*, 134411.

[30]   C. B. Rong, D. R. Li, V. Nandwana, N. Poudyal, Y. Ding, Z. L. Wang, H. Zeng, J. P. Liu, *Adv. Mater.* **2006**, *18*, 2984-2988.

[31]   J. Kim, C. B. Rong, Y. Lee, J. P. Liu, S. H. Sun, *Chem. Mater.* **2008**, *20*, 7242-7245.

[32]   F. Liu, J. H. Zhu, W. L. Yang, Y. H. Dong, Y. L. Hou, C. Z. Zhang, H. Yin, S. H. Sun, *Angew. Chem. Int. Ed.* **2014**, *53*, 2176-2180.

[33]   C. Coutanceau, M. J. Croissant, T. Napporn, C. Lamy, *Electrochim. Acta* **2000**, *46*, 579-588.

[34]   G. Wu, K. L. More, C. M. Johnston, P. Zelenay, *Science* **2011**, *332*, 443-447.

[35]   H. I. Karunadasa, E. Montalvo, Y. J. Sun, M. Majda, J. R. Long, C. J. Chang, *Science* **2012**, *335*, 698-702.

[36]   J. Greeley, T. F. Jaramillo, J. Bonde, I. B. Chorkendorff, J. K. Norskov, *Nat. Mater.* **2006**, *5*, 909-913.

Chapter 7. Synthesis of FeAu Nanoparticles and Their

Controlled Fe Release

7.1. Introduction

Metal nanoparticles (NPs) have attracted tremendous scientific and technologic attentions due to their great potentials for optical, electronic, catalytic and biomedical applications.[1-4] Significant advancements have been achieved on the synthesis of metal NPs with controlled size, morphology, composition and structure.[5-10] Among the family of metal NPs, Au NPs are of great importance due to their unique optical and catalytic properties.[1] Multicomponent complex Au-based NPs, such as core/shell NPs, dumbbell NPs or alloy NPs,[11-19] have been reported for superior or multi functionality. For example, dumbbell Au-Fe_3O_4 NPs have been synthesized and demonstrated as dual-functional probes for both magnetic and optical imaging of cancer cells.[20] Core/shell Au/$FePt_3$ NPs are more active and durable for oxygen reduction reaction in fuel cells due to the synergistic effect between the core Au NPs and the multimetallic shell.[21] Their properties can be further controlled by alloying Au with other elements. Taking the optical properties into consideration, the plasmonic absorption of AuAg alloy NPs are tunable by changing the composition of Au and Ag.[17, 22] Additionally, AuAg alloy NPs show much enhanced catalytic activity for CO oxidation compared to Au NPs.[17] Alloying with Ni, their catalytic activity for hydrogen evolution reaction is significantly improved compared to pure Au NPs.[23] These results demonstrate various controls of the properties of Au-based NPs.

Metal NPs have great potentials in biomedicine not only for diagnostic but also for therapeutic applications.[24-25] Recently face centered cubic (fcc) FePt NPs were reported to be a new type of agent for cancer therapy.[26] They allow the controlled release of Fe, which reacts with H_2O_2 and generates reactive oxygen species (ROS) in cells, leading to

the fast oxidation of cell membrane and causing cell death. However, there is one issue regarding the potential toxicity of the Pt in the alloy FePt NPs. Unlike Pt, Au NPs are well recognized to be biocompatible and have been extensively studied for their optical properties in bio-imaging.[27-29] Inspired by these, it is desirable to use FeAu alloy NPs as therapeutic agent for cancer therapy. Compared with the fcc-FePt NPs, FeAu alloy NPs have several advantages: 1) the biocompatibility of the FeAu NPs; 2) the optical properties from the plasmonic Au which make them suitable for optical diagnostics; 3) the controlled Fe release from FeAu NPs which acts as the therapeutic agent for therapeutic application. However, so far as we know, FeAu NPs were mainly synthesized through inert gas condensation in a vacuum system,[30-31] which are not suitable for biomedical applications. Solution phase synthesis of FeAu NPs with small size distribution is still challenging.[32] In this chapter, I will introduce the synthesis of uniform FeAu NPs through the simultaneous decomposition of $Fe(CO)_5$ and reduction of Au(III) acetate in the presence of oleic acid and oleylamine. The composition of FeAu is tunable by changing the amount of $Fe(CO)_5$. Through the ligand exchange with dimercaptosuccinic acid (DMSA), the oleic acid/oleylamine covered hydrophobic FeAu NPs can be transferred in hydrophilic water solution. These FeAu NPs are capable of releasing Fe in low pH (4.8) environment while remaining stable in neutral pH (7.0) environment. Our preliminary experiments on the controlled Fe release from FeAu NPs and their unique optical properties demonstrate their potential therapeutic and diagnostic applications in biomedicine.

7.2. Experimental Section

Chemicals: Gold (III) acetate (99.9 %) was purchased from Alfa Aesar. Iron pentacarbonyl (99.99%), oleic acid (90%), oleylamine (70%), 1,2,3,4-tetrahydronaphthalene (99%), 1,2-tetradecanediol (90%), meso-2,3-Dimercaptosuccinic acid (DMSA, 98%), tert-butylamine-borane complex, and 3,3',5,5'-Tetramethylbenzidine dihydrochloride hydrate (TMB·2HCl·xH$_2$O, 97%) were purchased from Sigma Aldrich. Gold(III) chloride hydrate was purchased from Strem Chemicals. Dimethy sulfoxide (DMSO, 99.9%) and dichloromethane (99.9%) were purchased from Macron Chemicals. All chemicals were used as obtained without further purification.

Characterization: Transmission electron microscopy (TEM) images were obtained from a Philips CM20 operating at 200 kV. High-resolution TEM (HR-TEM) images were recorded using a JEOL 2010 with an accelerating voltage of 200 kV. TEM and HR-TEM samples were prepared by depositing a single drop of diluted NPs dispersion on amorphous carbon-coated copper grids. X-ray diffraction (XRD) patterns of the NPs were collected on a Bruker AXS D8-Advanced diffractometer with Cu Kα radiation (λ = 1.5418 Å). Magnetic properties were studied on a Lakeshore 7404 high-sensitivity vibrating sample magnetometer (VSM) with fields up to 1.5 T at room temperature. The inductively coupled plasma-atomic emission spectroscopy (ICP-AES) analysis was measured on a JY2000 Ultrace ICP atomic emission spectrometer equipped with a JY AS 421 autosampler and 2400g/mm holographic grating. UV-vis absorption of the NPs was measured with a Perkin Elmer Lambda 35 spectrometer in the wavelength range of 400 nm to 1000 nm.

Synthesis of FeAu NPs: In a typical synthesis of 4 nm FeAu NPs, 0.1 mmol of Au(O$_2$CCH$_3$)$_3$ (37.4 mg) and 0.2 mmol of 1,2-tetradecanediol (57 mg) were dissolved in the mixture of 0.06 mL of oleic acid, 0.06 mL of oleylamine and 5 mL of 1,2,3,4-tetrahydronaphthalene at 40 ^{o}C for 0.5 h under a gentle flow of Ar gas. Then the mixture was heated up to 60 ^{o}C under the blanket of Ar gas. 0.02 mL of Fe(CO)$_5$ was added to the flask, after which the mixture was heated to 200 ^{o}C at the temperature increasing rate of 10 ^{o}C/min. The reaction was kept for 1 h and then the heating mantle was removed to let it cool down to room temperature. The product was precipitated by ethanol and collected by centrifugation (8500 rpm, 6 min). The product was redispersed in hexane and separated again by adding ethanol and centrifugation (8500 rpm, 8 min). The final product was dispersed in hexane for further use.

Synthesis of 4 nm Au NPs: In a typical synthesis, 0.2 g of HAuCl$_4$ was disolved in 10 mL of oleylamine and 10 mL of 1,2,3,4-tetrahydronaphthalene (Tetralin) under gentle Ar flow at 10 ^{o}C for 15 min. Then the reducing agent of tert-butylamine-borane complex (90 mg) dissolving in oleylamine (1 mL) and tetraline (1 mL) was injected into the mixture. The color changed into deep purple immediately. The mixture was kept at 10 ^{o}C for 1 h. Then aceton (30 mL) was added to precipitate the NPs, followed by centrifugation (8500 rpm, 8 min). The collected NPs were redispersed in hexane and purified again with ethanol. Then the obtained NPs were dispersed in hexane for further use.

Ligand Exchange of the FeAu NPs: 10 mg of the as-synthesized FeAu NPs was dispersed in 1 mL of CH$_2$Cl$_2$. 20 mg of DMSA was dissolved in the mixture of 0.2 mL of DMSO and 2 mL of CH$_2$Cl$_2$. The DMSA solution was added to the FeAu NP dispersion and the mixture was shaken for 2 h under ambient temperature. Then the NPs were

precipitated by adding 10 mL of hexane, followed by centrifugation (2000 rpm, 2 min). The obtained DMSA-FeAu NPs were re-dispersed in 10 mL of de-ionized (DI) water and purified using a dialysis tube (12,000 MW, Spectrum Laboratories, Inc.) in DI-H_2O bath for 24 h to remove the extra small ligands (oleic acid, oleylamine, DMSA, etc.) The final product, DMSA-FeAu NPs in DI- H_2O, was filtered through a 0.22 μm Millex@GP filter (Millipore Corp.). The NP concentration was determined by ICP-AES analysis. DMSA-Au NPs were obtained following the similar procedure.

Fe Release from FeAu NPs: 4ml of the aqueous solution of the DMSA-FeAu NPs were dispersed in dialysis tubing (12,000 MW, Spectrum Laboratories, Inc.) that was further immersed into a 80 mL PBS (pH = 7.4 or 4.8) bath at 37 ^{o}C. A portion (3 mL) of the PBS solution was sampled, and the concentration of Fe was analyzed with ICP-AES.

7.3. Results and Discussion

7.3.1. Synthesis of FeAu Nanoparticles

The FeAu NPs were synthesized through the thermal decomposition of $Fe(CO)_5$ and the reduction of $Au(O_2CCH_3)_3$. Fe and Au composition in the NPs was analyzed by inductively coupled plasma−atomic emission spectroscopy (ICP−AES). The $Fe(CO)_5$ not only acts as the source of Fe, but the CO generated from the decomposition of $Fe(CO)_5$ also acts as the reducing agent for the reduction of $Au(O_2CCH_3)_3$. Keeping the amount of $Au(O_2CCH_3)_3$ (0.1 mmol, 37.4 mg) unchanged, 0.006 mL of $Fe(CO)_5$ resulted in ~ 10 nm FeAu NPs, as shown in **Figure 7-1A**. ICP-AES analysis showed the molar ratio of Fe/Au to be 20/80. Increasing the amount of $Fe(CO)_5$ to 0.012 mL led to the formation of

smaller sized FeAu NPs (~7 nm, **Figure 7-1B**) , with the composition of $Fe_{38}Au_{62}$. This is because more reducing gas CO was formed, facilitating the reduction of $Au(O_2CCH_3)_3$ and the nucleating and growth process. Reacting 0.02 mL of $Fe(CO)_5$ with $Au(O_2CCH_3)_3$ generated even small FeAu NPs with the size of ~ 4 nm and composition of $Fe_{49}Au_{51}$, as shown in **Figure 7-1C**. HR-TEM image in Figure 7-1D of the 4 nm FeAu NPs indicates that most of the obtained NPs are polycrystalline. The inter-fringe distance was measured to be 2.28 Å, smaller than the (111) lattice spacing of pure Au (2.35 Å). This is consistent with the Fe alloying within Au NPs. XRD pattern of the 4 nm FeAu NPs is shown in **Figure 7-2**. It adopts the typical fcc structure of Au, but with the peaks of (111) slightly shifting to right, further confirming the formation of FeAu alloy NPs.
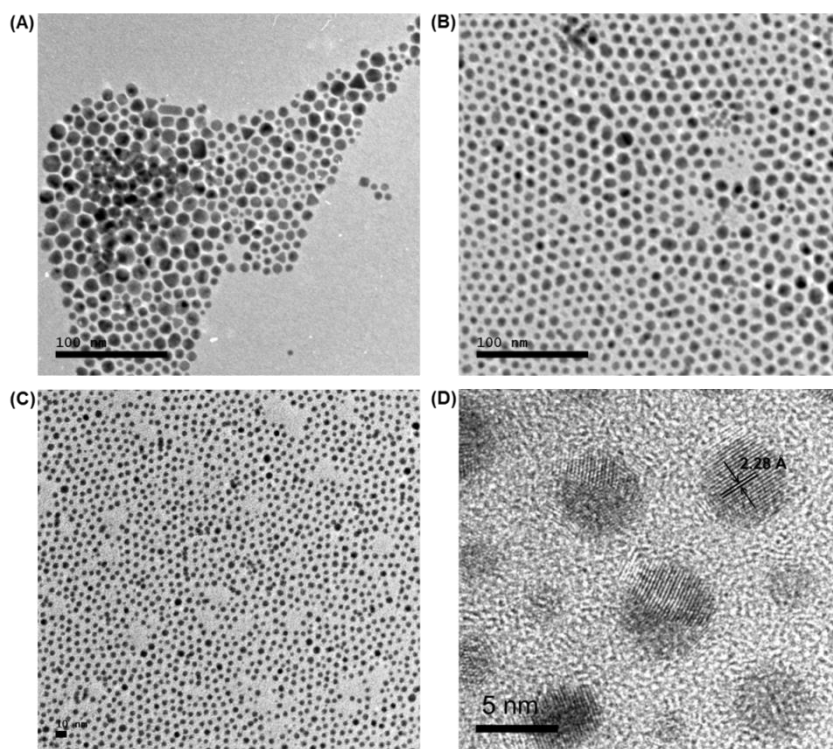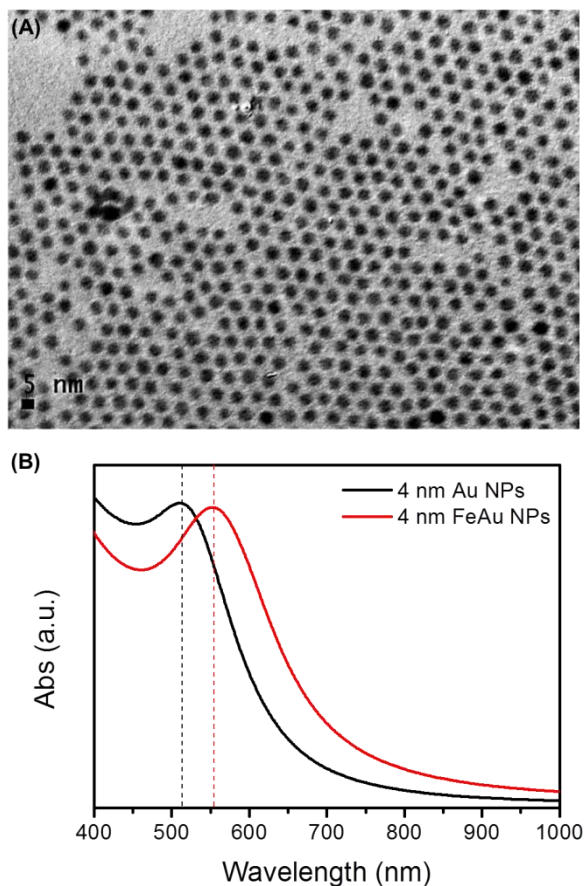

Figure 7-1. TEM images of the as-synthesized (A) $Fe_{20}Au_{80}$ NPs. (B) $Fe_{38}Au_{62}$ NPs. (C) $Fe_{49}Au_{51}$ NPs. (D) HR-TEM image of the $Fe_{49}Au_{51}$ NPs
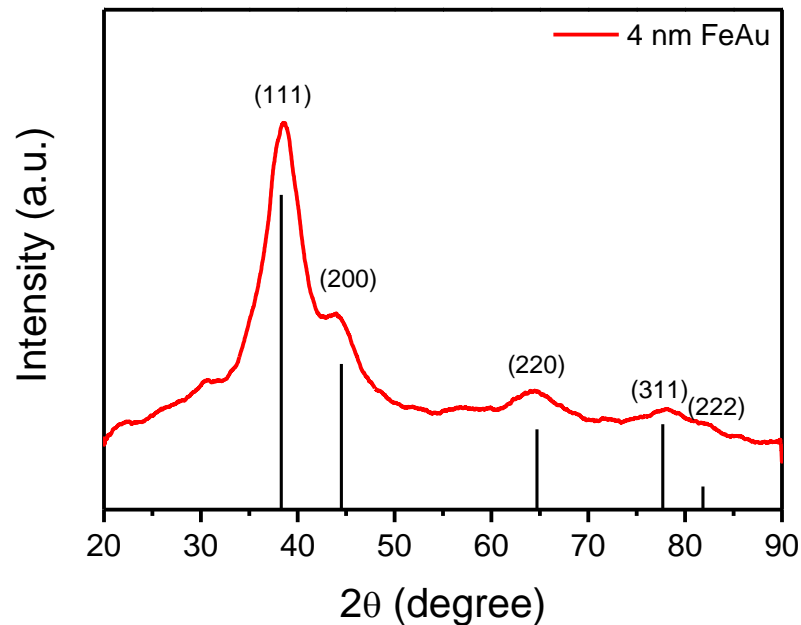
Figure 7-2. XRD pattern of the as-synthesized 4 nm $Fe_{49}Au_{51}$ NPs. Standard peaks of the fcc-Au are listed.

7.3.2. Optical and Magnetic Properties of the FeAu Nanoparticles

To better study the optical properties of the FeAu alloy NPs, 4 nm Au NPs were synthesized as a control. **Figure 7-3A** is the TEM image of the 4 nm Au synthesized according to our previous reported method.[33] UV-vis spectrum of the 4 nm Au NPs in hexane dispersion exhibits characteristic plasmonic absorption at ~515 nm. Different from the pure Au NPs, the surface plasmon absorption of FeAu NPs shows obvious red shift to 555 nm, as shown in **Figure 7-3B**. This is probably due to the surface electron density change caused by the alloying Fe atoms.

Figure 7-3. (A) TEM image of 4 nm Au NPs. (B) UV-vis spectra of the Au and FeAu NPs dispersed in hexane.

Magnetic properties of the FeAu NPs were also studied. **Figure 7-4A** is the room-temperature hysteresis loop of the as-synthesized 4 nm FeAu NPs. They are paramagnetic. Similar to fct-FePt NPs,[8, 34-35] FeAu NPs have been reported to have the ordered $L1_0$ structure with ferromagnetic properties.[30-31] The as-synthesized FeAu NPs are solid solution with Fe and Au randomly occupied in the crystal units. In order to convert the fcc-FeAu into ordered $L1_0$ structure, different annealing was applied. **Figure 7-4B** shows the hysteresis loops of the NPs after annealing at different temperatures in Ar + 5% H_2 gas. After annealing at 400 ^{o}C for 1 h, weak ferromagnetic property with the coercivity (H_c) of 390 Oe was observed in the annealed NPs. The saturation moment (M_s) of the

166

annealed NPs also increased to 21.0 emu/g. Annealing at 500 $^{\circ}$C resulted in increased H_c

of 450 Oe and M_s of 30.8 emu/g. However, further increasing the annealing temperature

caused the decrease of H_c. For example, after annealing at 700 $^{\circ}$C for 1 h, the sample

showed almost superparamagnetic behavior with the H_c of just 50 Oe. This is probably

due to the domain size increase caused by the very high temperature annealing, resulting

in a decrease of the coercivity. The magnetic properties of the annealed FeAu NPs are

summarized in **Table 7-1**.
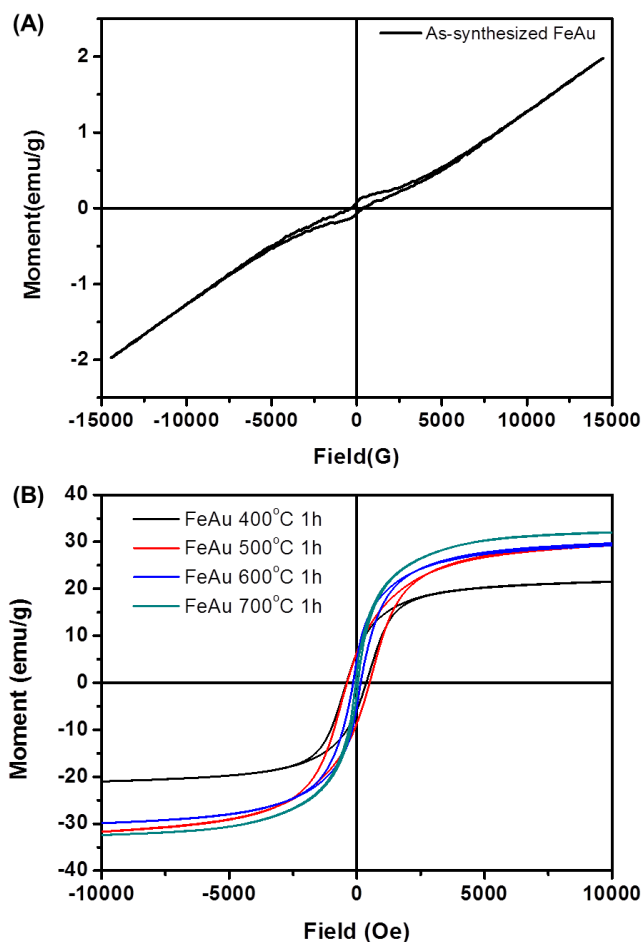
Figure 7-4. (A) Hysteresis loop of the as-synthesized 4 nm FeAu NPs. (B) hysteresis loops of the FeAu NPs after annealing at different temperatures in Ar + 5% H_2 for 1 h.

Table 7-1. Magnetic properties of the annealed FeAu NPs.

Annealing Temperature	400 °C	500 °C	600 °C	700 °C
Saturation Moment (emu/g)	21.0	30.8	29.8	32.2
Coercivity (Oe)	390	450	145	50

The structure of the FeAu NPs after annealing was characterized by the XRD patterns in **Figure 7-5.** Different from the fcc structure of the as-synthesized FeAu NPs, the XRD patterns of FeAu NPs after the annealing display obvious peak right shifts, which can be ascribed to the structure change in the annealed FeAu NPs. As the annealing temperature increased, the width of the diffraction peaks shrunk, indicating the increase of grain size in the annealed NPs. These results are consistent with the observation of the magnetic properties after different annealing treatment.
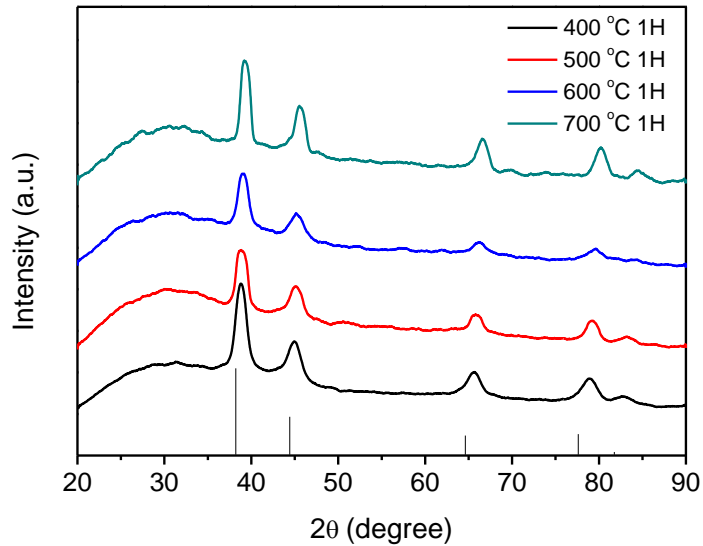
Figure 7-5. XRD patterns of the FeAu NPs after annealing at different temperatures.

7.3.3. Ligand Exchange of Hydrophobic FeAu Nanoparticles

The 4 nm FeAu NPs were chosen for the Fe release experiment. However, the as-synthesized FeAu NPs covered by hydrophobic oleic acid/oleylamine ligands need to be first transferred into hydrophilic media. Ligand exchange was utilized to achieve this goal. Meso-2,3-dimercaptosuccinic acid (DMSA), a biocompatible ligand, was used for the ligand exchange.[36] **Figure 7-6** illustrates the surface modification of the as-synthesized FeAu NPs. The detailed process can be found in the experimental section. After ligand exchange and purification, the MDSA-FeAu NPs were dispersed into DI-H$_2$O. UV-vis spectrum of the DMSA-FeAu NPs in DI-H$_2$O (**Figure 7-7**) shows the absorption at 535 nm, blue shift compared to the FeAu NPs in hexane with the absorption at 555 nm. This is due to the solvent effect on the surface plasmon resonance of the FeAu NPs.[37]
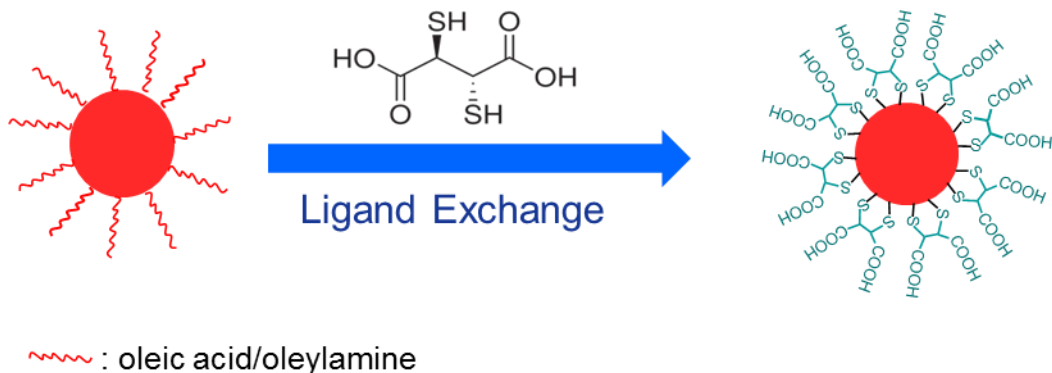
**Figure 7-6**. Ligand exchange of the as-synthesized FeAu NPs with DMSA.
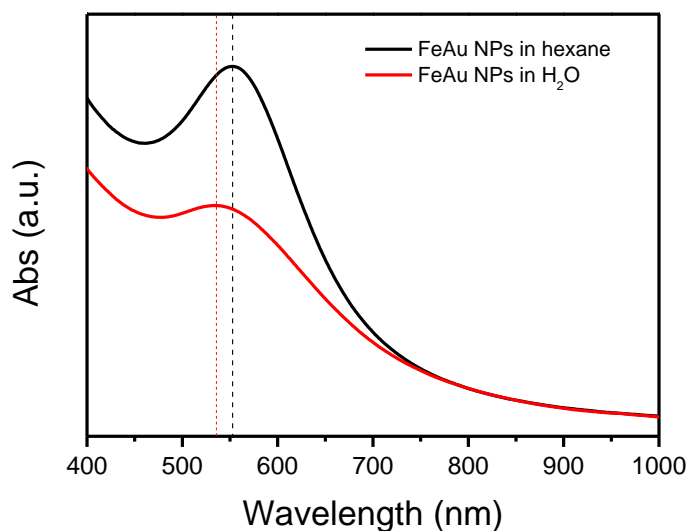
Figure 7-7. UV-vis absorption of the DMSA-FeAu NPs in DI-H_2O.

7.3.4. Fe Release from DMSA-FeAu Nanoparticles

Fe (II) reacting with H_2O_2 is known as Fenton's reaction, which generates reactive oxygen species (ROS) such as •OH. The ROS can oxidize various organic molecules including cell membranes. Compared to normal cells, cancer cells have the overproduction of H_2O_2. The controlled buildup of Fe in tumor cells can increase the production of ROS, causing cellular damage and cell death. Here, we propose using FeAu NPs as therapeutic agents. In order to test the Fe release from the FeAu NPs, the surface of FeAu NPs was modified with DMSA.

The pH-dependent Fe release from DMSA-FeAu NPs was analyzed in phosphate-buffered saline (PBS) with pH 7.4 and pH 4.8. Fe and Au released from the NPs into the PBS buffer solution were measured by analyzing the buffer solution at different time intervals with ICP-AES. The etching results are shown in **Figure 7-8**. At pH = 7.4, the DMSA-FeAu NPs had no measurable Fe release in the buffer solution outside the dialysis

170

tubing within 23 h. However, at pH = 4.8, there was 10% Fe released after 1 h and 22% Fe released after 23 h. Au concentration in the buffer solution was also analyzed. During the experiments, no free Au ion was detected from the DMSA-FeAu NPs, indicating the efficient Fe release under low pH conditions found in the cellular lysosome (pH = 4.8).
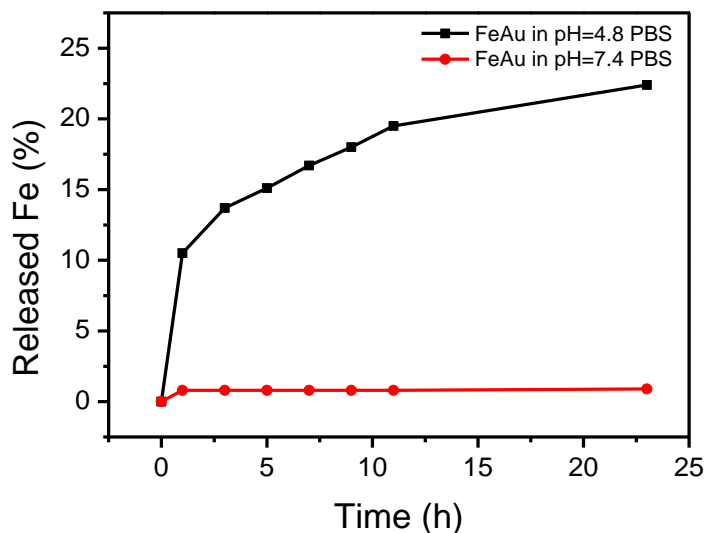
Figure 7-8. Fe release from DMSA-FeAu NPs in PBS solution under different pH conditions.

In order to further confirm the released Fe catalytic activity towards the decomposition of H_2O_2 to ROS, 3,3′,5,5′-tetramethylbenzidine (TMB) was used as the indicator, which can be colorimetrically monitored through the oxidization by the ROS into its one-electron oxidation product.[11] The PBS buffer solution (pH = 4.8) with the 0.1 mM H_2O_2 and 1 mM TMB was made. 4 μg_{Au} of DMSA-FeAu NPs was added to 1.5 mL of the PBS solution. As a control, 4 μg of DMSA-Au NPs was used and added to another 1.5 mL of PBS. The color change of the TMB was monitored. As shown in **Figure 7-9**, the solution in the presence of FeAu NPs showed much deeper color change compared to that with Au NPs even after 15 min, indicating the faster generation of ROS.

The deeper color change can be ascribed to the released Fe from FeAu, which promotes the decomposition of H_2O_2 into ROS. The blue-colored one-electron oxidation product of TMB was further monitored with UV-vis spectrometry. **Figure 7-10** is the UV-vis spectra of the solution after 60 min. Two absorption peaks at 369 and 650 nm were observed for the oxidation product of TMB. The peak intensity of the solution with FeAu NPs was much stronger than the solution with the same amount of Au NPs, further demonstrating the fast ROS formation by FeAu NPs.
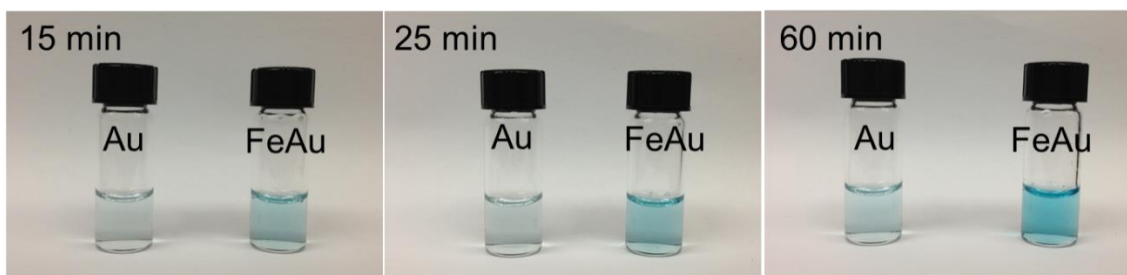
Figure 7-9. Photo image of the PBS solutions (pH = 4.8) with Au and FeAu NPs after different intervals.
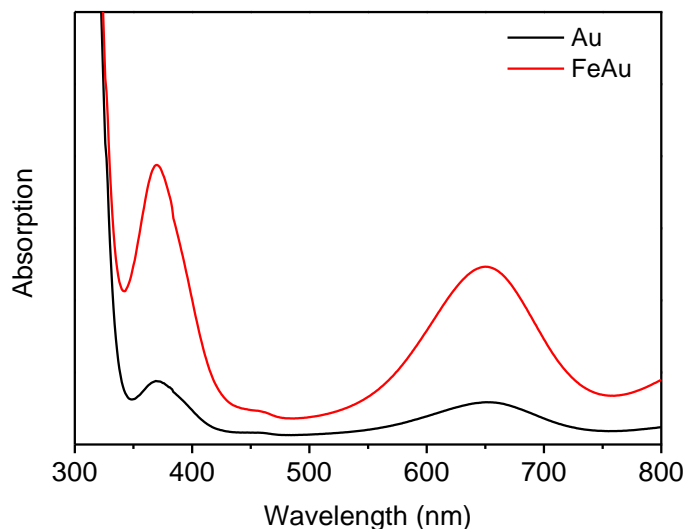
Figure 7-10. UV-vis spectra of the PBS solution with the Au and FeAu NPs after 60 min.

7.4. Conclusion

In summary, we have reported the solution-phase synthesis of uniform FeAu alloy NPs through the simultaneous decomposition of $Fe(CO)_5$ and reduction of $Au(O_2CCH_3)_3$. The composition of Fe and Au in the alloy NPs can be tuned by the amount of $Fe(CO)_5$. The FeAu NPs show strong surface plasmonic absorption at 555 nm. After surface modification, the DMSA-coated FeAu NPs can release Fe under low pH conditions found in the cellular lysosome (pH = 4.8) and the released Fe can catalytically decompose H_2O_2 into reactive oxygen species. With proper surface functionalization, those DMSA-FeAu NPs should serve as an optical probe for cancer detection and therapeutic agent for cancer therapy.

REFERENCES

[1]   M. C. Daniel, D. Astruc, *Chem. Rev.* **2004**, *104*, 293-346.

[2]   E. Boisselier, D. Astruc, *Chem. Soc. Rev.* **2009**, *38*, 1759-1782.

[3]   Y. H. Bing, H. S. Liu, L. Zhang, D. Ghosh, J. J. Zhang, *Chem. Soc. Rev.* **2010**, *39*, 2184-2202.

[4]   J. P. Wilcoxon, B. L. Abrams, *Chem. Soc. Rev.* **2006**, *35*, 1162-1194.

[5]   Z. W. Quan, Y. X. Wang, J. Y. Fang, *Acc.Chem. Res.* **2013**, *46*, 191-202.

[6]   C. Wang, H. Daimon, T. Onodera, T. Koda, S. H. Sun, *Angew. Chem. Int. Ed.* **2008**, *47*, 3588-3591.

[7]   C. Wang, Y. L. Hou, J. M. Kim, S. H. Sun, *Angew. Chem. Int. Ed.* **2007**, *46*, 6333-6335.

[8]   Q. Li, L. Wu, G. Wu, D. Su, H. Lv, S. Zhang, W. Zhu, A. Casimir, H. Zhu, A. Mendoza-Garcia, S. Sun, *Nano Lett.* **2015**.

[9]   L. Wu, P. O. Jubert, D. Berman, W. Imaino, A. Nelson, H. Zhu, S. Zhang, S. Sun, *Nano Lett.* **2014**, *14*, 3395-3399.

[10]   J. M. Kim, C. B. Rong, J. P. Liu, S. H. Sun, *Adv. Mater.* **2009**, *21*, 906-909.

[11]   X. L. Sun, S. J. Guo, C. S. Chung, W. L. Zhu, S. H. Sun, *Adv. Mater.* **2013**, *25*, 132-136.

[12]   C. Wang, C. J. Xu, H. Zeng, S. H. Sun, *Adv. Mater.* **2009**, *21*, 3045-3052.

[13]   V. Mazumder, M. F. Chi, K. L. More, S. H. Sun, *J. Am. Chem. Soc.* **2010**, *132*, 7848-7849.

[14]   X. L. Sun, D. G. Li, Y. Ding, W. L. Zhu, S. J. Guo, Z. L. Wang, S. H. Sun, *J. Am. Chem. Soc.* **2014**, *136*, 5745-5749.

[15]   C. J. Xu, B. D. Wang, S. H. Sun, *J. Am. Chem. Soc.* **2009**, *131*, 4216-4217.

[16]   H. Yu, M. Chen, P. M. Rice, S. X. Wang, R. L. White, S. H. Sun, *Nano Lett.* **2005**, *5*, 379-382.

[17]   C. Wang, S. Peng, R. Chan, S. H. Sun, *Small* **2009**, *5*, 567-570.

[18]   E. V. Shevchenko, M. I. Bodnarchuk, M. V. Kovalenko, D. V. Talapin, R. K. Smith, S. Aloni, W. Heiss, A. P. Alivisatos, *Adv. Mater.* **2008**, *20*, 4323-4329.

[19]   W. Chen, R. Yu, L. L. Li, A. N. Wang, Q. Peng, Y. D. Li, *Angew. Chem. Int. Ed.* **2010**, *49*, 2917-2921.

[20]   Y. M. Lee, M. A. Garcia, N. A. F. Huls, S. H. Sun, *Angew. Chem. Int. Ed.* **2010**, *49*, 1271-1274.

[21]   C. Wang, D. van der Vliet, K. L. More, N. J. Zaluzec, S. Peng, S. H. Sun, H. Daimon, G. F. Wang, J. Greeley, J. Pearson, A. P. Paulikas, G. Karapetrov, D. Strmcnik, N. M. Markovic, V. R. Stamenkovic, *Nano Lett.* **2011**, *11*, 919-926.

[22]   C. Wang, H. G. Yin, R. Chan, S. Peng, S. Dai, S. H. Sun, *Chem. Mater.* **2009**, *21*, 433-435.

[23]   H. Lv, Z. Xi, Z. Chen, S. Guo, Y. Yu, W. Zhu, Q. Li, X. Zhang, M. Pan, G. Lu, S. Mu, S. Sun, *J. Am. Chem. Soc.* **2015**.

[24]   L. M. Lacroix, N. F. Huls, D. Ho, X. L. Sun, K. Cheng, S. H. Sun, *Nano Lett.* **2011**, *11*, 1641-1645.

[25]   P. K. Jain, I. H. El-Sayed, M. A. El-Sayed, *Nano Today* **2007**, *2*, 18-29.

[26]   C. J. Xu, Z. L. Yuan, N. Kohler, J. M. Kim, M. A. Chung, S. H. Sun, *J. Am. Chem. Soc.* **2009**, *131*, 15346-15351.

[27] K. Sokolov, M. Follen, J. Aaron, I. Pavlova, A. Malpica, R. Lotan, R. Richards-Kortum, *Cancer Res.* **2003**, *63*, 1999-2004.

[28] I. H. El-Sayed, X. H. Huang, M. A. El-Sayed, *Nano Lett.* **2005**, *5*, 829-834.

[29] J. Chen, F. Saeki, B. J. Wiley, H. Cang, M. J. Cobb, Z. Y. Li, L. Au, H. Zhang, M. B. Kimmey, X. D. Li, Y. N. Xia, *Nano Lett.* **2005**, *5*, 473-477.

[30] P. Mukherjee, P. Manchanda, P. Kumar, L. Zhou, M. J. Kramer, A. Kashyap, R. Skomski, D. Sellmyer, J. E. Shield, *Acs Nano* **2014**, *8*, 8113-8120.

[31] P. Mukherjee, Y. Zhang, M. J. Kramer, L. H. Lewis, J. E. Shield, *Appl. Phys. Lett.* **2012**, *100*.

[32] I. C. Chiang, D. H. Chen, *Adv. Funct. Mater.* **2007**, *17*, 1311-1316.

[33] S. Peng, Y. M. Lee, C. Wang, H. F. Yin, S. Dai, S. H. Sun, *Nano Res.* **2008**, *1*, 229-234.

[34] S. H. Sun, C. B. Murray, D. Weller, L. Folks, A. Moser, *Science* **2000**, *287*, 1989-1992.

[35] J. Kim, C. Rong, Y. Lee, J. P. Liu, S. Sun, *Chem. Mater.* **2008**, 7242–7245.

[36] T. J. Yoon, H. Lee, H. L. Shao, R. Weissleder, *Angew. Chem. Int. Ed.* **2011**, *50*, 4663-4666.

[37] S. Underwood, P. Mulvaney, *Langmuir* **1994**, *10*, 3427-3430.